SIMULATIONS OF MULTI-PHOTON DISSOCIATION OF CALCIUM MONOHYDRIDE AND CALCIUM MONODEUTERIDE IONS

A Dissertation
Presented to
The Academic Faculty

By

Smitha S. Janardan

In Partial Fulfillment
of the Requirements for the Degree
Doctor of Philosophy in the
School of Chemistry and Biochemistry

Georgia Institute of Technology

December 2017

SIMULATIONS OF MULTI-PHOTON DISSOCIATION OF CALCIUM MONOHYDRIDE AND CALCIUM MONODEUTERIDE IONS

Approved by:

Dr. Kenneth R. Brown, Advisor
School of Chemistry and Biochemistry
Georgia Institute of Technology

Dr. C. David Sherrill
School of Chemistry and Biochemistry
Georgia Institute of Technology

Dr. Joseph Perry
School of Chemistry and Biochemistry
Georgia Institute of Technology

Dr. Thomas Orlando
School of Chemistry and Biochemistry
Georgia Institute of Technology

Dr. Brian Kennedy
School of Physics
Georgia Institute of Technology

Date Approved: October 17, 2017

An expert is someone who knows some of the worst mistakes that can be made in his

subject, and how to avoid them.

Werner Heisenberg

I dedicate this dissertation to my parents, who supported every decision I made; my advisor, who guided me in this process; my labmates, who answered all of my stupid questions; and my friends, who helped me stay sane.

ACKNOWLEDGEMENTS

Labmates:

- Gang Shu

- John Condoluci

- Aaron Calvin

- Renè Rugango

- Mauricio Gutiérrez

- Yu Tomita

- Alonzo Hernandez

- Silas Fradley

- Ryan Sheehan

Collaborators:

- Andrew Cross for useful discussion

- M. Kajita for useful discussion

- E. Hudson for useful discussion

- D. Denison for use of the MIRA

- Y. Choi for assistance with data collection

- Colin Trout for his input on the manuscript

- Minori Abe for providing us with data from Ref. [1, 2]

- Dr. Chris Seck for providing guidance on the pulse shaping setup

TABLE OF CONTENTS

LIST OF FIGURES

SUMMARY

We observe various transitions in CaH^+ and CaD^+ by resonance enhanced multiphoton photodissociation spectroscopy in a Coulomb crystal. We report the the vibronic $1^1\Sigma$ $v_0 \longrightarrow 2^1\Sigma$ $v'_{0,1,2,3,4}$ transitions of CaH^+ and CaD^+; rovibronic $1^1\Sigma$ v_0,J $\longrightarrow 2^1\Sigma$ $v'_{0,1,2,3}$,J' transitions of CaH^+; vibrational $1^1\Sigma$ $v_0 \longrightarrow 1^1\Sigma$ $v'_{9,10}$ transitions of CaH^+. This system is ideal for performing high-precision molecular spectroscopy with applications in astrochemistry and fundamental physics. These measurements are vital to future quantum logic spectroscopy (QLS) experiments and for measuring rotational state preparation of CaH^+.

We used CaH^+ co-trapped with Doppler cooled Ca^+ to perform spectroscopy using photodissociation. The Ca^+ fluorescence served as a detector for dissociation rates. The broad linewidth of the laser provided an advantage for the initial search for transitions, but did not allow spectral resolution of rotational transitions. We use pulse shaping to spectrally narrow the linewidth of the laser to obtain rotational constants for the rovibronic states.

We assign the observed peaks to the transition from the ground vibrational state using a theoretical model based on previous theoretical predictions. The simulation method comes in two flavors: simple and full simulations. The simple model that assumes instantaneous dissociation after resonant excitation, while the full simulations uses a matrix ordinary differential equation to account for all possibilities. Both methods convolute a tunable laser with an underlying rovibronic spectrum to find corresponding transition rates.

Physical constants and information, such as transition frequency, transition dipole moments, rotational constants, and dissociation pathway, come from fitting the simulated spectrum to the experimental spectrum. The vibrational transitions matched theory well when a thinner laser linewidth is assumed. The CaH^+ vibronic peak assignments initially match theoretical predictions well. Comparisons with CaD^+ vibronic peak assignments reveal a revised assignment of the CaH^+ vibronic levels and a disagreement with CASPT2

theoretical calculations by approximately 700 cm^{-1}. Rovibronic peak assignments affirm the predicted rotational and distortion constants. We will describe possible dissociation paths through excited Σ and Π states.

CHAPTER 1

INTRODUCTION/BACKGROUND

There has been a recent push towards creating cold (<1 K) and ultracold (<1 mK) molecular ions. At these cold temperatures, molecules and atoms possess a number of unique properties. Firstly, they are trapped within the Lamb Dicke regime, which means the motional modes are not only suppressed, but also decoupled from the internal transitions [3]. This disconnection is important for maintain precise state control, control of degrees of freedom, and manipulating state distribution [4]. Secondly, the de Broglie wavelength grows larger, which enhances previously masked properties such as tunneling, barrier reflection, scattering, interference, and more [5–8]. Next, the molecules have increased sensitivity to interactions from long-range portions of the potential energy surface [5, 7–9]. Finally, cold molecular ions form Coulomb crystals which are important to maintain experimental conditions and detect the number of ions [4, 10]. These properties make cold molecular ions ideal for a number of applications such as quantum chemistry [3, 7, 11–19], cold chemistry [8, 11, 13, 15, 17, 20, 21], quantum information [3, 10–19, 22–24], tests of fundamental physics [7, 12, 16], astrochemistry [3, 12], collisional mechanisms/dynamics [3, 5–11, 17–19, 21, 22, 25–28], and precise spectroscopy [3, 6, 10, 11, 14, 16, 17, 19].

This dissertation discusses recent efforts to obtain experimental spectroscopy constants of CaH^+, specifically transition frequencies, dissociation frequencies, various electronic energy levels, and ro-vibronic constants. CaH^+ is a molecule of interest due to its extensive applications towards testing time variation of fundamental constants [2, 29–35] and astrochemistry [13, 21, 32, 35–37]. Other applications are thermometry, a technique measuring temperature through the rotational distribution [38], testing quantum theory and benchmarking quantum theoretical calculations [33, 39], molecular clocks
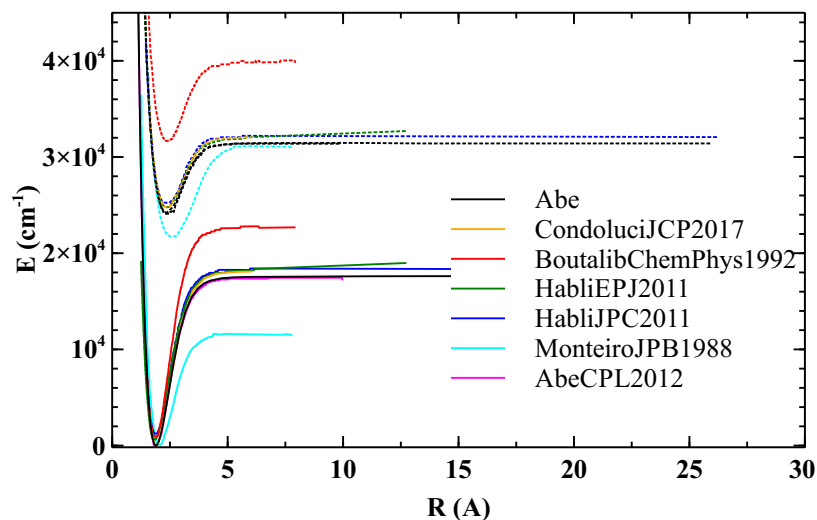
Figure 1.1: A comparison of the $X^1\Sigma$ and $A^1\Sigma$ potential energy surface (PES) curves from various theoretical studies of CaH^+ [**CondoluciJCP2017s**, 2, 36, 42–44].

[13], and understanding transition metal bonding through comparisons with other XH^+ species, where X is a variety of other atoms [27, 40, 41]. Extensive investigations on theoretical CaH^+, over the past 30 years, agree on the potential applications but differ on the quantitative results, **Figure 1.1** [1, 2, 27, 29–31, 36, 37, 40–45]. Furthermore, CaH^+ experimental research is inadequate for these same applications. Hansen et al. used a combination of photodissociation and nondestructive mass spectrometry to observe reaction rates and reaction product branching ratios [46]. Mokhberi et al. demonstrated sympathetic cooling of co-trapped $^+$ and CaH^+ [47]. Chou et al. implemented quantum-logic spectroscopy to prepare and detect CaH^+ rovibronic states in order to observe Rabi flopping and Ramsey fringes [35]. Okada et al. demonstrated trapping, Coulomb crystal formation, and cooling in an ion trap [32, 48, 49]. We use a combination of theoretical and experimental techniques (e.g. resonance-enhanced multi-photon dissociation (REMPD) and matrix ordinary differential equations (ODEs)) to find these spectroscopic properties. This introduction concentrates on motivations and applications for the various experimental techniques, meanwhile the rest of the dissertation focuses on theoretical work pertaining to CaH^+.

The measurement of the time variation in fundamental constants is a recent area of study for atoms and molecules. Many current physics models, e.g. the Grand Unification Theorem (GUT), Einstein Equivalence Principle (EEP), and standard model, assume all fundamental constants are independent of time and space. Confirming any time dependence in constants disproves all of these theorems [29–31, 50–54]. The most common constants measured are the mass ratio of an electron to proton, m_e/m_p, or the fine structure constant, α [13, 29–31, 51, 52, 55, 56]. Given sufficient accuracy, analyzing this ratio or constant repeatedly over a period of years determines the proposed time variation. Both molecules and atoms contain vibrational, rotational, and other transition frequencies proportional to $\sqrt{m_e/m_p}$ and m_e/m_p, respectively [13, 29–31, 45, 50–52, 55, 57, 58]. Ultimately, many considerations make molecules better adapted to time variation studies over atoms. Molecular transitions respond with increased sensitivity to variation, making changes in $\sqrt{m_e/m_p}$ easier to observe [29–31, 34, 51, 54, 55]. With the discovery of sympathetic and Doppler cooling, molecules reach cooler temperatures than atoms [29, 31, 34]. Some molecules have large rotational constants, which decouples them from blackbody radiation, and they stay trapped within the Lamb-Dicke regime for hours (i.e. decoupling from external temperature affects on quantum state distribution))[29–31, 34, 50, 56, 59–62]. Knowing diatomic hydrides generally have large rotational constants, Koelemeij et al. provides empirical evidence of HD^+ molecules offering enhanced results over atoms, but did not provide sufficient sensitivity to yield an answer [39]. A proposed two-ion-species technique, previously seen in precise atomic ion clocks [63, 64], may increase precision for molecules [51]. Kajita et al. proposes experiments implementing this technique with a CaH^+ ion coupled with a Ca^+ ion proffering sufficient accuracy to observe variation [29–31]. Kajita et al. chose CaH^+ over other molecules since the expected uncertainty in frequency measurements are smaller than HD^+, since they are closer to the order of the predicted astronomical time variation [29–31, 34]. In addition, the work from this dissertation prove that CaH^+ and Ca^+ have a known scheme to co-trap

CaH$^+$ and Ca$^+$, a known scheme to cool using sympathetically cooling, and no hyperfine splitting. Due to lack of experimental data with the vibrational transition frequencies, no CaH$^+$ investigations on constant variation exist as of yet.

Interstellar media (ISM), stellar atmospheres, comets, and the sun contain various ionic gases, atomic gases, molecular gases, dust, and cosmic rays at various temperatures. These area contain many diatomic hydride cation species, formed through steller evolution in warmer regions, which makes identifying other species present essential [36, 37, 43, 44]. These components generate stars and their chemistry plays a fundamental role in star formation and determining star lifetimes. Without physical accessibility to these sectors in space, the absorption and emission lines of atoms and molecules are the only means by which to identify constituents. These frequencies are matched to total solar irradiance (TSI) spectrum provided by various satellite experiments. While atoms do not have temperature-depended rotation distributions, molecules require detailed information of spectroscopic constants to map transition frequencies to interstellar temperatures, [36, 37]. High-precision spectroscopy of cold and ultracold molecules provides this information with adequate precision, [65, 66]. CaH, Ca, and Ca$^+$ exist in sun spots [36, 37, 67–69] and surface of stars [70], which indicates CaH$^+$ should exist in space as well. The presence of all four species leads to future investigations involving reaction chemistry in sun spots. In addition, CaH$^+$ has a low ionization potential similar to MgH$^+$, which is also present in space [37, 44]. If CaH$^+$ appears in space, CaH$^+$ act as a thermometer, where measuring the rotational distribution indicates a temperature [38]. The lack of experimental spectroscopic data stalls efforts to identify this species in the solar spectrum.

All further applications of CaH$^+$ require measuring precise spectroscopic constants. Experimental efforts center around co-trapping CaH$^+$ and Ca$^+$, cooling to an absolute rovibronic state, and finally using high-precision spectroscopy to measure transition frequencies. Ions traps both confine and co-trap multiple ionic species in the gas phase. While mass spectrometry (MS) and time of flight (TOF) experiments are viable alternative

methods, they experience low number density of ions and therefore weak absorption and dispersion signals [71, 72]. Ion-traps are preferable due to longer trapping times and more controlled environments [17, 73–75]. External cooling to the motional ground state and internal cooling to state-select a rovibrational state ensures accuracy and reduces the risk of misinterpreting the CaH^+ spectrum. Different cooling techniques such as buffer-gas cooling and electric field manipulation are popular but less effective within ion-traps [13]. CaH^+ is co-trapped Ca^+ to ease formation and detection methods. Due to this, sympathetic cooling suits CaH^+ best [13, 32, 33, 76, 77]. Many high-precision spectroscopy schemes are available within an ion trap, e.g. REMPD [76], fluorescence spectroscopy, and quantum logic spectroscopy (QLS) [63, 78]. Regrettably, many fluorescence spectroscopy experiments are subjected to Doppler shifts and peak broadening within ion traps. This dissertation concentrates on REMPD experiments, which leads to possible QLS experiments in the future.

1.1 Ion Traps

Ion trap research and application advancements benefits high-precision spectroscopy by providing stable experimental conditions. In particular, molecular ions are spatially confined, co-trapped with other species, and well-isolated from stray fields and collisions [53, 73–75, 79]. The longer potential confinement times benefit complex schemes which require lengthy experimentation times, and the high-density of molecules aid precision experiments by giving higher signals-to-noise ratios [13, 73–75]. Modern research implements three main types of traps: Penning traps, Paul traps, and combination magneto-optical traps (MOTs) with RF traps. Larson et al. demonstrated cooling using a Penning trap, however the high density within the trap leads to Doppler shifts of the spectroscopic lines [80]. Penning traps have limited magnetic field ranges available, inhibiting many experiments [9]. MOTs combined with Paul traps, i.e. MOTION traps, have high expectations, but are currently a work in progress [81–86]. Paul traps (i.e. radio

frequency (RF) traps) are the most commonly used trap for ultracold molecular ions. These traps are simplistic and are compatible with a large range of optical lasers [86]. The number of poles within the trap changes depending on the set-up and experimental needs. The later cited applications use 4-pole, 8-pole, or 22-pole typically; this dissertation focuses on quadrupole since they linearize easier [87], **Figure 1.2**. Linear Paul traps may eliminate the motional mode in the z direction, which reduces the required complexity in the cooling scheme [88]. Paul traps have additional applications, outside the ones mentioned above, in polarization experiments [53], state-selection scheme development [89, 90], molecular clocks [91], spectroscopy [28, 63, 73, 74, 79, 92–97], cooling scheme development [4, 10, 16, 20, 76, 77, 98], observing chemical reactions [8, 25, 32], detecting molecules [99–102], and state detection [103–105], and quantum control [88].
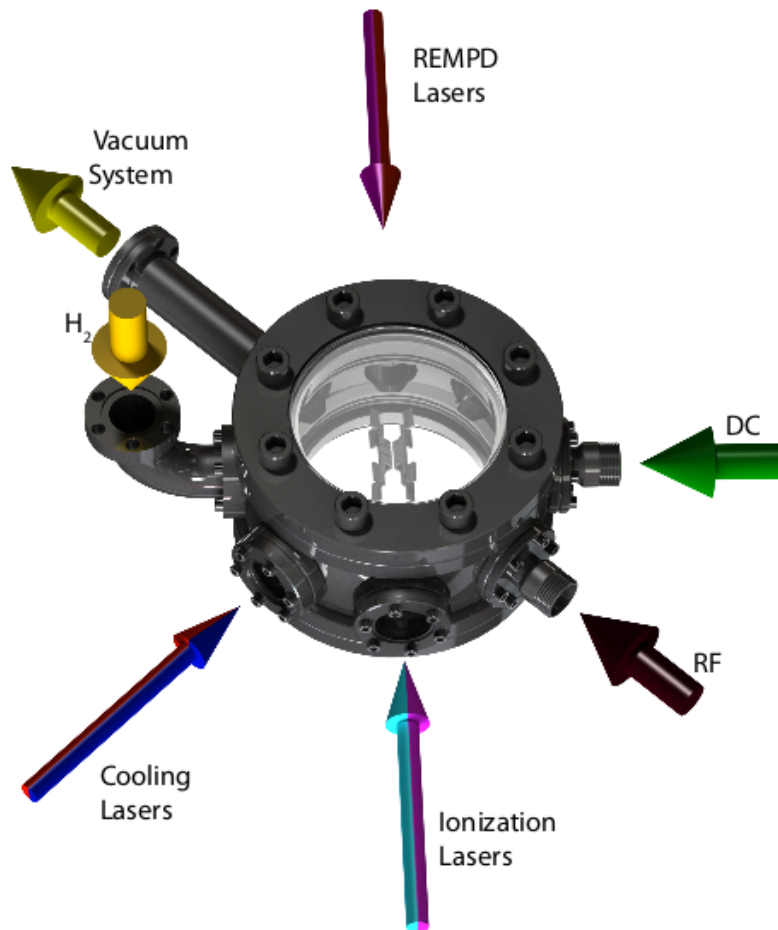
Figure 1.2: An example of a simple RF trap used in this work.

Cold ions in Paul traps yield ordered ion arrangements called Coulomb crystals, which provide many supplementary benefits [9, 11, 17, 19, 87]. Coulomb crystals are near-still ordered structures of ions [4, 10, 13, 17, 19]. This close proximity provides a higher density with less ions and a large spatial localization [10, 11, 17, 106]. The ions are within range of weak Coulomb forces, which aids sympathetic cools and possible elimination of the motional modes, which may lead to removing Doppler broadening [39, 106]. By definition, these crystals are at ultracold temperatures which contributes to immaculate testing environments and longer ion storage times [10, 11, 17, 106, 107]. Coulomb crystals reduce Dopplers shift and allow measurement of narrow electronic transitions or allow access to previously forbidden/obscured transitions [38, 39, 79, 98, 106, 107].

7

Furthermore, they are molecular detectors through fluorescence, since Ca^+ has an optical fluorescence and CaH^+ does not [19, 47, 106], as seen in **Figure 1.3**. Exciting over Ca^+'s optical transition indicates the presence and quantity of CaH^+ [19, 76, 106]. Coulomb crystals have other applications in reaction dynamics [8, 9, 11, 17, 19, 21, 25, 27, 28], cold chemistry [8, 11, 17, 20, 21], non-linear dynamics, testing quantum jumps, quantum information, quantum simulations, mass-to-charge ratios, state-detection, etc. [11, 14, 17, 19].
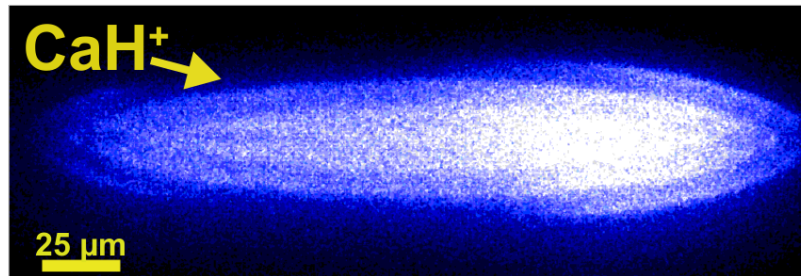
Figure 1.3: A Coulomb crystal containing Ca+, the lit areas and CaH+, the darker areas in the center [108].

1.2 Ion State-Selection/Cooling

Ions traps are ideal experimental setups for quenching the external degrees of freedom and cooling to the ground motional state [11, 17, 20, 32, 38, 80, 86, 107]. State-selection to the ground motional state includes cooling and sideband cooling [76, 77]. Basic molecular cooling techniques reduces the external degrees of freedom, which in turn cools the ions to cold (<1 K) and ultracold (<1 mK) temperatures. Including sideband cooling reduces the motional modes which minimizes the first and second-order Doppler shifts [11, 17, 56, 57, 73–75, 79, 107]. In general, cooling has additional applications in quantum computing, quantum simulations, and cold chemistry [8, 11, 13, 15]. Atoms are generally easier to cool, since molecules lack the necessary closed internal transitions [11, 103, 109, 110]. For example, Ca^+ is easily cooled using direct laser cooling [32, 76]. However, molecules may potentially reach lower temperatures [76]. Both atomic and molecular

cooling centers around a few modern techniques such as cryogenic cooling, molecular beam deceleration, cavity-enhanced laser cooling, direct laser cooling [13, 79, 91, 104, 109], Doppler cooling [11, 38, 77, 82, 88, 105, 110, 111], sympathetic cooling [9, 13, 16, 20, 25, 28, 32, 47, 76, 77, 80, 86, 88, 90, 92, 99–101], and buffer gas cooling [83, 86, 94, 98, 103]. Doppler cooling may induce Doppler shifts during spectroscopy, and is subjected to the Doppler cooling limit [11]. Cavity-enhanced laser cooling only applies to solids, while cryogenic cooling applies to liquids. Both of these methods cannot achieve ultracold temperatures [11, 83]. Buffer gas cooling requires an external collision beam and molecular beam deceleration requires an external field, which may interfere with ongoing experimentation or push ions out of the trap [107]. CaH^+ not only lacks a closed optical transition but also has a rich rovibronial structure at room temperature, which eliminates direct laser cooling, since it would require a number of repumping lasers which interferes with fluorescence detection. Ultimately, sympathetic cooling of CaH^+ uses co-trapped Ca^+ as a coolant to cools the external degrees of freedom below mK temperatures through the Coulomb interaction. CaH^+ has a known cooling scheme to the motional ground state [32, 47, 76], and large vibrational spacing which means a majority population will be the ground vibrational state at room temperature.

Cooling to the ground motional state is insufficient state-selection for high-precision spectroscopy of molecules. State-selecting the rovibronic state of CaH^+ is necessary to reduce cross-talk interference within measurements. In addition, internal cooling promotes cooling to even colder temperatures than pure external cooling, since external cooling depends on the proportion of a damping force stimulating the absorption-emission cycle. While cooling external degrees of freedom is well-known, cooling the internal degrees of freedom in molecules is a much more complex process. Sympathetic cooling leaves the internal temperature at the same temperature of the surrounds. The same weak Coulomb interactions between neighboring ions, which make sympathetic cooling possible, make molecules susceptible to heating of the rovibrational distribution due to

stray fields such as blackbody radiation excitations [17, 19, 33, 38, 86, 98, 103]. Internal cooling must compete against blackbody radiation heating to maintain any state-selection. Literature contains several methods for other molecules, most of which are modifications of external cooling techniques: state-selective photoionization [4, 17, 90, 106, 110], laser cooling [59–61, 109], optical pumping [17, 33, 60, 89, 110, 112, 113], buffer gas cooling [62, 83], probabilistic state preparation [35], sympathetic cooling with laser-cooled atoms [63, 86], molecular collisions [83], cryogenic cooling [66], and quantum logic spectroscopy [35, 78, 104]. As with external cooling, laser cooling, optical pumping, buffer gas cooling, molecular collisions, and cryogenic cooling are not possible with CaH^+ due to various experimental limitations. State-selective photoionization occurs before trapping, which is experimentally difficult for CaH^+. Probabilistic state preparation, quantum logic spectroscopy, and sympathetic cooling require detailed spectroscopic knowledge. Selecting a specific scheme for CaH^+ requires preliminary knowledge the specific transitions excited [107], which currently does not exist.

1.3   High-Precision Spectroscopy of Ions

All of CaH^+'s potential applications (e.g. astrochemistry, molecular clocks, rovibronic state-selection, quantum logic spectroscopy, and fundamental constant measurements) require high-precision measurements of its transition frequencies and energy levels [15]. Molecules have a variety of laser-based spectroscopic techniques available to them: photodissociation [83], resonance enhanced multiphoton dissociation (REMPD) [11, 17, 33, 38, 39, 75, 89, 90, 93, 95, 103, 114], resonance enhanced multiphoton ionization (REMPI) [11, 106], quantum logic spectroscopy (QLS) [35, 38, 63, 78, 79, 91, 104], light induced charge transfer (LICT) [90], quantum jump spectroscopy [50, 104], Laser-cooled fluorescence mass spectrometry (LCFMS) [99–102, 114], and laser-induced fluorescence [32, 73, 74]. Photodissociation does not provide the required transition frequencies. REMPI and LICT require changing the charge of CaH^+, which would remove it

completely from the trap. Recreating the Coulomb crystal for every data point is unrealistic. Laser-induced fluorescence requires a second detector for the non-optical CaH^+ emissions and longer/more photon pulses to achieve adequate signal to noise ratios [102]. Laser-cooled fluorescence mass spectrometry determines the charge-to-mass ratio of the target ion, but works best with only two atoms, not Coulomb crystals. This dissertation executes [1 + 1'] REMPD on CaH^+ since the process can be easily detected through fluorescence in a Coulomb crystal [76]. The exact dissociation scheme is unknown at the time of writing, which leads to many potential difficulties when interpreting spectra.

Unlike dissociation, quantum logic spectroscopy is a non-destructive approach which measures changes in motional energy through fluorescence of a control ion to obtain a spectrum. This process is precise than REMPD experiments, since it amplifies weak signals and transitions that are experimentally obscured. Schmidt et al. introduced quantum logic spectroscopy using a logical Be^+ ion to measure transitions in the hard to cool spectroscopic Al^+ ion [63]. Koelemeij et al. proposed a procedure using one molecular ion and clock ion, CO^+, for blackbody radiation thermometry using modulated optical dipole force (MODF) [38]. Chou et al. used a logical Mg^+ ion to measure the transitions of Al^+ to apply to optical clock [91]. Hume et al. worked with a logical Mg^+ ion to detected the clock states of Al^+ [104]. Wan et al. employed a logical Mg^+ ion to precisely measure transitions in Ca^+ with an amplified signal [79]. Wolf et al. utilized a logical Mg^+ ion to distinguish rotational states in MgH^+ [78]. Chou et al. implemented a procedure with a logical Ca^+ to help prepare and detect quantum states in CaH^+ [35]. QLS requires good estimations of the transitions before hand, however, the CaH^+ transitions, especially for excited electronic states, have never been experimentally measured before this collective work. The results from this dissertation will hopefully lead to future QLS experiments.

11

1.4 Dissertation Layout/Organization

The rest of the thesis is organized as follows: chapter 2 characterizes the theoretical methodology; chapter 3 presents initial data on the $1^1\Sigma \longrightarrow 2^1\Sigma$ vibronic transitions; chapter 4 describes efforts to distinguish rovibronic transitions withing the previously found vibronic transitions; chapter 5 reports other applications of the model to CaH$^+$ experiments; chapter 6 recounts a divergent project involving quantifying errors for quantum information; and chapter 7 outlines the main conclusions and various future experiments.

Table 1.1: Full Constants Table

Constant	Meaning
ε_0	Vacuum permittivity in $\frac{C^2}{Jm}$
h	Planck's constant in Js
c	Speed of light in m/s
k	Boltzmann's constant in J/K
T	Temperature in Kelvin
N_a	Avogadro's number
n	Electronic quantum number
v	Vibrational quantum number
J	Rotational quantum number
$E(n,v,J)$	Zero point total energy for state n, v, J in cm^{-1} **Equation 2.1**
$T(n)$	Zero point electronic energy for state n in cm^{-1}
$G_n(v)$	Zero point vibrational energy for state n, v in cm^{-1} **Equation 2.1**
$F_{n,v}(J)$	Zero point rotational energy for state n, v, J in cm^{-1} **Equation 2.1**
ω_n	Harmonic constant for state n in cm^{-1}
$\omega\chi_n$	Anharmonicity for state n in cm^{-1}
$B_{n,v}$	Rotational constant for state n, v in cm^{-1}

Table 1.1: (continued)

$D_{n,v}$	Rotational distortion constant for state n, v in cm^{-1}
$\nu_{n',v',J'\leftarrow n,v,J}$	Transition frequency in m^{-1} **Equation 2.2**
Ω	Dissociation cross section in m^2 **Equation 2.17**
$\Gamma_{n',v',J'\leftarrow n,v,J}$	Transition rate in s^{-1} **Equation 2.10**
$A_{n',v',J'\leftarrow n,v,J}$	Einstein A in s^{-1} **Equation 2.4**
$B_{n',v',J'\leftarrow n,v,J}$	Einstein B in $\frac{s}{kg}\frac{kg}{s^2}$ **Equation 2.6**
$p(n, v, J)$	Probability of being in state n, v, J in $\frac{J}{m^3}$
$N_{n,v,J}$	Population of state n, v, J
$\mu_{n',v',J'\leftarrow n,v,J}$	Transition/permanent dipole moment in Cm
$g(\nu_{n',v',J'\leftarrow n,v,J})$	Laser intensity in J/m^2 **Equation 2.11**
f_0	Laser center frequency in cm^{-1}
I_0	Peak laser intensity in J/m^2
$FWHM$	Laser linewidth (full width at half maximum) in cm^{-1}
σ	Laser linewidth (variance) in cm^{-1}

CHAPTER 2

THEORETICAL MODEL

The theoretical model imitates experiments by applying lasers on and off, detecting throughout, and fitting to an exponential rate. Three different versions of the dissociation software currently exist: a simple model, a full simulation model, and a Hamiltonian model. The simple model is best suited to quick estimations and optimization calculations due to it's simplicity and efficiency. The full-simulation model accounts for competing reactions within the system, but takes significantly longer due to the matrix ordinary differential equation (ODE). The Hamiltonian model calculates dissociation directly from the potential energy surface (PES) curves and dipole moment curves. While this method is the most commonly used method in literature, this dissertation does not implement Hamiltonians due to incorrect CaH^+ PES curves.

2.1 Calculating Transition and Dissociation Rates

Within the simple and full-simulation models, transitions rates illustrate intra-molecule state transitions, while dissociation rates signify transitions from CaH^+ to Ca^+ + H. Transitions rates (e.g. spontaneous emission, black-body radiation stimulated transitions, laser induced transitions, etc.) indicate absorption or emission of photons due to numerous energy sources (e.g. black-body radiation, lasers, etc.). Dissociation rates (e.g. laser induced dissociation) depict absorption of photons from a laser, only. Both of these rate types represent a change of the population of a particular quantum state at each time step. The theoretical model must account for all possible rates and all possible states depending on the laser frequency, **Figure 2.1**. The quantitative rates originate from various sources such as LEVEL [115], BCONT [116–118], and the formulas listed below.
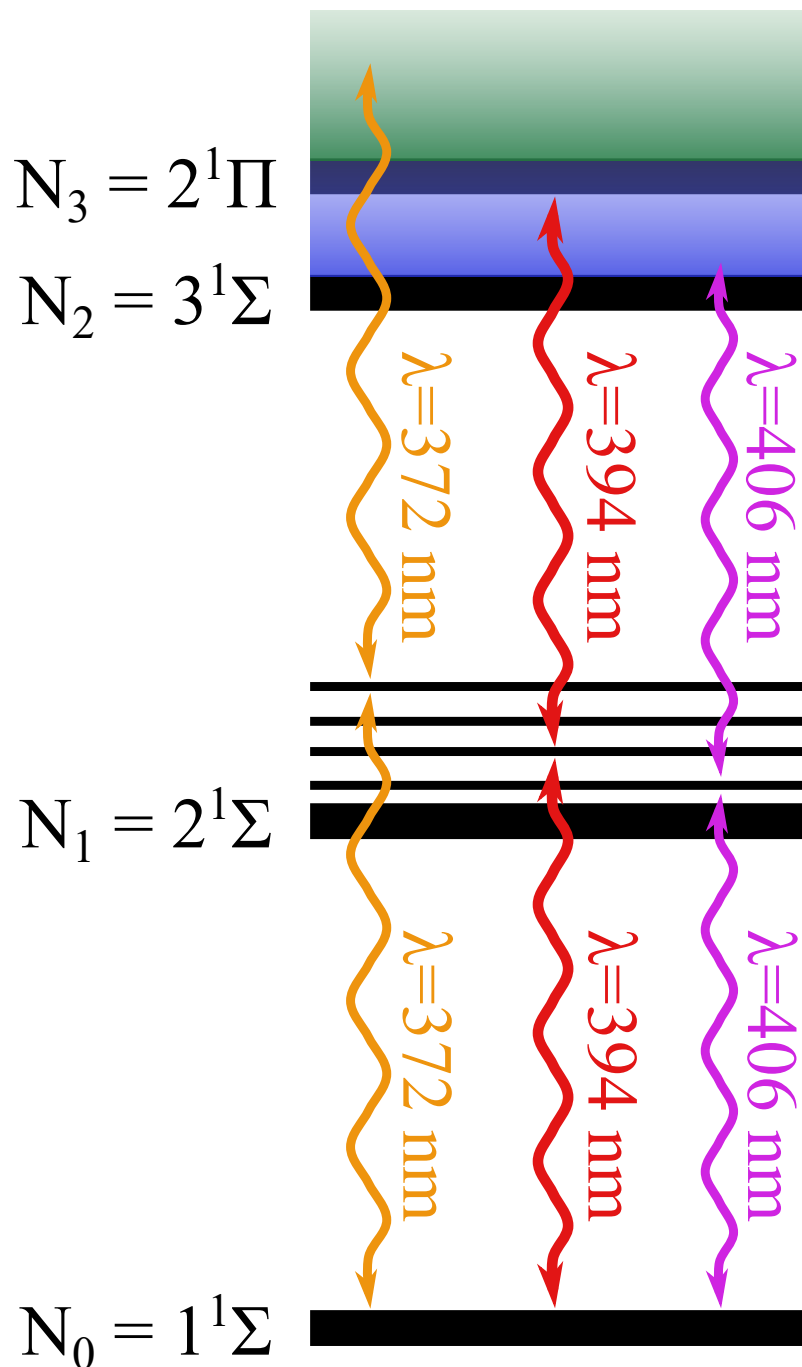
Figure 2.1: A three level diagram for CaH$^+$ with two bound states ($1^1\Sigma$ and $2^1\Sigma$) and two dissociative states ($3^1\Sigma$ and $2^1\Pi$). A laser tunes from 370nm to 420nm, which excites the molecule from the ground state to a transition state, and eventually to a dissociation state.

The models designate each energy level using quantum numbers (i.e. n, v, J) and physical constants, **Equation 2.1**. The Born-Oppenheimer approximation separates the

electronic energy, $T(n)$, from the internal energy, $G_n(v) + F_{n,v}(J)$:

$$E(n, v, J) = T(n) + G_n(v) + F_{n,v}(J), \tag{2.1}$$

where

$$G_n(v) = \omega_n(v + \frac{1}{2}) - \omega\chi_n(v + \frac{1}{2})^2 + \mathcal{O}((v + \frac{1}{2})^3),$$

and where

$$F_{n,v}(J) = B_{n,v}(J(J+1)) - D_{n,v}(J(J+1))^2 + \mathcal{O}((J(J+1))^3).$$

The rotational constants depend on the vibronic quantum numbers, which accounts for internal crossing from rovibrational affects. Representing the vibrational and rotational energy terms as individual Taylor series means storing less information, the simulations are more efficient, and the potential energy surface can be derived from experimental constants. However, this representation loses accurate with fewer terms, and any initial guesses must come from theoretical PES curves. Typically, LEVEL calculates an all initial guesses for these physical constants [115], but some constants emanate from previous literature [1, 2, 27, 43, 44].

2.1.1 Transitions

The strength of a transition depends on two main factors: the frequency shift and the dipole moment [119–121]. When molecules shift from one bound state to another, the energy change produces a photon corresponding to the difference in frequency:

$$\nu_{n',v',J' \leftarrow n,v,J} = |E(n', v', J') - E(n, v, J)|. \tag{2.2}$$

Due to the anharmonicity in the potential well, there are no selection rules for vibrational transitions. Rotational transitions still follow the $J' = J \pm 1$ rule, in these models. For

a diatomic molecule, $J' = J$ is not allowed. In this dissertation, LEVEL [115] calculates $\lambda = T(n') + G_{n'}(v') - T(n) - G_n(v)$ from PES curves provided by Abe et al. [2]. Abe et al. provide additional initial ground-state frequencies ($n = 0$) in an early paper [1]. The dipole moment (e.g. permanent dipole or transition dipole) represents the overlap between two quantum states and the probability of transitions from one state to another. Transitions occurring within the same electronic state use the permanent dipole moment, while transitions occurring between electronic states use a transition dipole moment. These dipole moments originate from various literature sources [2, 27]. To calculate transition rates, the last factor needed is the absorption/gain coefficient from the stimulation source (e.g. black-body radiation, lasers, etc.) [119–121].

Spontaneous emission is the process whereby a molecules decays from a higher energy level to a lower energy level by spontaneously emitting a photon [119–122]. LEVEL directly calculates the spontaneous emission transition rate, i.e. Einstein A, without the rotational dependence [115], and this Einstein A directly relates to the change in state population [38, 119–125]:

$$\frac{dN_{n',v',J'}}{dt} = A_{n',v',J' \leftarrow n,v,J} N_{n,v,J}. \tag{2.3}$$

To include the rotational dependence, the model manually determines each Einstein A dependent on the transition dipole moment, μ, [119–122, 126]. The exact formula depends on whether the angular momentum is higher or lower in the final state, which is described by the Hönl-London factor [127]:

$$A_{n',v',J-1 \leftarrow n,v,J} = \frac{16\pi^3 J}{3\varepsilon_0 h(2J+1)} \nu_{n',v',J-1 \leftarrow n,v,J}^3 \mu^2, \tag{2.4}$$

or

$$A_{n',v',J+1 \leftarrow n,v,J} = \frac{16\pi^3 (J+1)}{3\varepsilon_0 h(2J+1)} \nu_{n',v',J+1 \leftarrow n,v,J}^3 \mu^2.$$

This rotational factor accounts for the degenerate populations of J.

Stimulated emission and absorption is the process of a simulation sources changing the molecular energy level by stimulating decaying or growing from one energy level to another using a photon [119–125]. Black-body radiation (BBR) stimulated emission/absorption transition rates, i.e. Einstein B, is the simulated rate using photons originating from BBR. Many texts write the stimulated rate as $B_{n',v',J'\leftarrow n,v,J}\rho(\nu_{n',v',J'\leftarrow n,v,J})N_{n,v,J}$ where $\rho(\nu_{n',v',J'\leftarrow n,v,J})$ is energy density per unit angular frequency interval [119–125]. For simplification, this dissertation uses $B_{n',v',J'\leftarrow n,v,J}$, where the energy density of the simulation source is combined with the Einstein B [119–122]:

$$\frac{dN_{n',v',J'}}{dt} = B_{n',v',J'\leftarrow n,v,J}N_{n,v,J}. \tag{2.5}$$

There are two types of Einstein Bs: stimulated emission from a higher level to a lower level [38, 119–126] :

$$B_{n',v',J'\leftarrow n,v,J} = A_{n',v',J'\leftarrow n,v,J}\frac{1}{\exp(\frac{ch\nu_{n',v',J'\leftarrow n,v,J}}{kT}) - 1}, \tag{2.6}$$

and stimulated absorption from a lower level to a higher level [38, 119–122]:

$$B_{n,v,J\leftarrow n',v',J'} = A_{n',v',J'\leftarrow n,v,J}\frac{1}{\exp(\frac{ch\nu_{n',v',J'\leftarrow n,v,J}}{kT}) - 1}\frac{2J+3}{2J+1}. \tag{2.7}$$

The simulations calculate all Einstein Bs within the program, and sample rates are shown in **Figure 2.2**.
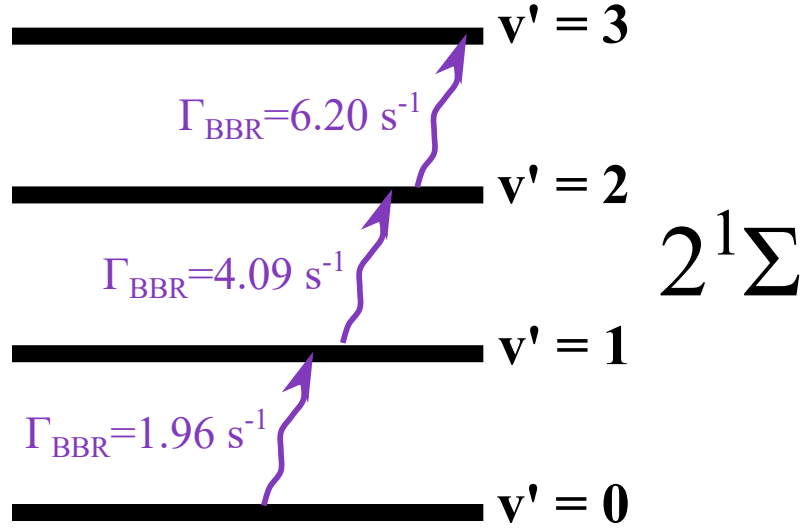
Figure 2.2: Example of Black Body Radiation stimulated absorption rates for the $2^1\Sigma$ state of CaH$^+$.

Laser stimulated transition rates are similar to Einstein Bs, but the simulation source is a laser instead of BBR [123, 124, 128]:

$$\frac{dN_{n',v',J'}}{dt} = \Gamma_{n',v',J'\leftarrow n,v,J} N_{n,v,J}. \tag{2.8}$$

Unlike before, stimulated emission is equivalent to stimulated absorption, regardless of the rotational population. The transition rate depends on a convolution between the laser profile ($g(\nu_{n',v',J'\leftarrow n,v,J})$) and the transitions profile ($f(\nu_{n',v',J'\leftarrow n,v,J})$) [124, 129]:

$$\Gamma_{n',v',J'\leftarrow n,v,J} = \frac{A_{n',v',J'\leftarrow n,v,J}}{8\pi\hbar c\nu^3_{n',v',J'\leftarrow n,v,J}} \int g(\nu_{n',v',J'\leftarrow n,v,J}) f(\nu_{n',v',J'\leftarrow n,v,J}) d\nu. \tag{2.9}$$

If one of spectral lines is significantly smaller than the other, the rate simplifies. In the case of this dissertation, the laser linewidth is much wider than any transition linewidth, which simplifies the rate [123, 124, 128]:

$$\Gamma_{n',v',J'\leftarrow n,v,J} = \frac{A_{n',v',J'\leftarrow n,v,J}g(\nu_{n',v',J'\leftarrow n,v,J})}{8\pi hc^2\nu^4_{n',v',J'\leftarrow n,v,J}}. \tag{2.10}$$

The experiments, in this dissertation, use a Gaussian laser to describe the laser profile [123, 124, 128, 130]:

$$g(\nu_{n',v',J'\leftarrow n,v,J}) = I_0 \frac{2\sqrt{\ln(2)}}{\pi FWHM} \exp\left(\frac{-4ln(2)(\nu_{n',v',J'\leftarrow n,v,J} - f_0)^2}{FWHM}\right). \qquad (2.11)$$

Since these rates change based on the frequency of the laser, the exact rates are recomputed for each data point in the spectrum.

While not relevant to any experiment in this dissertation, multi-photon laser induced transitions may occur. Karr et al. defines two-photon transitions where a_0 is the Bohr radius, Γ_f is instrumental transition width, μ_{2ph} is the two-photon transition matrix element [93, 95]:

$$\Gamma_{2ph} = \frac{64\pi^2 a_0^6}{\hbar c \Gamma_f} \mu_{2ph}^2 I_0^2. \qquad (2.12)$$

Ketterle et al. defines the transition differently, where A_{2ph} is the two-photon rate:

$$\Gamma_{2ph} = \frac{8\pi^3}{\hbar^4 c^2} A_{2ph} g(\nu_{n',v',J'\leftarrow n,v,J}). \qquad (2.13)$$

The calculation of μ_{2ph} or A_{2ph} depends on the proximity to an intermediate transition state. Off-resonance transitions involve transitioning to ghost state, while on-resonance transitions use an already existing state. Formulas alone are not sufficient to calculate these transitions. The calculations involve integrating the overlap between PES curves, multiple dipoles, and a dependence on the laser profile.

2.1.2 Dissociation

The dissociation process utilizes a photon to separate a molecule into its atomic comportments. As with transitions, dissociation rates depend on the dissociation frequency and dipole moment. In CaH^+, the electron excites to a weakly-bound state and

dissociates to Ca^+ and H:

$$\nu_{\infty \leftarrow n,v,J} = |E_{Ca} + E_H - E(n,v,J)|. \qquad (2.14)$$

The exact quantum states of the individual Ca^+ and H are currently unknown. Each dissociative state has either no potential well or a small one, therefore dissociation is continuous and can occur anywhere within scope of the electronic state. This removes the need to dissociate to a particular rovibrational state. Since dissociation occurs at the electronic transition level, the dipole moment is always a transition dipole moment. As before, literature contains all of the necessary dipoles [2, 27]. The dissociation simulations assumes BBR cannot dissociate without help from the laser, and that no association process is re-forming CaH^+.

Laser induced dissociation uses a Gaussian laser to dissociate CaH^+ from a transition state to a dissociate state:

$$\frac{dN_\infty}{dt} = \Gamma_{\infty \leftarrow n,v,J} N_{n,v,J}. \qquad (2.15)$$

The exact rate depends heavily on the dissociation cross section, Ω_ν:

$$\Gamma_{\infty \leftarrow n,v,J} = \frac{\Omega_\nu}{hc}. \qquad (2.16)$$

The cross section integrates the overlap between two states, which is calculated through BCONT. The BCONT program calculates molar extinction coefficient spectra, $\epsilon_s(\nu)$, using PES and dipole moment curves [116–118]. This coefficient gives the dissociation cross section which in turn provides the overall dissociation rate, **Equation 2.16** [131, 132]:

$$\Omega_\nu = \frac{\log(10)}{10 N_a} \int \frac{\epsilon_s(\nu_{\infty \leftarrow n,v,J}) g(\nu_{\infty \leftarrow n,v,J})}{\nu_{\infty \leftarrow n,v,J}} d\nu_{\infty \leftarrow n,v,J}. \qquad (2.17)$$

Since dissociation is continuous over the entire laser range, the rate is a convolution of the extinction coefficient spectrum with the laser profile.

21

While possible in some CaH$^+$ experiment, multi-photon laser induced dissociation is not included in the simulations, as of yet. As with single photon transitions, two-photon transitions depend on a dissociation cross section, **Equation 2.16** [131, 132]. This constant depends transition matrix element which comes from the overlap between multiple PES curves. As these elements have a dependence on the laser profile and are not yet available in literature, these dissociation rates have been excluded from simulations. As with multi-photon transitions, multi-photon dissociation can be either on-resonance or off-resonance. On-resonance dissociation will make peaks in the spectrum wider or double-peaked, while off-resonance dissociation will provide new peaks previously unaccounted for. This means multi-photon dissociation will appear as unaccounted for data in the spectrum.

2.2   Full - Simulation Model

The full-simulation method uses a transition rate matrix, i.e. a continuous-time Markov chain, to coalesce information about the probability of a molecules shifting between quantum states at each time step. This implies all states are discrete from each other. **Equation 2.18** shows the rate matrix M affecting the population vector, P, as a matrix ordinary differential equation (ODE):

$$\frac{d\mathbf{P}}{dt} = \mathbf{M}\,\mathbf{P}. \tag{2.18}$$

M contains all rates previous mentioned in **Section 2.2**, and the simulations assume that there are no other unaccounted rates occurring. The initial P assumes all CaH$^+$ molecules start in the ground vibronic state, but in a thermally distributed rotational state. As later results will prove false, the models assumes the potential well for each PES curve matches theory predictions from Abe et al. [2].

2.2.1 Forming Transition Rate Matrix

The matrix is formed by mapping all possible transitions to a transformation in the matrix. The simulation accounts for and summates all cross-competing reactions. Two examples of all rates that affect a single population are listed below. The first example only includes rotational rates, without vibrational or electronic transitions. The second example includes the previous rates plus possible vibrational transitions.

$$
\begin{aligned}
\frac{dN_{v,J}}{dt} \; + = \; & A_{v,J+1\to v,J}N_{v,J+1} + B_{v,J+1\to v,J}N_{v,J+1} - B_{v,J\to v,J+1}N_{v,J} \\
& - A_{v,J\to v,J-1}N_{v,J} - B_{v,J\to v,J-1}N_{v,J} + B_{v,J-1\to v,J}N_{v,J-1} \quad (2.19)
\end{aligned}
$$

$$
\begin{aligned}
\frac{dN_{v,J}}{dt} \; + = \; & \sum_{v_2>v} A_{v_2,J+1\to v,J}N_{v_2,J+1} + \sum_{v_2>v} B_{v_2,J+1\to v,J}N_{v_2,J+1} + \\
& \sum_{v_2>v} A_{v_2,J-1\to v,J}N_{v_2,J-1} + \sum_{v_2>v} B_{v_2,J-1\to v,J}N_{v_2,J-1} - \\
& \sum_{v_2>v} B_{v,J\to v_2,J+1}N_{v,J} - \sum_{v_2>v} B_{v,J\to v_2,J-1}N_{v,J} + \\
& \sum_{v_1<v} B_{v_1,J+1\to v,J}N_{v_1,J+1} + \sum_{v_1<v} B_{v_1,J-1\to v,J}N_{v_1,J-1} - \\
& \sum_{v_1<v} A_{v,J\to v_1,J+1}N_{v,J} - \sum_{v_1<v} B_{v,J\to v_1,J+1}N_{v,J} - \\
& \sum_{v_1<v} A_{v,J\to v_1,J-1}N_{v,J} - \sum_{v_1<v} B_{v,J\to v_1,J-1}N_{v,J} \quad (2.20)
\end{aligned}
$$

The program will always check that the constructed matrix for simulations is mathematically sound. The diagonal of the matrix should contain only non-positive numbers, $0 \leq -M_{ii} \leq \infty$, $\forall\, i$. All other elements of the matrix should be non-negative, $0 \leq M_{ij} \; \forall\, i,j \; where \; i \neq j$. Each row must summate to zero, $\sum_j M_{ij} = 0 \; \forall\, i$, which implies that the entire matrix should also add to zero, $\sum M_{ij} = 0 \; \forall\, i,j$. The last rule is that the diagonal element in each row should be equal to all other elements,

$-M_{ii} = \sum_j M_{ij}, \; where \; i \neq j.$ The last two rules present a problem in modern computers. Each memory slot can only store a finite number of decimal places, which changes depending on the computer resources. If two rates of greatly different magnitudes are added together, then the smaller number would be rounded out. Therefore, the simulation excludes transition rates smaller than a specified threshold. For our CaH^+ experiments, the laser rate is relatively high, therefore this limitation removes all black-body radiation transitions and majority of the spontaneous emission transitions.

2.2.2 Extracting Fluorescence Curve

Experiments detect the percentage of dissociated CaH^+ by the amount of fluorescing Ca^+. These experiments determine the rate from fitting the fluorescence vs. time curve to a first-order rate equation. The transition rate matrix reproduces this same curve through numerical integration:

$$Intensity(t) = N_\infty(t). \tag{2.21}$$

Integrating the matrix ODE gives, $\mathbf{P}(t)$, changes in state population over time, but due to the complexity of the matrix, this cannot be done efficiently analytically. Numerical integration provides the same information without complex SVU decompositions and boundary-condition problems. This procedure requires two factors: a time step, dt, and a numerical integrator.

The time-step is carefully chosen to produce the spectrum accurately and efficiently. To ensure that the total population stays normalized at each time step, dt must be less than the largest matrix element:

$$\frac{1}{dt} \leq \max(-M_{ii}) \, \forall \, i. \tag{2.22}$$

To ensure more than one point on the fluorescence curve, the time step should be less than the experiment time:

$$dt \leq \frac{t_{max}}{100}.$$

The simulations use Runga-Kutta (RK4) as the numerical integrator due to its robustness and easy of implementation. This integrator is implemented step-wise through a C++ library called ODEINT [133]. While numerical integration gives $\mathbf{P}(t)$, only the last element in the vector, $N_\infty(t)$, is the true fluorescence curve. This implies that the majority of $\mathbf{P}(t)$ is not stored in memory, which reduces overall resource costs.

```
rk.do_step(Eq. 1, P, start time, dt)
```

2.2.3   Determining Dissociation Rate

After generating the fluorescence curve, the next step is extracting the overall dissociation rate. Experiments fit the fluorescence curve to an exponential decay equation, therefore simulations strive to imitate this strategy:

$$Intensity(t) = N_\infty(t) = 1.0 - \exp(-\Gamma t). \tag{2.23}$$

Since dt is inversely proportional to the laser intensity, large intensities consume amplitude computing resources. To ensure dissociation, experiments use high intensities, beyond the computing capabilities of simulations. Studying regimes will reveal procedures that produce equivalent results without wasting resources. The simulations consider multiple procedures for extracting the overall rate such as fitting, expectation value formulas, and stochastic procedures.

Regimes studies analyze different methods and ensure accuracy compared the simple model, **Section 2.3**. At very low laser intensities, laser-induced transitions are weaker than competing Einstein As and Bs. In a spectrum, this would appear as a negligible peak. Based on theoretical studies for CaH^+, this regime is typically $<1.0e9\ \frac{W}{m^2}$. At intermediate intensities, laser transitions are directly competing with Einstein As and Bs, which gives no guarantee on peak shape. Theory puts this regime between 1.0e9 and 1.0e14 $\frac{W}{m^2}$. With very high intensities, the laser renders the Einstein As and Bs negligible due to

the large difference in magnitudes. This is the case and peak shape seen in experiments, and therefore the simple model is based of this assumption. Theoretical estimations place this regime at $>1.0e14 \frac{W}{m^2}$.

The most true to form method to find the dissociation rate would involve fitting the fluorescence curve to the same exponential as experiments:

$$N_\infty(t) = A - B\exp(-\Gamma t). \tag{2.24}$$

In this equation, A and B are additional fitting parameters to account for the initial fluorescence and the limited experiment time. This method properly predicts the peak shape and behavior at all regimes, **Figure 2.3**. Since it implements the same method as experiments, any discrepancies will be consistent in both experiments and simulations. While low intensities do not predict all behavior correctly, the intermediate and high intensities produce equivalent results. However, this method presents a big disadvantage: the fitting step. To preform regression, the entire fluorescence curve must be stored locally and then optimized, which is resource and time intensive. Due to this fact, the method is worthless at high intensities, and untimely at intermediate intensities.
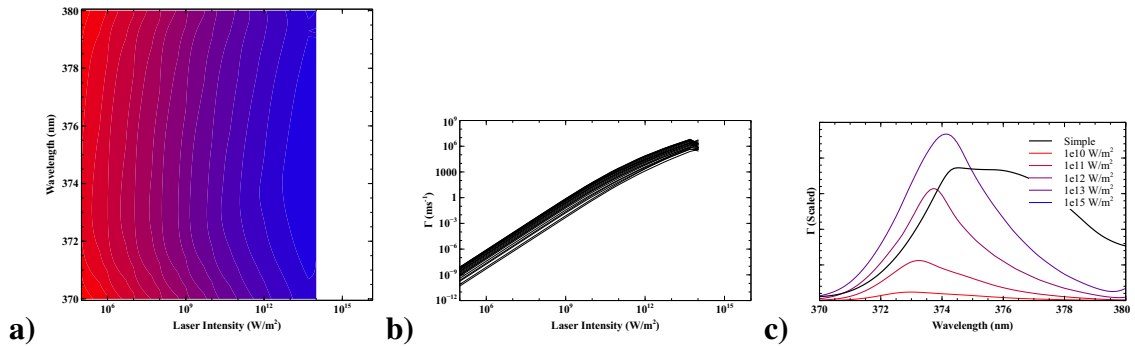
Figure 2.3: Single dissociation peak generated using **Equation 2.23**. Three different view points of the same data are provide. **a)** A contour plot where the bluer areas of the contour plot indicate a higher rate. **b)** A side-view of contour plot where each line in the side-view plot is a different laser positions (ranging from 370 nm to 380 nm). **c)** A standard spectrum with scaled low intensity, middle intensity, highest intensity, and simple model rates, **Equation 2.41**. t_{max} = 4.0e-3 s, σ = 1.1074 nm.

An alternative to fitting is the expectation value for time of dissociation. In this case, the rate is inversely proportional to the average lifetime:

$$\frac{1}{\Gamma} = <t> = \sum_{t=0}^{t=max\_time} tP_{\infty}(t).$$

(2.25)

This expectation value comes from treating $N_{\infty}(t)$ as a cumulative distribution function (CDF). The probability distribution function (PDF) at any time, t, is the derivative of the CDF, $P_{\infty}(t)$. Unlike before, this method does no require any addition resources since the rate can be computed as the fluorescence curve is generated. Regrettably, the peak shape does not match the simple model at any regime, **Figure 2.3**. The rates are inversed at low intensities, the peak is a double peak at intermediate intensities, and the peak is right shifted at high intensities. This method is ineffective at all regimes.
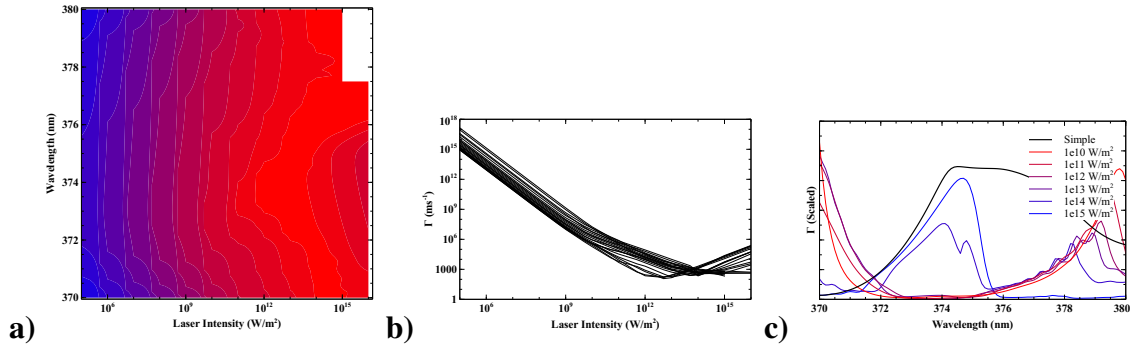
Figure 2.4: Single dissociation peak generated using **Equation 2.25**. Three different view points of the same data are provide. **a)** A contour plot where the bluer areas of the contour plot indicate a higher rate. **b)** A side-view of contour plot where each line in the side-view plot is a different laser positions (ranging from 370 nm to 380 nm). **c)** A standard spectrum with scaled low intensity, middle intensity, highest intensity, and simple model rates, **Equation 2.41**. t_{max} = 4.0e-3 s, σ = 1.1074 nm.

Another alternative is the expectation value for rate of dissociation. The rate is proportional to average dissociation rate:

$$\Gamma = \sum_{t=dt}^{t=max\_time} \frac{1.0}{t} P_{\infty}(t).$$

(2.26)

27

As with the other alternative method, this method requires no addition computing resources. Fortunately, the peak shape and behavior matches both the simple model and the fitting method at intermediate and high intensities, **Figure 2.3**. Similar to the fitting method, the peak behavior does not match perfectly at low intensities. There is also a small scale factor between this method and the fitting method.
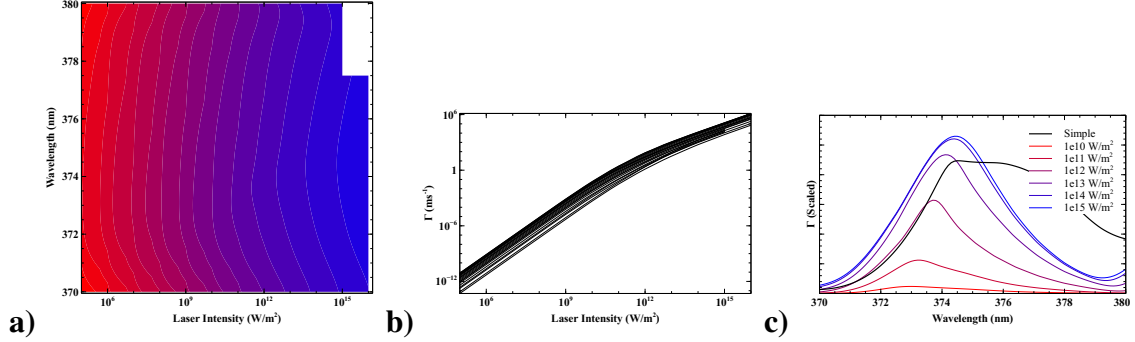
Figure 2.5: Single dissociation peak generated using **Equation 2.26**. Three different view points of the same data are provide. **a)** A contour plot where the bluer areas of the contour plot indicate a higher rate. **b)** A side-view of contour plot where each line in the side-view plot is a different laser positions (ranging from 370 nm to 380 nm). **c)** A standard spectrum with scaled low intensity, middle intensity, highest intensity, and simple model rates, **Equation 2.41**. t_{max} = 4.0e-3 s, σ = 1.1074 nm.

The last alternative is a stochastic method to iterate through the transition rate matrix. In this process, the simulations use a number of iterations, max_i, to stochastically average the overall rate:

$$\Gamma = \frac{1.0}{max\_i} \sum_{i=0}^{i=max\_i} \frac{1.0}{\Gamma_i}.$$

(2.27)

Each iteration moves from quantum state to quantum state depending on the probability of transition, i.e. transversing through a Markov chain:

$$P(i \leftarrow j) = \frac{M_{ij}}{\sum_{k=0}^{k=max} M_{ik} \forall i \neq k}.$$

(2.28)

The final rate depends on the summation of all of these individual probabilities:

$$\Gamma_i = \sum \frac{1.0}{M_{ij}}. \tag{2.29}$$

This method produces similar results to the fitting method, even though the method does not technically produce a florescence curve. Since the stochastic process defines the number of total iterations, the resource usage is small relative to fitting. In addition, the method is less susceptible to errors due a ill chosen adding threshold. Other methods will produce un-normalized florescence curves if the adding threshold is too small. Due to these reasons, the stochastic method is the only process suitable for any three-photon dissociation experiments.

Comparing all four methods based on peak behavior at different regimes and resource usage, the expected rate of dissociation is the most viable solution for two-photon dissociation. On the other hand, the stochastic method is ideal for three-photon dissociation.

2.3 Simple Model

While the full-simulation model is more accurate, the simple model is more efficient and needs less computational resources. The efficiency enables optimizations and non-linear regression with experimental data. While the simple model cannot account for competing reactions and multiple intra-electronic transitions, the optimizations provide an initial guess for corrections to the CaH^+ PES curves. In addition to the assumptions for the full simulation model, the simple model assumes the dissociation process is always a two-photon procedure: one photon from the ground state to an intermediate state and a second photon from the intermediate state to the dissociative state. There are two versions of the simple model, and the second version assumes the dissociation rate is always faster than the excitation transition rate. Further sections discuss whether this assumptions is

reasonable or not.

2.3.1 Simple Model Derivation

The simple model is derived from a simple three state problem where the states are the ground state (N_0), an intermediate transition state (N_1), and the dissociative state (N_2). This is the assumptions that prevents intra-electronic transitions.

$$\frac{dN_0}{dt} = -\Gamma_{01}N_0 - \Gamma_{02}N_0 + \Gamma_{10}N_1 \tag{2.30}$$

$$\frac{dN_1}{dt} = \Gamma_{01}N_0 - \Gamma_{10}N_1 - \Gamma_{12}N_1 \tag{2.31}$$

$$\frac{dN_2}{dt} = \Gamma_{02}N_0 + \Gamma_{12}N_1 \tag{2.32}$$

These rates are converted to a transition matrix form as before.

$$\begin{bmatrix} -\Gamma_{01} - \Gamma_{02} & \Gamma_{10} & 0 \\ \Gamma_{01} & -\Gamma_{10} - \Gamma_{12} & 0 \\ \Gamma_{02} & +\Gamma_{12} & 0 \end{bmatrix} \begin{bmatrix} N_0 \\ N_1 \\ N_2 \end{bmatrix} = \begin{bmatrix} \frac{dN_0}{dt} \\ \frac{dN_1}{dt} \\ \frac{dN_2}{dt} \end{bmatrix} \tag{2.33}$$

To simplify the matrix for computation, two additional assumptions are applied. Since the laser rate is greatly larger than the BBR rate rate, the forward and backwards rates are approximately the same, $\Gamma_{01} \cong \Gamma_{10}$. The second assumptions expects the ground state to not dissociate, $\Gamma_{02} \cong 0$. This is the assumption that prevents competing reactions. The full derivation, without these two assumptions is included in the appendix.

$$\begin{bmatrix} -\Gamma_{01} & \Gamma_{01} & 0 \\ \Gamma_{01} & -\Gamma_{01} - \Gamma_{12} & 0 \\ 0 & +\Gamma_{12} & 0 \end{bmatrix} \begin{bmatrix} N_0 \\ N_1 \\ N_2 \end{bmatrix} = \begin{bmatrix} \frac{dN_0}{dt} \\ \frac{dN_1}{dt} \\ \frac{dN_2}{dt} \end{bmatrix} \tag{2.34}$$

Solving the matrix ODE requires the eigenvalues (λ_0, λ_1, λ_2) and eigenvectors (v_0, v_1,

v_2).

$$\lambda_0 = 0$$

$$\lambda_1 = \frac{1}{2}\left(-\sqrt{4\Gamma_{01}^2 + \Gamma_{12}^2} - 2\Gamma_{01} - \Gamma_{12}\right)$$

$$\lambda_2 = \frac{1}{2}\left(\sqrt{4\Gamma_{01}^2 + \Gamma_{12}^2} - 2\Gamma_{01} - \Gamma_{12}\right)$$

$$
\begin{bmatrix} v_0 \\ v_1 \\ v_2 \end{bmatrix} =
\begin{bmatrix}
0 & \frac{-1}{2\Gamma_{12}}\left(\lambda_1 + 3\Gamma_{12}\right) & \frac{-1}{2\Gamma_{12}}\left(\lambda_2 + 4\Gamma_{01} + 3\Gamma_{12}\right) \\
0 & \frac{-1}{2\Gamma_{12}}\left(\lambda_2 + 3\Gamma_{12}\right) & \frac{-1}{2\Gamma_{12}}\left(\lambda_1 + 4\Gamma_{01} + 3\Gamma_{12}\right) \\
1 & 1 & 1
\end{bmatrix}
\tag{2.35}
$$

The SVU decomposition directly solves the matrix ODE problem:

$$
\begin{bmatrix}
0 & \frac{-1}{2\Gamma_{12}}\left(\lambda_1 + 3\Gamma_{12}\right) & \frac{-1}{2\Gamma_{12}}\left(\lambda_2 + 4\Gamma_{01} + 3\Gamma_{12}\right) \\
0 & \frac{-1}{2\Gamma_{12}}\left(\lambda_2 + 3\Gamma_{12}\right) & \frac{-1}{2\Gamma_{12}}\left(\lambda_1 + 4\Gamma_{01} + 3\Gamma_{12}\right) \\
1 & 1 & 1
\end{bmatrix}
\begin{bmatrix} z_0 \\ z_1 \exp(\lambda_1 t) \\ z_2 \exp(\lambda_2 t) \end{bmatrix} =
\begin{bmatrix} N_0(t) \\ N_1(t) \\ N_2(t) \end{bmatrix}
\tag{2.36}
$$

Since the molecule population is assumed to start in the ground state at time zero and end up in the dissociative state at time infinity, boundary conditions determine the initial constants, (z_0, z_1, z_2).

T = 0:

$$
\begin{bmatrix}
0 & \frac{-1}{2\Gamma_{12}}\left(\lambda_1 + 3\Gamma_{12}\right) & \frac{-1}{2\Gamma_{12}}\left(\lambda_2 + 4\Gamma_{01} + 3\Gamma_{12}\right) \\
0 & \frac{-1}{2\Gamma_{12}}\left(\lambda_2 + 3\Gamma_{12}\right) & \frac{-1}{2\Gamma_{12}}\left(\lambda_1 + 4\Gamma_{01} + 3\Gamma_{12}\right) \\
1 & 1 & 1
\end{bmatrix}
\begin{bmatrix} z_0 \\ z_1 \\ z_2 \end{bmatrix} =
\begin{bmatrix} 1 \\ 0 \\ 0 \end{bmatrix}
\tag{2.37}
$$

T = ∞:

$$\begin{bmatrix} 0 & \frac{-1}{2\Gamma_{12}}(\lambda_1 + 3\Gamma_{12}) & \frac{-1}{2\Gamma_{12}}(\lambda_2 + 4\Gamma_{01} + 3\Gamma_{12}) \\ 0 & \frac{-1}{2\Gamma_{12}}(\lambda_2 + 3\Gamma_{12}) & \frac{-1}{2\Gamma_{12}}(\lambda_1 + 4\Gamma_{01} + 3\Gamma_{12}) \\ 1 & 1 & 1 \end{bmatrix} \begin{bmatrix} z_0 \\ 0 \\ 0 \end{bmatrix} = \begin{bmatrix} 0 \\ 0 \\ 1 \end{bmatrix} \quad (2.38)$$

Solving the boundary conditions gives:

$$\begin{bmatrix} z_0 \\ z_1 \\ z_2 \end{bmatrix} = \begin{bmatrix} 1 \\ \frac{-\sqrt{4\Gamma_{01}^2 + \Gamma_{12}^2} + 2\Gamma_{01} + B}{2\sqrt{4\Gamma_{01}^2 + \Gamma_{12}^2}} \\ \frac{-\sqrt{4\Gamma_{01}^2 + \Gamma_{12}^2} - 2\Gamma_{01} - B}{2\sqrt{4\Gamma_{01}^2 + \Gamma_{12}^2}} \end{bmatrix} \quad (2.39)$$

The dissociation population over time appears immediately:

$$N_2(t) = 1 + \frac{-\sqrt{4\Gamma_{01}^2 + \Gamma_{12}^2} + 2\Gamma_{01} + B}{2\sqrt{4\Gamma_{01}^2 + \Gamma_{12}^2}}\exp(\lambda_1 t) + \frac{-\sqrt{4\Gamma_{01}^2 + \Gamma_{12}^2} - 2\Gamma_{01} - B}{2\sqrt{4\Gamma_{01}^2 + \Gamma_{12}^2}}\exp(\lambda_2 t)$$

$$(2.40)$$

As with full-simulations, this rate must imitate an exponential decay rate, $N_2(t) = 1 - \exp(-\Gamma t)$, to match the experimental approximation. Using numerical analysis, Γ appears to be approximately $-\lambda_2$:

$$N_2(t) = 1 - \exp(\lambda_2 t). \quad (2.41)$$

To produce the second version of the simple model, the model factors in the assumption $\Gamma_{12} >> \Gamma_{01}$ assumption, which simplifies the rate to:

$$N_2(t) = 1 - \exp(-\Gamma_{01} t). \quad (2.42)$$

Therefore the estimated dissociation rate without any dissociation dependence is Γ_{01}. **Figure 2.6** demonstrates a shift in the peak between the two simple models. The model which assumes instantaneous dissociation, **Equation 2.42** is blue shifted compared to the

model without instantaneous dissociation, **Equation 2.41**. This shift comes from the blue shifted dissociation cross section, which does not meet the $\Gamma_{12} >> \Gamma_{01}$ criteria.
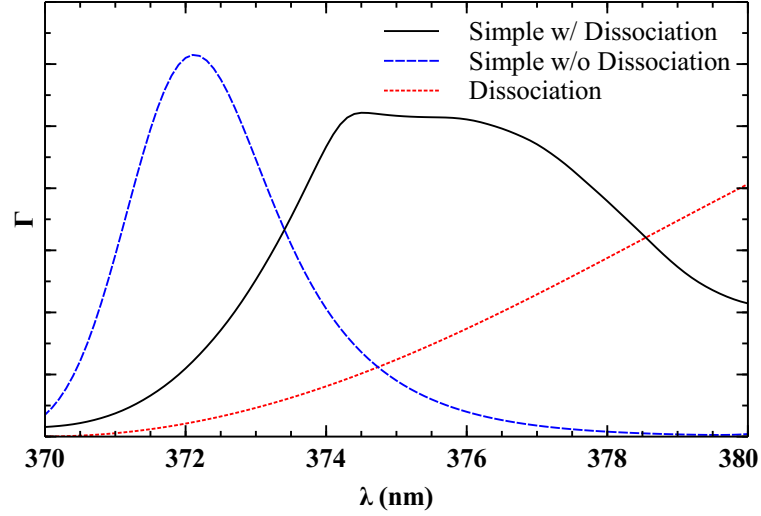
Figure 2.6: The shape of a peak and the center of the peak changes based on the method used to determine the rate. The peak using **Equation 2.41** is a convolution of the peak from **Equation 2.42** and the dissociation cross section. This graph shows the CaH$^+$ $^1\Sigma(v = 0) \rightarrow^2 \Sigma(v' = 3)$ REMPD peak from the simple model. I_0 = 1e16 W/m^2, σ = 1.1074 nm.

2.3.2 Simple Rate Calculations

The simple model requires estimations for the overall transition and dissociation rate, Γ_{01} and Γ_{12} respectively. Summing the individual transitions rates corresponding to initial ground state population gives a good estimate of the transition rate [121, 123, 125, 126, 134]:

$$\Gamma(\lambda) = \frac{1}{\tau_{sp}} = \sum_{J,v',J'=\pm J} \Gamma_{n',v',J'\leftarrow n,v,J}(\nu_{n',v',J'\leftarrow n,v,J})N(n,v,J). \qquad (2.43)$$

This same concept is applied to find an overall dissociation rate which is a weighted sum of the eigenvalue, λ_2, for all possible dissociation pathways [121, 123, 125, 126, 134]:

$$\Gamma(\lambda) = \sum_{J,v',J'=\pm J} \lambda_2(\infty \leftarrow n',v',J' \leftarrow n,v,J)N(n,v,J). \qquad (2.44)$$

2.3.3   Optimizations

The simple model is designed for optimizations, especially non-linear regressions. All constants are initial set to theoretical values from literature and *ab initio* calculations. The Nelder-Mead Minimization Algorithm minimizes an error function, E, between experiments and theory values. The error function depends on a summation of the dissociation rates from theory, Γ^T, experiment, Γ^E, and the error from experiments, σ^E. The simulation implements various E functions depending on the availability of σ^E and the needs of the optimization:

$$
\begin{aligned}
E &= \sqrt{\sum_i \frac{(\Gamma_i^T - \Gamma_i^E)^2}{\sigma_i^{E2}}} & (2.45) \\
&= \sqrt{\sum_i \frac{(\Gamma_i^T - \Gamma_i^E)^2}{\Gamma_i^E}} & (2.46) \\
&= \sqrt{\sum_i (\Gamma_i^T - \Gamma_i^E)^2} & (2.47) \\
&= \sqrt{\sum_i 1 \exp\left(\frac{(\Gamma_i^T - \Gamma_i^E)^2}{2\sigma_i^{E2}}\right)} & (2.48) \\
& & (2.49)
\end{aligned}
$$

The program implements this regression using a C++ library [135]. Typically the optimized parameters are laser linewidth, vibronic zero-point energy, rotational constants, and transition dipoles.

Each optimized parameter has a variance to measure the precision, which comes from the covariance matrix. The covariance matrix is related to a Hessian matrix:

$$
\sigma^2 = \frac{1}{-\mathbb{H}}, \qquad (2.50)
$$

where

$$
H_{ij} = \frac{\partial^2 E}{\partial i \partial j}, \qquad (2.51)
$$

where i and j are parameters being optimized. Since many Hessians do not have inverses, the program assumes that all off-diagonal elements are zero, which implies no correlation between parameters. This simplifies the standard deviation to:

$$\sigma_i = \sqrt{-\frac{\partial^2 E}{\partial i^2}^{-1}}. \qquad (2.52)$$

2.4 Hamiltonian Model

The Hamiltonian method uses a general Hamiltonian operator, $\hat{\mathcal{H}}$, to calculate transition in a molecule. While this operator includes the kinetic and potential energy for the system, only the potential will affect the transition rate:

$$\hat{\mathcal{H}}' = -\hat{\vec{\mu}} \cdot \vec{E}(t). \qquad (2.53)$$

Detailed descriptions of the electric dipole moment, $\hat{\vec{\mu}}$, and the electrostatic field, $\vec{E}$, are included below. This method assumes all rotations are classical and the excitation laser is a Gaussian profile. The Hamiltonian method is potentially more accurate than methods since it makes less assumptions to calculate individual transition rates. However, this method does not account for the full REMPD process, nor completing transitions in its current form. When applied to a wide laser, this model imitates the simple model. Later studies prove theoretical PES curves incorrect for CaH^+, therefore this model was never fully developed.

The electric dipole moment for a molecule measures the overlap between an initial state, E, to a final state, E', to determine the strength of a transition:

$$\hat{\vec{\mu}} = \langle E' | \, e\vec{r} \, | E \rangle. \qquad (2.54)$$

The dipole depends on the elementary charge, e, and the dipole operator, $\vec{r}$. The

electrostatic field describes the strength of the laser at the transition's frequency:

$$E\vec{(t)} = \vec{E_0} \exp(i2\pi c\nu\vec{r}) \exp(-ic\nu t), \qquad (2.55)$$

where

$$\vec{E_0} = \sqrt{\frac{2I_0}{c\varepsilon_0}}. \qquad (2.56)$$

The field propagates through time, t.

Fermi's Golden rule characterizes the overall transition rate within a continuum:

$$\Gamma_{E' \leftarrow E} = \frac{2\pi}{\hbar} \left| \langle E' | \hat{\mathcal{H}}' | E \rangle \right|^2 \rho(\nu). \qquad (2.57)$$

This is the probability of transition per unit time. To account for a wide laser, this rate should be convoluted with the laser profile based on frequency. However, these transitions exist at discrete wavelengths and do not have a continuous function to describe all of the transition frequencies. This means a wide laser must apply **Equation 2.43** to account for exciting multiple transitions:

$$\Gamma = \sum_\nu \Gamma_{E' \leftarrow E} = \sum_\nu \frac{2\pi}{\hbar} \left| \langle E' | \hat{\mathcal{H}}' | E \rangle \right|^2 \rho(\nu) N_\nu. \qquad (2.58)$$

Applying general simplifications to this system gives a similar result to the stimulated laser transition rate:

$$\Gamma = \sum_\nu \Gamma_{E' \leftarrow E} = \sum_\nu \frac{\pi e^2 E_0^2}{2\hbar^2} |\langle E' | \vec{r} | E \rangle|^2 \frac{g(\nu)}{c\nu} N_\nu. \qquad (2.59)$$

2.5 Peak Properties

Various factors could affect the properties of each peak in a spectrum, where the main properties defining each peaks are height, width, and location. This next section describes

which physical inputs will affect which peak properties. The physical inputs consist of either physical constants unique to the molecule, or experimental constants unique to the set-up. Comparing these attributes determines which constants are optimizable for matching theory simulations to experimental spectra. To increase efficiency, the optimization ignores factors that cannot be accounted for by the model. Well-known parameters, such as those which have been experimentally measured, are held constant. All other factors are eligible for optimizations.

2.5.1 Peak Width

The peak width and overall peak shape depend on how the laser interacts with a map of transitions. With a broad frequency distribution, the laser will excite/dissociate multiple rovibronic transitions. If the laser variance changes, the number of excited transitions will change, which affects the overall peak width. If the underlying transition map changes, then the peak will change width and sometimes shape. The model accounts for the underlying transition distribution internally, but the rotational constants and laser linewidth are optimizable constants, **Figure 2.7**. With a narrow frequency distribution, the laser is irrelevant and line broadening is the main factor affecting peak width. Common types of broadening are on-resonance multi-photon transition/dissociation, Doppler broadening, and the natural line width. As stated previously, multi-photon rates are ignored for simplicity. Doppler broadening does not occur in our CaH^+ experiments, due to the cooling process. The natural linewidth is small in trapped-cooled CaH^+, therefore, the model does not try to account for it. Since experiments in this dissertation use broad laser, line broadening has no visible affect on experimental spectra.
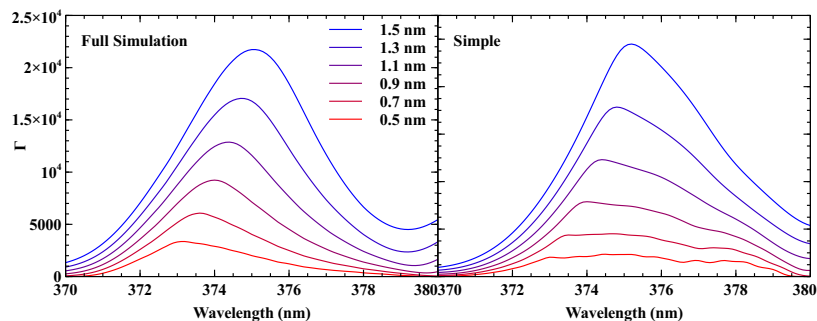
Figure 2.7: The height of a peak changes based on the laser σ. This graph shows the CaH^+ $^1\Sigma(v=0) \rightarrow ^2\Sigma(v'=3)$ REMPD peak from the full-simulation model, **Section 2.2**, and the simple model, **Equation 2.41**. I_0 = 1e14 W/m^2, t_{max} = 4.0e-3 s.

2.5.2   Relative Peak Height

Optimizable parameters affect the absolute and relative peak height differently. Experiments involving CaH^+ cannot guarantee a absolute dissociation rate, only a relative rate. In addition, the simple model can only match relative rates. Therefore the optimizations account for relative factors, mainly. The relative transition dipole moment is the strongest constant for relative transition strength, therefore the model concentrates on optimizing this constant. The intensity of the laser is constant over the entire tunable range, and therefore, only changes the absolute height of peaks, not the relative height. For REMPD experiments, the average dissociation rate proportionate to the average transition rate will change the relative peak height. The model optimizes the location of the PES curve, which will in turn optimize the dissociation rate. The total experiment time, t_{max}, determines which portion of the florescence curve the model takes into account. While CaH^+ experiments have a predefined time, shorter times will change the absolute peak height, **Figure 2.8**. The last factor considered is the cross-excitation affect from neighboring molecules and atoms. As CaH^+ and Ca^+ undergoes internal conversion and relaxation, the emitted photons could excite neighboring CaH^+ molecules, which would change the absolute and relative rates. As the model assumes a single molecule set-up, this is currently unaccounted for, but could be included using molecular dynamic

38
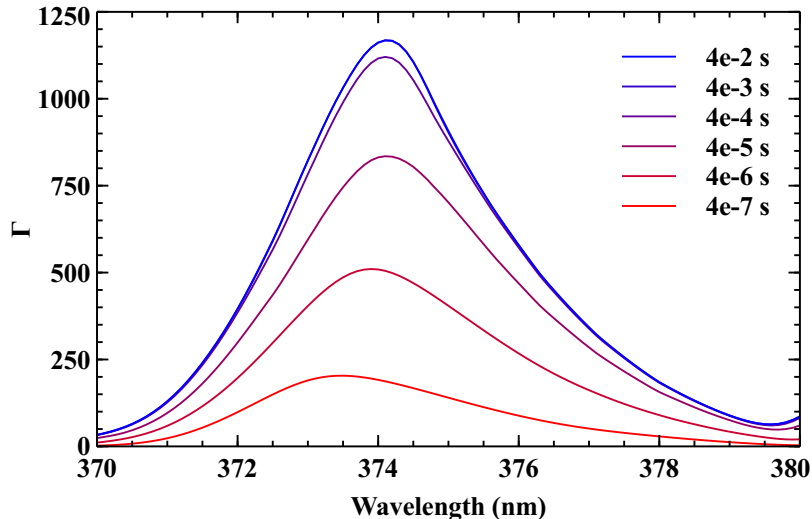
simulations.

Figure 2.8: The height of a peak changes based on how long the experiment was. This graph shows the CaH$^+$ $^1\Sigma(v = 0) \rightarrow ^2\Sigma(v' = 3)$ REMPD peak from the full-simulation model, **Section 2.2**. The simple model does not depend on time. I_0 = 1e13 W/m^2, σ = 1.1074 nm.

2.5.3   Peak Location

The location/maximum of a peak, which is not equivalent to the transition frequency, hinges on how various transition frequencies shifts due experimental conditions. While the transition frequency is the main optimizable constant, it is not the only possible one. The underlying rovibronic transition map can shift the peak in one direction. The model predicts this shift, but optimizing the rotational constants changes the exact vibronic peak location. Line splitting such as Zeeman splitting, Stark splitting, Hyperfine splitting, and off-resonance multi-photon transitions/dissociation may also affect the underlying transitions. As discussed previously, the model ignores all multi-photon affects and assumes all other affects are negligible.

2.6   Experimental Laser Profile

Table 2.1: Experimental Constants for Dissociation/Transition Laser

Constant	Value
Average Power	20 mW
Pulse Width (FWHM)	185 fs
Repetition Rate	76 MHz
Beam Diameter	20 μm
σ^2	1.11 nm
σ^2 at 397 nm	70263.3 m^{-1}
σ^2 at 794 nm	17565.8 m^{-1}
$\frac{1}{e^2}$	4.21E-6 mm
I_0	2.0e20 W/m^2
Peak Power	1336 W

CHAPTER 3

CAH$^+$ VIBRONIC TRANSITIONS

Co-trapping molecular ions with Doppler-cooled atomic ions sympathetically cools the molecular motion to millikelvin temperatures, enabling studies in spectroscopy and reaction dynamics [11, 20, 38, 80, 86]. Cold ionic ensembles in a variety of platforms have proved useful for astrochemical identification [21, 65, 66] and studies of internal state distributions,[38, 98] while co-trapping with Doppler-cooled ions offers advantages for probing the possible time variation of fundamental constants, [30, 31, 33, 136] and performing quantum logic spectroscopy. [35, 63, 78, 104] Ionic metal-hydrides like CaH+ and MgH+ are promising candidates for these applications [89] due to their large rotational constants and Doppler-cooled dissociation products.

To date, spectroscopy on CaH$^+$ is limited to two vibrational overtones [137], four vibrational levels within the $2^1\Sigma$ state [108], a photodissociative electronic transition [46], and single-ion quantum logic probes of rotational state [35]. The vibronic transitions of Ref. [108] were previously assigned according to theory. The observed transition frequencies agreed to within 50 cm^{-1} of theory, but the $v = 0 \to v' = 0$ transition was not observed. A similar issue was encountered for the isoelectronic KH neutral, where the first few vibronic lines were experimentally absent and KD spectroscopy was required in order to correctly assign the KH transitions [138–141]. Isotopic substitution changes the reduced mass but maintains the adiabatic electronic potential energy. The resulting shift in vibrational energy levels can be compared to theory to confirm peak assignments.

Here we apply this method to the spectroscopy of CaH$^+$ and CaD$^+$. Vibronic transitions were calculated using a MS-CASPT2 internuclear potential [2] and then compared to measured transition frequencies obtained by resonance enhanced multiphoton photodissociation spectroscopy (REMPD). Instead of observing the predicted

shifts for deuterium substitution based on our previous assignment, this study reveals a 687 cm^{-1} disagreement in the electronic energy from MS-CASPT2 and leads to a revised labeling of the CaH^+ and CaD^+ vibronic transitions.

3.1   Methods
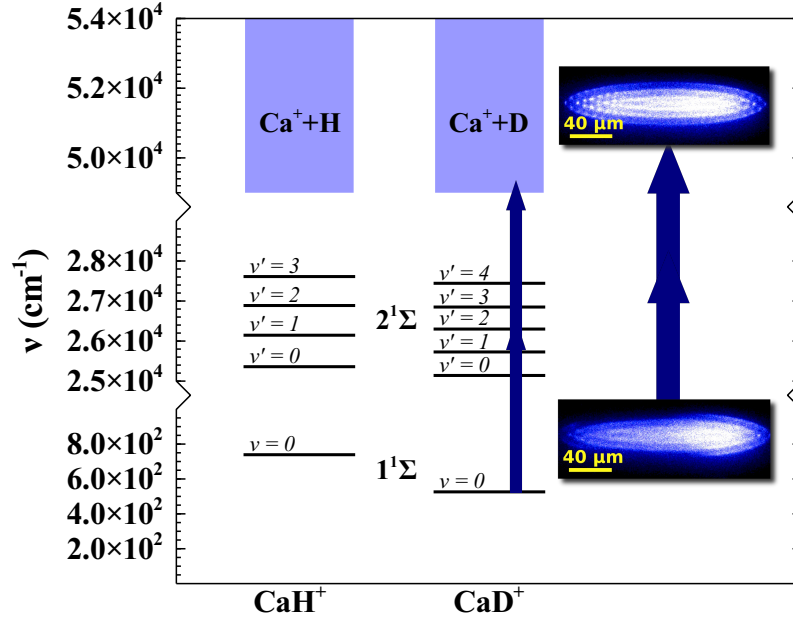
Figure 3.1: Energy level diagram of the CaH^+ and CaD^+ transitions probed by applying a doubled Ti:Sapphire laser and observing resonance enhanced photodissociation. The photodissociation of dark CaD^+ ions in the crystal into trapped Ca^+ and free H can be observed in the crystal image and by an increase in 397 nm Ca^+ fluorescence signal.

The experiment employed a manually-tuned, frequency-doubled Ti:Sapphire laser to probe the vibronic transitions of CaD^+ co-trapped with laser-cooled Ca^+ in a heterogeneous Coulomb crystal. By measuring the Ca^+ fluorescence increase upon laser exposure, a spectrum of molecular dissociation rate was generated. The experiments take place in an ultrahigh vacuum chamber with a background pressure of 10^{-10} torr and the ions are held in a linear Paul trap. CaD^+ is generated by reaction of D_2 with excited Ca^+ at pressures of 10^{-8} torr. The Ca^+ is observed and laser cooled by the laser-induced fluorescence at 397 nm. A repump laser at 866 nm is also required to close the transition.

Details of the experimental setup may be found in our previous work [108] on the vibronic spectroscopy of CaH^+.

The MS-CASPT2 potential energy surface of CaH^+ guided our spectroscopic search for CaD^+ vibronic transitions [2]. To achieve the desired 24390 to 27100 cm^{-1} range, the mode-locked Ti:Sapphire laser was frequency-doubled by a BBO crystal before being sent along the trap axis. Each fluorescence measurement was taken for 8 ms after ten sets of alternating 200 μs delay and 200 μs exposure to the AOM-shuttered 20 mW Ti:Sapph beam. A fit of the fluorescence intensity to the total exposure time t to the exponential equation:

$$A_t = A_\infty - (A_\infty - A_0)e^{-\Gamma(\lambda)t}, \tag{3.1}$$

yields the dissociation rate Γ as a function of wavelength λ. A_∞ and A_0 are the steady-state and initial fluorescence counts, respectively. Scans exhibiting first-order CaD^+ dissociation are presented in **Figure 3.2**. Dissociation rate plotted as a function of frequency yielded the spectrum in **Figure 3.3**. [1]

---

[1]The CaH^+ peaks were taken with ten sets of alternating 400 μs delay and 400 μs exposure time. Ref. [108] peak heights and rates differ by a factor of 10 because an internal counter in the computer control of the experiment was overlooked in the analysis.
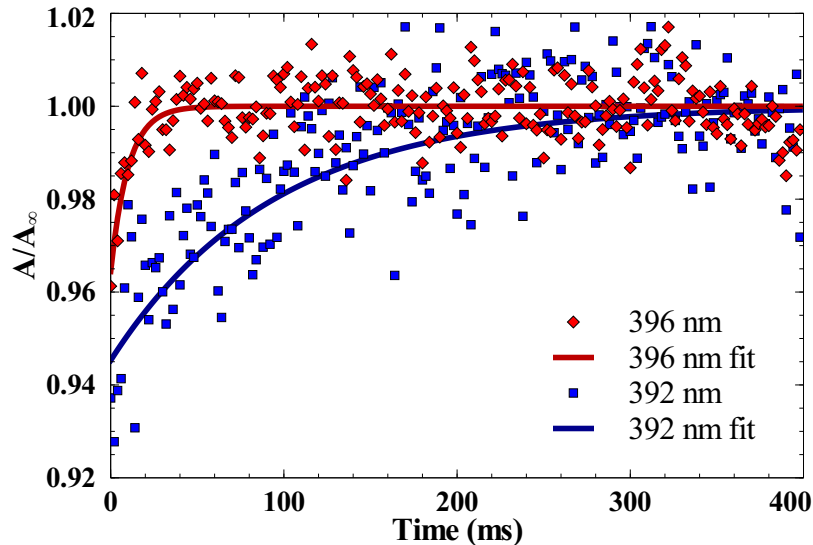
Figure 3.2: Observed Ca^+ fluorescence of composite Coulomb crystals exposed to two laser frequencies. An increase in fluorescence indicates resonance-enhanced dissociation of CaD^+ into Ca^+ and D. Dissociation rates extracted from **Equation 3.1** are plotted against frequency in **Figure 3.3**.
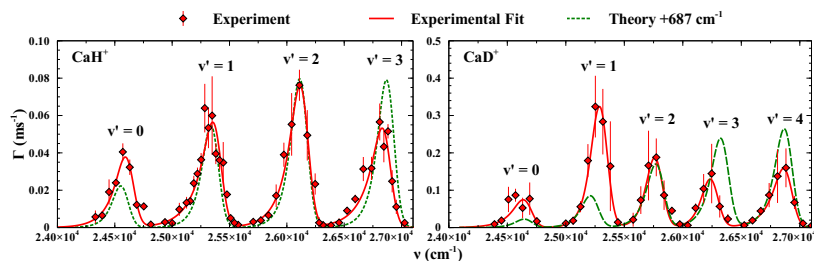
Figure 3.3: Comparisons of the experimental and *ab initio*-predicted spectra for each isotopologue. The optimized parameters include $G_1(v')$, $B_{1,v'}$, and $\mu_{v \to v'}$. Relative heights of theoretical vibronic peaks are governed by MS-CASPT2 transition dipole moments scaled to fit the experimental $v' = 2$ peak, while peak shapes come from the Boltzmann rotational state distribution 298 K.

3.1.1   Theoretical Model for Parameter Estimation

To compare theory and experiment, CaD^+ dissociation spectra were modeled using theoretical and experimental parameters. Calculation of the Einstein A for each transition gave a dissociation rate, and the total rate at each wavelength was obtained by summing all transitions covered by the laser linewidth [108]. Although the experimental CaD^+

dissociation is a multi-photon process, we used a first-order model by assuming the dissociation rate is much greater than the first excitation rate.

The spectra labeled "Theory" in **Figure 3.3** rely heavily on MS-CASPT2 *ab initio* calculations: the potential energy surfaces, transition dipole moments $\mu_{v \to v'}$, and vibronic transition frequencies $G_{0 \to 1}(v')$ come from Ref. [2]. Harmonic, ω_1, and anharmonic, $\omega \chi_1$, constants were generated using the internuclear potential curves and R.J. LeRoy's open-source project, LEVEL [115]. Relative peak heights were determined by assuming a thermal distribution of the rotational states in $1^1 \Sigma$. The first 15 *J* rotational levels contribute >99.99% of the initial state population and dominate the shapes of the vibronic peaks.

During spectral simulation, the spectral density of the laser was held at a constant linewidth of 80 cm^{-1} to match the laser linewidth based on spectrometer measurements. The model's invariant peak intensity of 4.77×10^8 W/m^2 was calculated from the laser power and beam waist diameter at the trap center. The *ab initio* calculated energy of the $1^1 \Sigma$ ground vibrational state was used as a reference for all transitions due to lack of experimental data on the ground state potential.

3.2 Results and Discussion

Table 3.1: Comparison of MS-CASPT2 [2] and CCSDT/cc-pCV5Z theoretical prediction for vibronic transition frequencies for CaH^+ and CaD^+. Below, experimental transitions frequencies are determined by fitting a convolution of laser linewidth and parameter-dependent level structure to laser-induced dissociation rates of CaH^+ and CaD^+. The previous CaH^+ is shifted -50 cm^{-1} from MS-CASPT2 calculations [108] while the revised CaH^+ is shifted +687 cm^{-1}. The resulting fit is compared to an *ab-initio* spectrum in **Figure 3.3**
.

v'	CaH^+ CASPT2	CaH^+ CCSDT	CaD^+ CASPT2	CaD^+ CCSDT
0	23887	24302.0	23983	24404.4
1	24674	25066.4	24666	24953.3
2	25449	25823.2	25305	25498.4
3	26206	26572.4	25845	26039.7
4	26942	27314.0	26199	26577.2

v'	Previous CaH^+	Revised CaH^+	CaD^+
0	(unobserved)	24635 ± 49	24683 ± 128
1	24635 ± 74	25401 ± 21	25321 ± 22
2	25401 ± 31	26158 ± 18	25792 ± 49
3	26158 ± 27	26879 ± 29	26268 ± 60
4	26879 ± 35	-	26908 ± 55

Figure 3.3 compares the REMPD spectra of CaH^+ and CaD^+ produced from **Equation 2.43**. As expected, the CaD^+ transition frequencies were more tightly-packed, owing to the decrease in ω_e accompanying the increase in reduced mass. Complication arose when matching the *ab initio* predictions to experimental values: the theory, shifted by -50 cm^{-1} to agree with CaH^+, systematically underestimated the CaD^+ vibronic transition frequencies by >100 cm^{-1}. If the assignments proposed in Ref. [108] were correct, this study would

imply a 150 cm^{-1} isotopic shift of the electronic energy potential and further evidence the experimentally unobserved transition to the $v' = 0$ state. The isotopic shift of the electronic energy level is large compared to the 10 cm^{-1} shifts seen in KH [139, 141]. These spectral anomalies prompted a reassignment of the vibrational energy levels within the $2^1\Sigma$ manifold.

The new assignment of vibrational quantum numbers, shown in **Table 3.1**, reflects a 687 cm^{-1} departure from *ab initio* calculations. This shift manifests as a 687 cm^{-1} increase in $T(1) - E_0$. Roughly a vibrational quantum in CaH$^+$, the revision is greater than the 100 - 150 cm^{-1} error window afforded by the mismatch of calculated and measured dissociation asymptotes for Ca$^+(3d^1)$ and H$(1s^1)$. This revised assignment, however, features observable vibrational peaks through $v' = 4$ and good agreement for both isotopologues.

3.2.1 Experimental Parameters

With the new CaH$^+$ and CaD$^+$ peak assignments, we determined the spectroscopic constants of the excited state by fitting both theory and experimental values to a second-order model of vibrational energy levels. Vibronic transitions to v' of the $2^1\Sigma$ state were modeled with the equation

$$v_{v'} = T(1) + \omega_1(v' + \frac{1}{2}) - \omega\chi_1(v' + \frac{1}{2})^2 - E_0, \qquad (3.2)$$

where $T(1)$ is the potential minimum of the $2^1\Sigma$ state, and E_0 is the zero-point energy of the ground state. The parameters $T(1)$, ω_1, and $\omega\chi_1$ for both CaH$^+$ and CaD$^+$ are varied to fit experimental data points by quadratic regression. Regression curves of theory predictions and experimental fits were plotted (see **Figure 3.4**) to obtain the constants listed in **Table 3.1**. Since CaH$^+$ ground state information is limited [137], the E_0 energy is confined to the *ab initio* prediction. The fitted MS-CASPT2/experimental constants only use a second order fit, while the theoretical MS-CASPT2/CCSDT constants use higher

order terms, which accounts for the change in the ω_1 value.

Table 3.2: Molecular constants for the $1^1\Sigma \to 2^1\Sigma$ vibronic transitions of CaH^+ and CaD^+ based on the revised peak assignments are shown. Constants are obtained from fitting the transition energies as in Ref. [108]. (see **Table A.1** for the complete list of parameters calculated by the new (EOM)-CCSDT/cc-pCV5Z). All values are in cm^{-1}.

	ω_1	$\omega\chi_1$	T(1) - E_0	E_0
CaH^+ Experimental	813 ± 6	16.8 ± 1.4	24239 ± 5	-
CaH^+ CASPT2	773	-	23488	739
CaH^+ CASPT2 Fitted	803 ± 3	7.5 ± 0.7	23487 ± 2	739
CaH^+ CCSDT	772	3.8	23907	749
CaD^+ Experimental	521 ± 72	1.0 ± 14.0	24506 ± 76	-
CaD^+ CASPT2 Fitted	574 ± 1	3.5 ± 0.1	23697 ± 1	526
CaD^+ CCSDT	553	1.9	24123	537

The spectroscopic constants agree reasonably with theory, however we notice a large shift of the excited state potential. To maintain the assumption that the internuclear potentials of CaH^+ and CaD^+ are similar, the energy surfaces of the MS-CASPT2 *ab initio*-calculated $1^1\Sigma$ and $2^1\Sigma$ states must be separated by an additional 687 cm^{-1}.
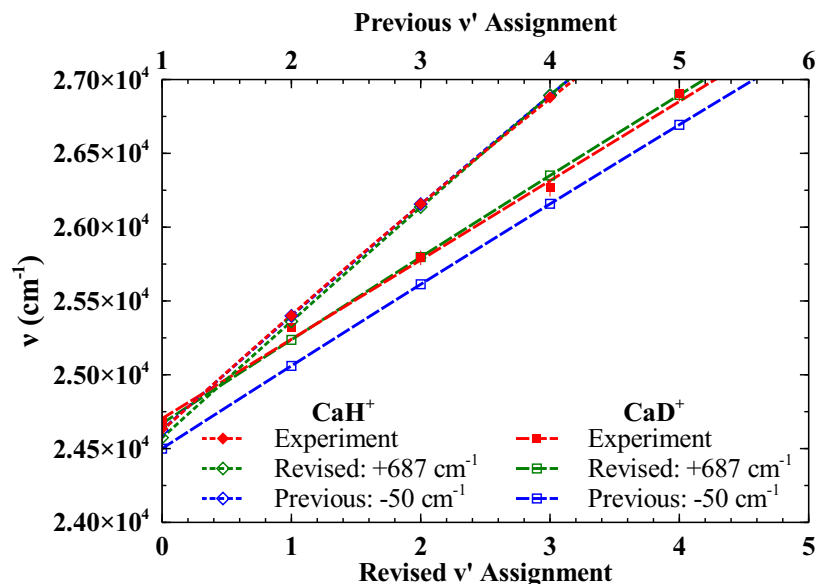
Figure 3.4: The vibronic transitions of CaH^+ and CaD^+ and their associated fits using **Equation 3.2**. Theoretical and experimental values are separated by 687 cm^{-1} on average. Spectroscopic constants of each species may be found in **Table 3.1**.

This sizable departure from *ab initio* calculations is currently unexplained. Deviations could be due to the frozen core electron approximation of MS-CASPT2 or non-adiabatic effects. The latter effect is expected to be small based on estimations from other diatomic hydrides. LiH vibrational levels show a 10 cm^{-1} isotopic electronic shift[142, 143] and the KH, KD system features corrections around 10 cm^{-1} [139, 141]. The disparity in experimental and calculated peak heights may be explained after further study of electronic levels relevant to the dissociation pathway. In addition, the different rates for CaH^+ and CaD^+ dissociation may be due to an enhanced forward reaction rate for $Ca^+ + H_2$ due to the kinetic isotope effect depressing the observed dissociation rate.

In our computations, the 102 cm^{-1} uncertainty in ω_1 absorbs the CaD^+ $\omega\chi_1$ constant. The deviations in peak position and relative peak heights from our simple model may be due to an unknown dissociation pathway and is a topic of future research. In particular, the shape of the v'=0 peak was not well matched by our simple model leading to a large uncertainty in its calculated position.

3.2.2 Revised Theoretical Predictions

The deviation from the initial *ab initio* calculations could be due to the frozen core electron approximation of MS-CASPT2 or non-adiabatic effects. The latter effect is expected to be small based on estimations from other diatomic hydrides. LiH vibrational levels [142, 143] and the KH, KD system [139, 141] feature corrections around 10 cm^{-1}. To address the former, new computational results for the ground $1^1\Sigma$ state were obtained using coupled-cluster theory using single and double substitutions (CCSD),[144] coupled-cluster through full triple substitutions (CCSDT),[145–147] or coupled-cluster through full quadruple substitutions (CCSDTQ) [148, 149]. Although CaH$^+$ is nominally a two-valence-electron system, where a model like CCSD should be quite accurate, group II elements like Ca atom tend to have modest core-valence energy gaps, and so we also included the Ca $3s$ and $3p$ electrons in the coupled-cluster procedure. To describe the core-valence correlation, we employed the correlation-consistent polarized core-valence (cc-pCVXZ) basis sets,[150, 151] using cardinal numbers X = D (double-ζ) through 5 (pentuple-ζ). The $2\,^1\Sigma$ excited state was obtained using equation-of-motion (EOM) coupled-cluster techniques,[152] and their extension to full triple (EOM-CCSDT)[153] and quadruple substitutions (EOM-CCSDTQ) [154].

These single-reference coupled-cluster methods should be appropriate for accurate computations of the equilibrium geometries of the $1^1\Sigma$ and $2^1\Sigma$ states, even though the equilibrium bond length of the excited state is somewhat stretched compared to that in the ground state. Any small deficiencies due to incipient multi-reference character at these bond lenghts should be effectively dealt with by the time one adds triple substitutions through (EOM)-CCSDT. Indeed, as shown in the Appendix for the cc-pCVDZ basis set, (EOM)-CCSDT appears to be essentially converged with respect to electron correlation treatment, because the (EOM)-CCSDTQ results hardly differ. There are, however, substantial differences between (EOM)-CCSD and (EOM)-CCSDT at larger internuclear separations due to the decreasing energy gap between the σ^2 and $(\sigma^*)^2$ configurations.

50

Because (EOM)-CCSDT remains computationally feasible for larger basis sets [unlike (EOM)-CCSDTQ], we have utilized it as our primary theoretical method for this study. As shown in the Appendix, (EOM)-CCSD potential curves appear to be converging with respect to basis set by the time one uses cc-pCV5Z, and hence this basis was paired with (EOM)-CCSDT.

Spectroscopic constants were obtained for the $1^1\Sigma$ and $2^1\Sigma$ states of CaH^+ were obtained by computing 5 electronic energies around the approximate r_e for each state, evenly spaced by 0.025 Å, and finding the quartic polynomial uniquely defined by these 5 points. Spectroscopic constants are then computed from this polynomial. Due to the Born-Oppenheimer approximation, the same electronic energies are used to obtain the spectroscopic constants for CaD^+, although the differing mass of deuterium vs hydrogen of course affects some of the constants like ω_e. Our best values at the (EOM)-CCSDT/cc-pCV5Z level of theory are presented in **Table A.1**. Convergence of the spectroscopic constants with respect to basis set and correlation treatment can be examined in the Appendix.

All computations were executed through Psi4, [155] with its driver module parsing user input and managing the computation. As part of a project under development, the Quantum Chemistry Common Driver and Databases (QCDB), Psi4 can run its own modules, other interfaced modules (e.g., MRCC [156]), and even other quantum chemistry programs (initially, CFOUR [157]). For this work, (EOM-)CCSD used code intrinsic to Psi4, CCSDT used Cfour, and EOM-CCSDT and (EOM-)CCSDTQ used MRCC, all from a unified input format. Spectroscopic constants were obtained through Psi4's diatomic anharmonicity module.

These new theoretical results account for many differences seen between the previous predictions and experimental results, **Table 3.1**. Various basis sets (cc-pCV5Z vs cc-pCVTZ) adjust the absolute difference to 70-300 cm^{-1}, compared to the previous 687 cm^{-1} shift.

3.2.3   Theoretical Parameter Selection
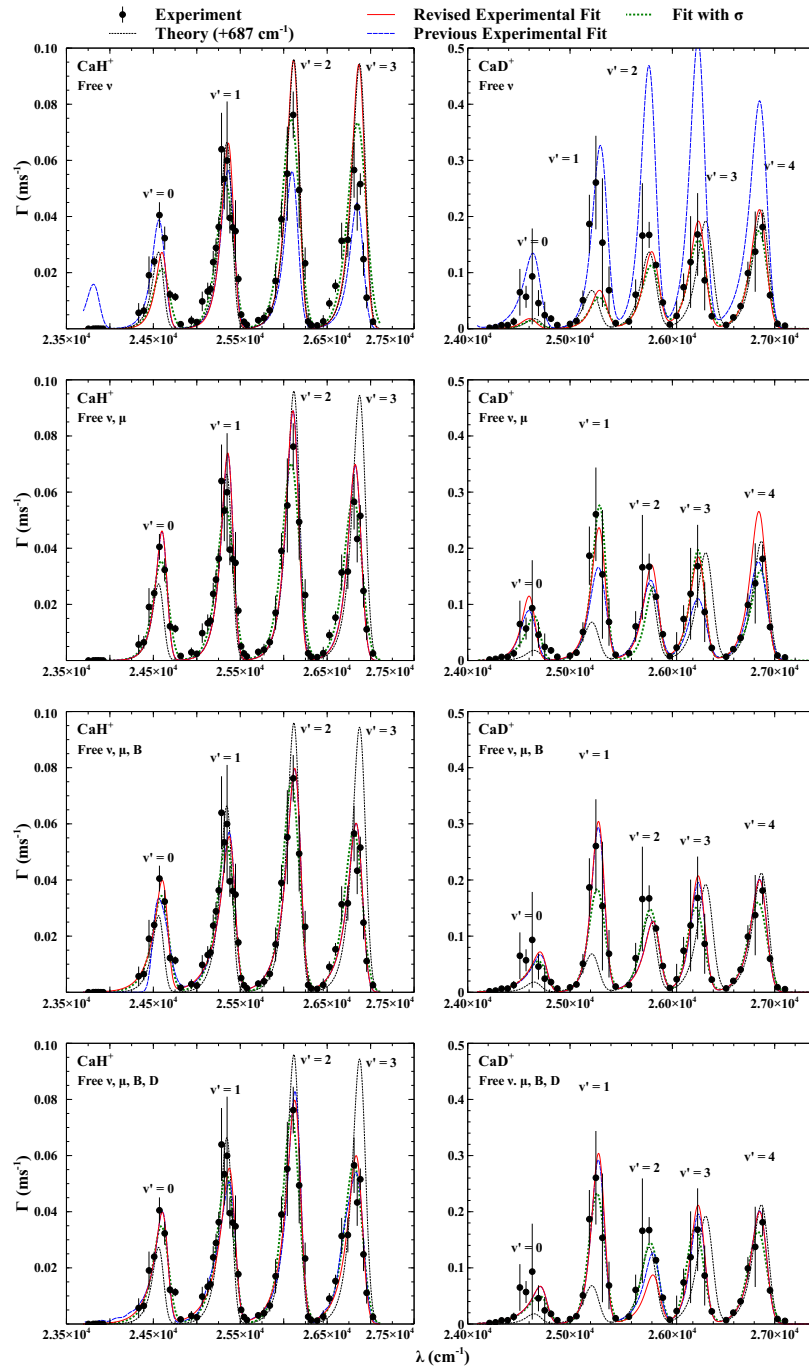
Figure 3.5: Parameter Determination for CaH^+ and CaD^+ Vibronic Transitions. All spectra generated from simple model, **Section 2.3**, where σ is assumed to be 80 cm^{-1} when not a free parameter. Constants listed in **Table 3.3**, **Table 3.4**, **Table 3.5**, **Table 3.6**, **Table 3.7**, **Table 3.8**, **Table 3.9**, **Table 3.10**, **Table 3.11**, **Table 3.12**, **Table 3.13**, and **Table 3.14**.
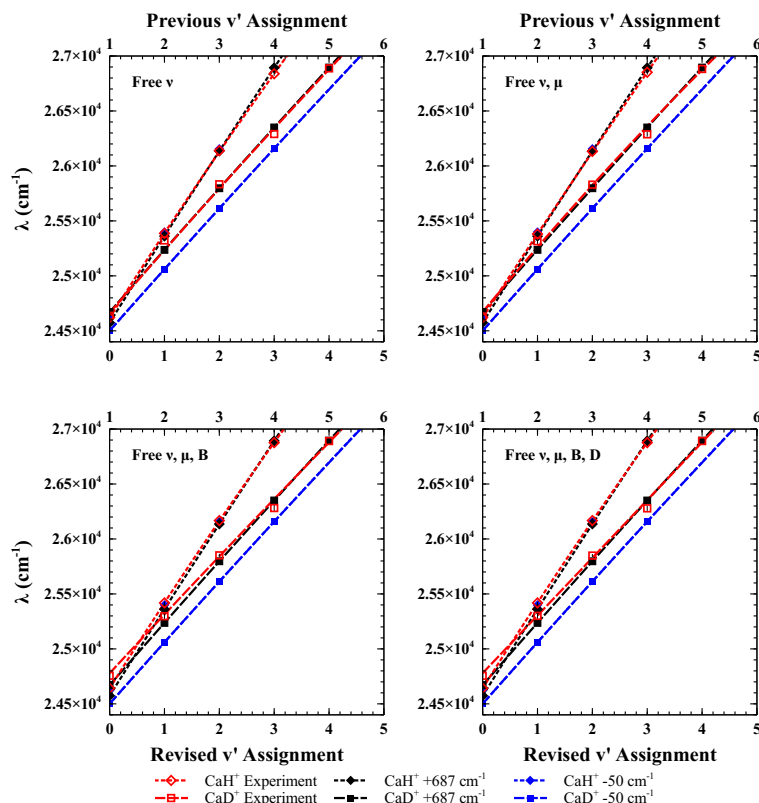
Figure 3.6: Vibronic Parameter Determination for CaH^+ and CaD^+ Vibronic Transitions. All spectra generated from simple model, **Section 2.3**, where σ is assumed to be 80 cm^{-1} when not a free parameter. Constants listed in **Table 3.3**, **Table 3.4**, **Table 3.5**, **Table 3.6**, **Table 3.8**, and **Table 3.11**.

Due to time constants, only the simple model can optimize parameters. The spectrum from the simple model has requires four physical constants for CaH^+ (vibronic transition $G_{0\to1}(v')$, rotational constant $B_{n,v'}$, distortion constants $D_{n,v'}$, and transition dipole moments $\mu_{v\to v'}$), and three laser parameters (laser linewidth σ, peak intensity I_0, laser frequency λ). By turning these parameters on and off, optimizations produce different experimental fits, **Figure 3.5**.

Since not enough information is known about the ground state, we assume that the *ab initio* predictions are correct for that state. The average shift from theory for $2^1\Sigma$ state in CaH^+ is 708 cm^{-1} while the average shift in CaD^+ is 670 cm^{-1}. This difference could originate from ill-estimated well-depths, ill-estimated ground states, or an isotopic affect.

The parameter $\mu_{0\to2}$ is well-defined in both isotopes, and this was used as a reference to find relative peak heights, **Table 3.3**, **Table 3.4**, **Table 3.7**, **Table 3.9**, and **Table 3.12**. This new data cannot accurately measure distortion constants still, since the data is not precise enough and would require a narrower laser linewidth. The current linewidth is measured at 373nm and assumed to never change across the spectrum. Ultimately, the fit from keeping σ and $D_{n,v'}$ constant was choose as the most reasonable experimental fit.

Table 3.3: CaH$^+$ Theoretical Parameters

v'	$\lambda\ cm^{-1}$ [1]	$\frac{\mu_{0\to v'}}{\mu_{0\to2}}$ [2]	$B_{1,v'}\ cm^{-1}$ [2, 115]	$D_{1,v'}\ cm^{-1}$ [2, 115]
0	24626	0.53	3.05	1.80e-4
1	25413	0.83	3.00	1.74e-4
2	26188	1.00	2.94	1.72e-4
3	26945	1.00	2.88	1.74e-4

Table 3.4: CaD$^+$ Theoretical Parameters [2, 115]

v'	$\lambda\ cm^{-1}$	$\frac{\mu_{0\to v'}}{\mu_{0\to2}}$	$B_{1,v'}\ cm^{-1}$	$D_{1,v'}\ cm^{-1}$
0	24509	0.36	1.57	4.75e-5
1	25075	0.70	1.55	4.62e-5
2	25636	1.00	1.53	4.56e-5
3	26189	1.19	1.51	4.51e-5
4	26734	1.26	1.49	4.55e-5

Table 3.5: CaH$^+$ Optimized Vibronic λ (cm^{-1}) with Free λ and Free σ

v'	CaH$^+$ Previous	CaH$^+$ Revised	CaD$^+$ Previous	CaD$^+$ Revised
0	-	24621 ± 35	-	24686 ± 97
w/ σ	-	24628 ± 30	-	25191 ± 1
1	24622 ± 15	25387 ± 16	24682 ± 55	25324 ± 63
w/ σ	24621 ± 16	25367 ± 13	-	25846 ± 1
2	25383 ± 14	26139 ± 37	25326 ± 49	25799 ± 12
w/ σ	25367 ± 11	26122 ± 20	-	26358 ± 0
3	26129 ± 47	26839 ± 18	25798 ± 11	26278 ± 10
w/ σ	26124 ± 25	26833 ± 16	-	26817 ± 0
4	26862 ± 24	-	26280 ± 11	26896 ± 11
w/ σ	26848 ± 22	-	-	27413 ± 0
5	-	-	26897 ± 11	-
w/ σ	-	-	-	-

Table 3.6: CaH$^+$ Optimized Vibronic λ (cm^{-1}) with Free λ, μ and Free σ

v'	CaH$^+$ Previous	CaH$^+$ Revised	CaD$^+$ Previous	CaD$^+$ Revised
0	-	24620 ± 16	-	24630 ± 27
w/ σ	-	24621 ± 17	-	24631 ± 25
1	24622 ± 16	25381 ± 15	24688 ± 33	25315 ± 24
w/ σ	24622 ± 17	25366 ± 11	24713 ± 28	25313 ± 22
2	25383 ± 14	26132 ± 39	25317 ± 19	25830 ± 10
w/ σ	25368 ± 11	26123 ± 19	25306 ± 20	25826 ± 10
3	26137 ± 36	26852 ± 21	25836 ± 11	26288 ± 21
w/ σ	26125 ± 19	26840 ± 17	25815 ± 10	26289 ± 26
4	26853 ± 21	-	26280 ± 19	26882 ± 11
w/ σ	26843 ± 17	-	26274 ± 24	26882 ± 13
5	-	-	26906 ± 13	-
w/ σ	-	-	26904 ± 14	-

Table 3.7: CaH$^+$ Optimized Vibronic Transition Dipole Moments ($\frac{\mu_{v'}}{\mu_2}$) with Free λ, μ and Free σ

v'	CaH$^+$ Previous	CaH$^+$ Revised	CaD$^+$ Previous	CaD$^+$ Revised
0	-	0.71 ± 0.07	-	0.81 ± 0.08
w/ σ	-	0.70 ± 0.05	-	0.78 ± 0.07
1	0.78 ± 0.08	0.90 ± 0.08	0.59 ± 0.05	1.18 ± 0.16
w/ σ	0.80 ± 0.06	0.88 ± 0.06	0.72 ± 0.06	1.07 ± 0.13
2	1.00 ± 0.09	1.00 ± 0.15	1.00 ± 0.12	1.00 ± 0.03
w/ σ	1.00 ± 0.06	1.00 ± 0.12	1.00 ± 0.12	1.00 ± 0.02
3	1.11 ± 0.17	0.89 ± 0.10	0.68 ± 0.01	1.05 ± 0.16
w/ σ	1.14 ± 0.13	0.92 ± 0.08	0.89 ± 0.02	0.88 ± 0.14
4	0.99 ± 0.11	-	0.85 ± 0.13	1.27 ± 0.07
w/ σ	1.04 ± 0.09	-	0.83 ± 0.13	1.12 ± 0.06
5	-	-	0.84 ± 0.04	-
w/ σ	-	-	0.90 ± 0.04	-

Table 3.8: CaH$^+$ Optimized Vibronic λ (cm^{-1}) with Free λ, μ, B and Free σ

v'	CaH$^+$ Previous	CaH$^+$ Revised	CaD$^+$ Previous	CaD$^+$ Revised
0	-	24642 ± 17	-	24753 ± 28
w/ σ	-	24637 ± 17	-	24745 ± 29
1	24565 ± 17	25418 ± 11	24756 ± 29	25299 ± 20
w/ σ	24637 ± 17	25381 ± 11	24734 ± 31	25290 ± 19
2	25416 ± 11	26167 ± 21	25297 ± 21	25851 ± 11
w/ σ	25381 ± 11	26122 ± 19	25283 ± 505	25816 ± 10
3	26168 ± 21	26876 ± 19	25851 ± 11	26279 ± 18
w/ σ	26122 ± 19	26851 ± 17	25796 ± 10	26233 ± 22
4	26876 ± 19	-	26281 ± 19	26891 ± 12
w/ σ	26851 ± 17	-	26258 ± 26	26878 ± 12
5	-	-	26891 ± 12	-
w/ σ	-	-	26872 ± 13	-

Table 3.9: CaH$^+$ Optimized Vibronic Transition Dipole Moments ($\frac{\mu_{v'}}{\mu_2}$) with Free λ, μ, B and Free σ

v'	CaH$^+$ Previous	CaH$^+$ Revised	CaD$^+$ Previous	CaD$^+$ Revised
0	-	0.72 ± 0.06	-	0.82 ± 0.07
w/ σ	-	0.71 ± 0.05	-	0.70 ± 0.05
1	0.73 ± 0.06	0.88 ± 0.06	0.58 ± 0.05	1.40 ± 0.16
w/ σ	0.81 ± 0.06	0.87 ± 0.06	1.20 ± 0.05	1.09 ± 0.13
2	1.00 ± 0.07	1.00 ± 0.13	1.00 ± 0.12	1.00 ± 0.02
w/ σ	1.00 ± 0.06	1.00 ± 0.11	1.00 ± 0.26	1.00 ± 0.02
3	1.15 ± 0.14	0.87 ± 0.08	0.73 ± 0.01	1.18 ± 0.16
w/ σ	1.14 ± 0.13	0.91 ± 0.07	1.62 ± 0.02	0.98 ± 0.14
4	1.00 ± 0.09	-	0.84 ± 0.12	1.23 ± 0.06
w/ σ	1.04 ± 0.08	-	1.49 ± 0.12	1.08 ± 0.05
5	-	-	0.90 ± 0.04	-
w/ σ	-	-	1.77 ± 0.05	-

Table 3.10: CaH$^+$ Optimized Vibronic Rotational Constant (cm^{-1}) with Free λ, μ, B and Free σ

v'	CaH$^+$ Previous	CaH$^+$ Revised	CaD$^+$ Previous	CaD$^+$ Revised
0	-	1.7 ± 0.9	-	0.8 ± 0.2
w/ σ	-	2.2 ± 0.7	-	0.8 ± 0.2
1	5.2 ± 0.4	1.3 ± 0.6	0.7 ± 0.2	1.8 ± 0.2
w/ σ	2.2 ± 0.7	2.5 ± 0.4	0.9 ± 0.2	1.9 ± 0.2
2	1.5 ± 0.5	2.0 ± 0.6	1.8 ± 0.2	1.2 ± 0.1
w/ σ	2.5 ± 0.4	3.0 ± 0.5	2.0 ± 1.2	1.7 ± 0.1
3	1.9 ± 0.6	1.9 ± 0.5	1.2 ± 0.1	1.7 ± 0.3
w/ σ	3.0 ± 0.5	2.6 ± 0.4	2.0 ± 0.1	2.2 ± 0.3
4	1.9 ± 0.5	-	1.7 ± 0.3	1.4 ± 0.1
w/ σ	2.6 ± 0.4	-	1.9 ± 0.3	1.5 ± 0.1
5	-	-	1.4 ± 0.1	-
w/ σ	-	-	1.6 ± 0.1	-

Table 3.11: CaH$^+$ Optimized Vibronic λ (cm^{-1}) with Free λ, μ, B, D and Free σ

v'	CaH$^+$ Revised	CaH$^+$ Revised w/ σ	CaD$^+$ Revised	CaD$^+$ Revised w/ σ
0	24642 ± 17	24633 ± 17	24756 ± 39	24759 ± 30
1	25418 ± 11	25382 ± 11	25300 ± 26	25273 ± 16
2	26167 ± 21	26123 ± 19	25849 ± 14	25814 ± 10
3	26877 ± 19	26853 ± 17	26279 ± 23	26225 ± 20
4	-	-	26891 ± 15	26875 ± 12

Table 3.12: CaH$^+$ Optimized Vibronic Transition Dipole Moments ($\frac{\mu_{v'}}{\mu_2}$) with Free λ, μ, B, D and Free σ

v'	CaH$^+$ Revised	CaH$^+$ Revised w/ σ	CaD$^+$ Revised	CaD$^+$ Revised w/ σ
0	0.72 ± 0.06	0.71 ± 0.05	0.97 ± 0.09	0.70 ± 0.05
1	0.88 ± 0.06	0.87 ± 0.06	1.70 ± 0.23	1.23 ± 0.13
2	1.00 ± 0.13	1.00 ± 0.11	1.00 ± 0.23	1.00 ± 0.02
3	0.87 ± 0.08	0.91 ± 0.07	1.45 ± 0.24	1.07 ± 0.13
4	-	-	1.50 ± 0.09	1.11 ± 0.05

Table 3.13: CaH$^+$ Optimized Vibronic Rotational Constant (cm^{-1}) with Free λ, μ, B, D and Free σ

v'	CaH$^+$ Revised	CaH$^+$ Revised w/ σ	CaD$^+$ Revised	CaD$^+$ Revised w/ σ
0	1.7 ± 0.9	2.5 ± 0.7	0.7 ± 0.3	0.6 ± 0.2
1	1.3 ± 0.5	2.4 ± 0.4	1.8 ± 0.3	2.1 ± 0.2
2	2.0 ± 0.6	3.0 ± 0.5	1.3 ± 0.4	1.8 ± 0.1
3	1.9 ± 0.5	2.5 ± 0.4	1.7 ± 0.8	2.3 ± 0.2
4	-	-	1.4 ± 0.2	1.6 ± 0.1

Table 3.14: CaH$^+$ Optimized Vibronic Rotational Distortion Constant (cm^{-1}) with Free λ, μ, B, D and Free σ

v'	CaH$^+$ Revised	CaH$^+$ Revised w/ σ	CaD$^+$ Revised	CaD$^+$ Revised w/ σ
0	-2.0E-4 $\pm$ 2.3E-2	1.4E-3 $\pm$ 1.5E-2	-1.4E-5 $\pm$ 2.2E-3	-8.8E-5 $\pm$ 2.1E-3
1	-1.6E-4 $\pm$ 5.1E-3	-2.3E-4 $\pm$ 5.8E-3	-4.3E-5 $\pm$ 1.5E-3	-6.3E-6 $\pm$ 1.0E-3
2	-2.0E-4 $\pm$ 6.1E-3	-6.5E-4 $\pm$ 6.2E-3	-4.5E-5 $\pm$ 2.0E-3	-3.8E-5 $\pm$ 7.0E-4
3	-1.8E-4 $\pm$ 6.4E-3	-1.0E-3 $\pm$ 3.9E-3	-8.4E-5 $\pm$ 9.9E-3	-3.6E-5 $\pm$ 1.1E-3
4	-	-	-4.6E-5 $\pm$ 1.1E-3	1.4E-4 $\pm$ 7.0E-4

3.3   Conclusion

The vibronic spectrum of CaD$^+$ was obtained by scanning a frequency-doubled Ti:Sapph laser over the frequencies predicted to excite $2^1\Sigma$ vibrational modes before coupling to unbound electronic states. Collection of Ca$^+$ fluorescence allowed us to quantify the rate of CaD$^+$ dissociation and plot it against frequency at constant laser linewidth and intensity. The harmonic constant $\omega_1 = 537 \pm 102$ cm^{-1} and anharmonicity $\omega\chi_1 = 0 \pm 20$ cm^{-1} of the $2^1\Sigma$ state were extracted by fitting our experiments to a second-order vibrational energy expression, **Equation 3.2**. Comparison of the simulated experiment with MS-CASPT2 predictions revealed a 687 cm^{-1} average deviation from standing theory. CaH$^+$ vibrational levels within $2^1\Sigma$ were consequently reassigned by reducing the vibrational quantum number by one relative to the previous assignment [108].

To understand this disagreement, we required further information on the ground and excited electronic states of CaH$^+$. New theoretical estimates were found by unfreezing core electrons through (EOM)-CCSDT/cc-pCV5Z, which accounted for majority of the difference. Experiments using mid-infrared spectroscopy to measure lower vibrational transitions of the ground-state can be combined with previous vibrational overtone data

[137] to construct a $1^1\Sigma$ potential energy. Probing higher-lying electronic states could offer insight into photodissociation rates and explain why they differ from theoretical expectations. Future experiments will also include examination of the $2^1\Sigma$ state with rotational resolution, improving the precision of the constants presented here.

CHAPTER 4

CAH$^+$ ROVIBRONIC TRANSITIONS

The first bound transition in CaH$^+$ was observed for two vibrational overtone transitions within the ground electronic state for a single CaH$^+$ sympathetically cooled by two Ca$^+$ [137]. In order to obtain rotational resolution, we used a stronger electric dipole transition to study. Four vibronic peaks were previously measured for the $1^1\Sigma, v = 0 \rightarrow 2^1\Sigma, v' = 0, 1, 2, 3$ electronic transition [108] and the peak assignment was verified using the deuterated isotopologue [158]. In our experiment, a pulse shaping technique was used to tighten the range of frequency components and obtain rotational resolution of the $1^1\Sigma, v = 0 \rightarrow 2^1\Sigma, v' = 0, 1, 2, 3$ transition.

4.1   Methods

The experimental setup for the vacuum system and ion trap are discussed in ref [108]. A frequency doubled Ti:sapph laser was chosen for the spectroscopy of CaH$^+$ because of the high tunability and ease of frequency doubling when mode locked. When mode-locked, the laser has a pulse width of around 300 fs, and a linewidth too broad to resolve rotational transitions. In order to narrow the linewidth, we employed a 4-f pulse shaping system [159]. The pulsed laser is spectrally dispersed angularly by a holographic grating (Thorlabs GH25 with 3600 lines/mm). A focal point away, a cylindrical lens (f=500mm) performs a Fourier transform to convert angular dispersion to spatial dispersion. At the focal point of the lens, a 76 micron slit spatial mask is used to pick out desired frequency components. The slit lies directly in front of a mirror and second pass recombines the selected frequency components into a collimated beam. The mirror is tilted vertically to spatially separate the outgoing pulse shaped beam from the incoming beam in order to pick the beam with a D-shaped mirror and send to the trap. 76 microns is the narrowest the slit width achieved

without spatial diffraction of the outgoing beam. The pulse shaped beam is co-aligned to the axial direction of the trap. A shutter (Vincent Associates Model V51452T0 Serial 11355) is used to switch the beam.

For each dissociation measurement, the ions are exposed to the beam alternating between on and off with a time of 8 ms each for 10 cycles. The fluorescence is detected for 200 μs, and the process is repeated 250 times **Figure 4.1** to give a typical fluorescence plot **Figure 4.2**. The dissociation and detection times are determined empirically to maximize the dissociation signal. The dissociation laser power was kept between 20 and 150 μW and the rate in this regime showed no significant power dependence.
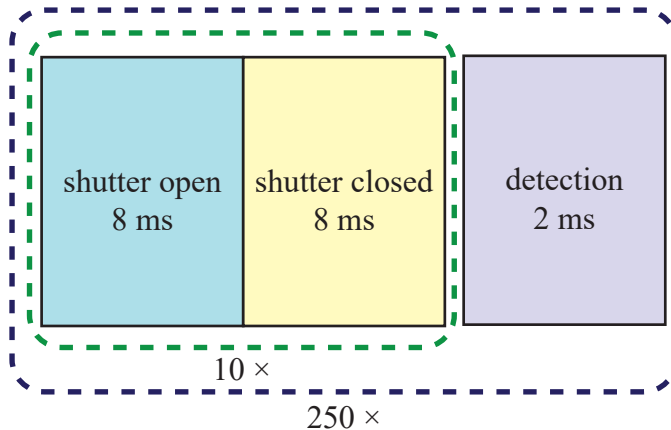
Figure 4.1: The dissociation sequence used to expose the molecular ions to the dissociation beams. The 250 fluorescence values are shown in **Figure 4.2** for three sample wavelengths.

The plot compares two regimes of dissociation. Off resonance, no dissociation is seen and is entered as 0 on the spectrum. On resonance, the fluorescence increase is fit to an exponential curve to model a first order dissociation process:

$$A_\infty - (A_\infty - A_0 e^{-\Gamma(\lambda)t}) \tag{4.1}$$

where A_0 represents the initial fluorescence, A_∞ is the steady state florescence, and Γ

is the rate recorded to produce the spectrum. Sample dissociation curves for three experimental runs at different wavelengths are shown in **Figure 4.2**. The data points for the spectrum **Figure 4.3** are the average of five fitted points and vertical error bars are the standard deviation. The entire range studied with vibronic resolution [108] was studied with rotational resolution and is discussed in the results.
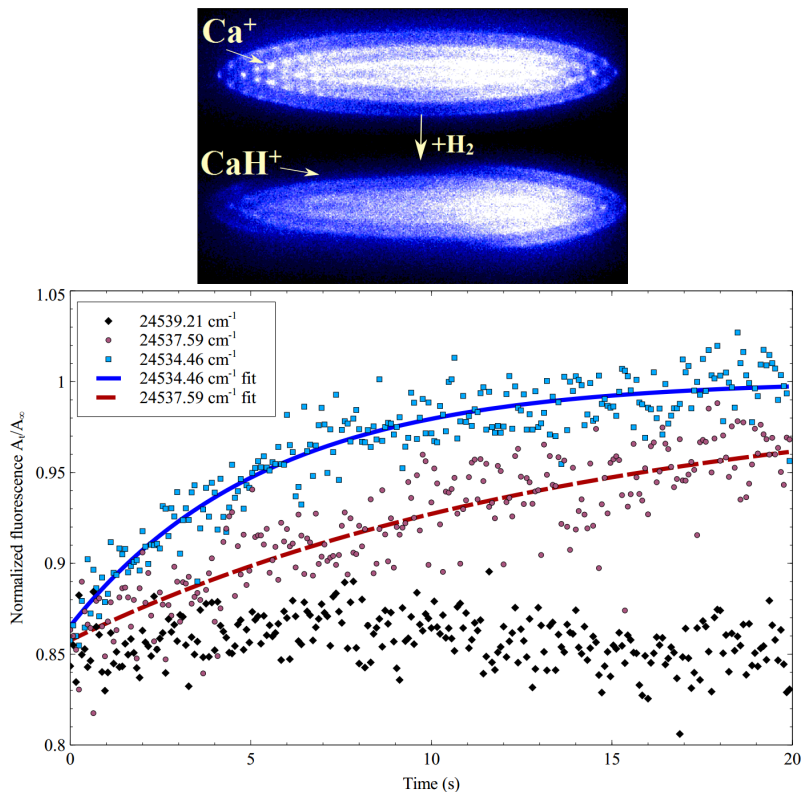
Figure 4.2: A Coulomb crystal of Ca^+ reacts with H_2 to form CaH^+ and Ca^+ with an associated decrease on fluorescence over the course of several minutes. CaH^+ is more stably trapped on the outer edge of the composite Coulomb crystal due to the increased mass compared to Ca^+. The asymmetry of the crystal is due to radiation pressure on the Ca^+ (top). Fluorescence recovers when the laser is on resonance with a rovibronic transition of CaH^+ to form Ca^+. A typical dissociation scan for three wavelengths showing the normalized fluorescence over exposure time is used to extract dissociation rates (bottom). The 407.511 nm scan shows no detectable dissociation. The other two are fit to **Equation 4.1** to model a first order dissociation process.

4.2 Results and Discussion

Measuring the dissociation rate as a function of wavelength yielded a series of peaks **Figure 4.3**, corresponding to transitions from $1^1\Sigma, v = 0, J \rightarrow 2^1\Sigma, v' = 0 - 4, J'$. The horizontal error bars are the standard error of the residuals from the calibration curve. The dissociation pathway is not known, though we assume that the limiting step is the excitation to the first excited state and that the second photon causes dissociation instantaneously. This assumption is reasonable and was used to model the vibronic spectrum in CaH^+ [108, 158] with decent agreement with the predicted transition dipole moments [2]. In contrast to the previous experiment [108, 158] when the broad-linewidth laser dissociated multiple rotational states at once, we observe much slower fluorescence recovery likely due to the fact that only one rotational level is addressed in the ground state at a given time.

The measured dissociation rate is not a quantitative indication of the transition strength or population in the rotational levels. This is due to the fact that we do not know the exact dissociation pathway. Over the course of the fluorescence recovery scan, rethermalization populates the levels depleted by dissociation at a rate lower than the dissociation rate giving the measured rate. While the assumption of a first order dissociation rate over the course of the experiment is an approximation, it does provide a method to obtain a rotational spectrum to determine transition frequencies and spectroscopic constants.

To extract rotational constants from the experimental data, each peak was assigned to a specific transition. Vibronic transition assignments are from CaH^+ and CaD^+ experiments [158]. Since the laser beam profile is unknown, only the rovibronic transition frequency can be matched and not the exact peak shape or width. The transition frequency is taken as the weighted average of the data points in each peak:

$$\lambda(v', J, J') = \frac{\sum_i \Gamma_i \lambda_i}{\sum_i \Gamma_i} \tag{4.2}$$

where λ_i refers to the frequency of the data point, and Γ_i is the dissociation rate at that

point. The total dissociation for the peak is used as a normalizing factor.

The initial theoretical spectrum was produced using *ab initio* predictions with the physical parameters $\lambda(v'), B_{1,v'}, D_{1,v'}, B_{00}, D_{00}$. The primed symbols refer to levels in the $2^1\Sigma$ state. The transitions were given an absolute shift of 257 cm^{-1} initially. The optimization parameters were found through a Nelder-Mead algorithm to minimize the χ^2 difference. We did not assign transitions manually, as there is chance for mis-assignments. Instead, we let minimization program assign and re-assign transitions as needed. The error function is a a weighted summation of type one and type two error. Type one error gives a consequence for experiment transitions far removed from theory predictions, while type two error gives the reverse. Per each experimental transition, the type one error is the minimum χ^2 difference between the experimental peak and all other theoretical transitions. On the other hand, the type two error has the minimum χ^2 difference between the theoretical peak and all other experimental transitions. This forces all predicted transitions to match the spectrum with no deviations. The weight for each error type is derived from the Boltzmann distribution of the ground state population. This forces stronger transitions to be favored over weaker transitions. Results are shown in **Table ??**. The error bars are calculated from covariance matrix derived from the Hessian. An example spectrum and Fortrat diagram showing the optimized theoretical results are shown in **Figure 4.3**.

The rovibronic results predict an average shift of 266 ± 47 cm^{-1} from theory. The rotational constants match well with theory, however the distortion constants are very inconsistent. This is due to the limited resolution obtained by the pulse shaping method. The P and R branches are too close to be resolved using this method, hence the centrifugal distortion term cannot be accurately distinguished. In addition, a peak at 25920 cm^{-1} could not be assigned with the method used. This could possibly be attributed to a two photon dissociation to another state through a pathway not currently understood. It is worth noting that this transition is close to the Doppler cooling frequency of the

Table 4.1: Optimized parameters for the experimental fit for the excited (top) and ground vibrational (bottom) states are compared to theoretical parameters for the predicted spectrum. $G_{1,v'}$ was taken from reference [158]. The $B_{n,v}$ and $D_{n,v}$ values were taken from [2, 115]. All values reported are in cm^{-1}. The $\lambda(v')$ is the $J = 0 \rightarrow J' = 0$ transition.

v'	$\lambda(v')$	$B_{1,v'}$	$D_{1,v'}$
0 Thr.	24294	3.05	1.80×10^{-4}
0 Exp.	24603 ± 29	3.03 ± 0.04	-0.0002 ± 0.0003
1 Thr.	25073	3.00	1.74×10^{-4}
1 Exp.	25369 ± 16	2.86 ± 0.04	-0.0003 ± 0.0002
2 Thr.	25861	2.94	1.72×10^{-4}
2 Exp.	26118 ± 16	2.86 ± 0.02	-0.0001 ± 0.0
3 Thr.	26655	2.88	1.74×10^{-4}
3 Exp.	26859 ± 23	2.87 ± 0.01	0.0 ± 0.0
v	$G_0(v)$	$B_{0,v}$	$D_{0,v}$
0 Thr.	759	4.711	1.99×10^{-4}
0 Exp.	-	4.73 ± 0.01	-0.0002 ± 0.0

co-trapped Ca$^+$.
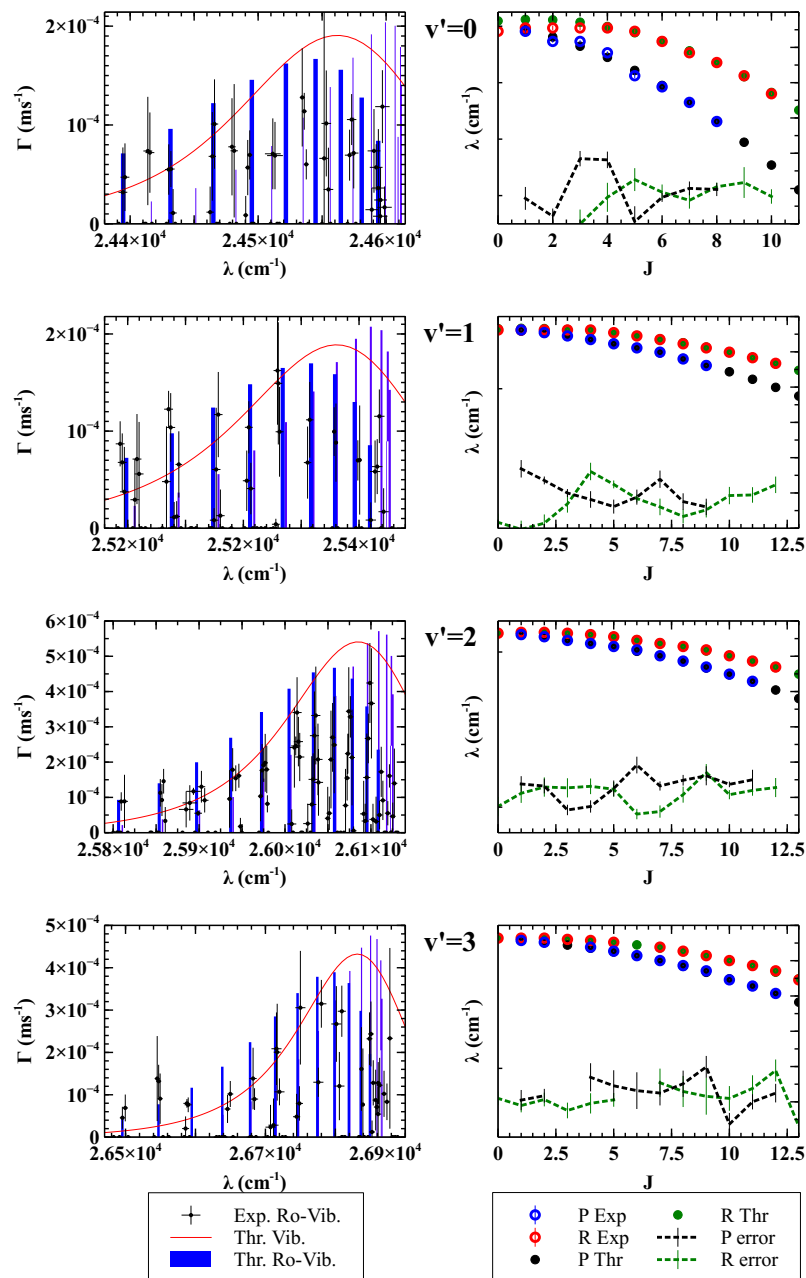
Figure 4.3: The resulting rovibronic spectrum for each previously measured vibronic peak. (Left) The vibronic measurement in red corresponds to the spectroscopy done before pulse shaping where the linewidth of the femtosecond laser covered multiple rotational transitions. Generated from simple model, **Equation 2.42**. The black data points correspond to measurements taken after the linewidth was narrowed to obtain suitable resolution. Each data point is an average of five dissociation measurements and gaps in between peaks were verified to have no dissociation. Expected peak positions determined from the rotational constants of the optimized fits of the experimental data are shown as blue bars. (Right Top) a Fortrat diagram for the same transition with experimentally assigned peak locations, corresponding optimized theoretical peak locations, and (Right bottom) the residual between the two.

Table 4.2: Spectroscopic constants obtained from the rovibronic spectrum of CaH^+ compared to the constants determined from vibronic spectroscopy [158] and CCSDT [158]. All values reported are in cm^{-1}.

	CaH^+ Rovibronic	CaH^+ Vibronic	Theory
T(0,1)	24217 ± 3	24239 ± 5	23907
ω_1	776 ± 4	813 ± 6	772
$\omega\chi_1$	6 ± 1	16.8 ± 1.4	3.8

4.2.1 Vibration Constant Assignment

Finally, the results were used to extract information about the vibrational constants. Using the same procedure as before, the optimized T(0,1), ω_1 and $\omega_1\chi_1$ were solved obtain the values shown in **Table 4.2**.

These constants match well with the vibronic data for CaH^+ as seen in **Figure 4.4**. The rovibronic results match theoretically predicted parameters better than vibronic results. This is because the vibronic results are largely affected by unknown dissociation pathway. The exact pathway affects transition strength and may even shift the vibronic transition frequency. At rovibronic level, the dissociation pathway is irrelevant. The pathway can only affect the transition strength, not the actually frequency. This is why rovibronic results match theory better. The electronic transition still shows a 310 ± 3 cm^{-1} shift from theory.
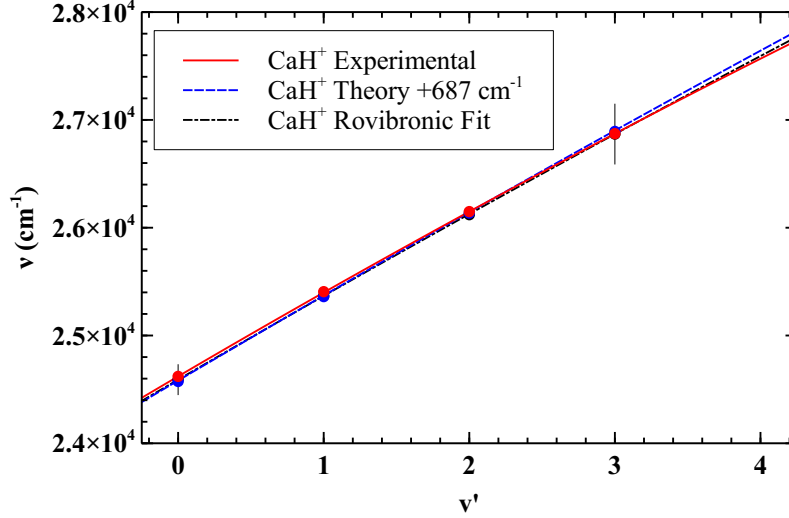
Figure 4.4: The vibronic transitions for CaH^+ using experimental values from the vibronic [158] and rovibronic experiments and their associated fits are compared to *ab initio* theory. Exact parameters are in **Table 4.1**.

4.3   Conclusion and Outlook

The spectrum and rotational constants obtained here represent the highest precision measurements available for CaH^+. The results may prove useful in the validation of the presence of this molecular ion in the solar atmosphere. Knowledge of the transition energies also provide a method of state readout for proposed methods of rotational cooling by a cryogenic chamber [160, 161], sympathetic cooling with a buffer gas of Doppler cooled atoms, or by optical pumping. One optical pumping scheme using a 6.9 micron laser to induce the $1^1\Sigma(v = 0, J = 1) \rightarrow 2^1\Sigma(v = 1, J = 2)$ transition.

In the absence of inelastic collisions from background gas, polar molecules have a rotational distribution determined entirely by blackbody radiation. Ion trap clocks using CO^+ and CaH^+ molecules have large uncertainties from the rotational distribution influence of BBR [13, 38]. On the atomic side, cesium fountain frequency standards have an uncertainty dominated by an AC Zeemann shift from uncertain BBR [162, 163]. Knowing the temperature of the BB source will help cancel the uncertainty for more

precision. Thus, molecular ions provide a convenient method of measuring temperature through their many rotational states [38]. This work provides a step forward in realizing the use of this particular ion in thermometry.

CHAPTER 5

APPLICATIONS TO OTHER PROBLEMS

This section discusses two particular applications of the simulation and simple model. The first half reports an analysis of the ninth and tenth overtones of the CaH^+ ground state. The second half depicts preliminary findings on the dissociation pathway in CaH^+.

5.1 CaH^+ Vibrational Transitions

Precision spectroscopy of molecules and molecular ions can yield insight into the fundamental physical constants and astrochemical processes [13, 15]. Coulomb crystals composed of laser-cooled atomic ions and molecular ions provide a pristine environment for studying the properties of molecules [17]. The laser-cooled atomic ions serve as both a coolant that reduces the temperature and a sensitive detector that allows for single molecule measurements. It is also a natural system for precision measurements of molecular ion transitions. Expanding these techniques to a wider array of molecular ion species remains a challenge due to the lack of experimental data on molecular ions transitions. This requires new methods for obtaining spectral information. The spatial localization of molecular ions in a Coulomb crystal results in the required ion density for spectroscopy with low ion numbers relative to traditional techniques. Systems built for high-precision measurement are often incompatible with the survey spectroscopy required to find unknown transitions. However, this is not the case for Coulomb crystals, where the long ion storage time provides multiple opportunities to probe the molecule and the fluorescence of the laser-cooled atomic ion serves as a fast, low-noise detector. CaH^+ is a candidate molecule for testing the possible variation in the proton-to-electron mass ratio [29, 31]. It is also expected to be relatively abundant in space due to observation of CaH, but has not yet been directly observed [37]. In both cases, laboratory measurements of

rovibrational transitions in CaH$^+$ are required for scientific progress.

5.1.1   Methods

We use laser cooled ^{40}Ca$^+$ ions to sympathetically cool ^{40}CaH$^+$ molecules. The experiment takes place in a chamber described previously [102]. The ^{40}Ca$^+$ ions are trapped in a rf Paul trap (r$_0$ = 0.5 mm) driven at $\Omega = 2\pi \times 14$ MHz to confine the ions radially, while static DC voltage applied at the endcaps confines the ions axially. The trap is kept at a base pressure of about 4×10^{-9} Pa. The ions are detected by laser induced fluorescence at 397 nm onto a photon multiplier tube (PMT) and electron multiplying charge coupled device (EMCCD) camera. A narrow bandpass filter is used to ensure that only 397nm light is detected.

A ^{40}CaH$^+$ molecule is produced by leaking about 5×10^{-7} Pa of molecular H$_2$ into the chamber via a leak valve. A chain consisting of three ^{40}Ca$^+$ ions is trapped before leaking in the H$_2$. The ^{40}CaH$^+$ is produced via reactive collisions in the gas phase between ^{40}Ca$^+(4P_{\frac{1}{2}})$ and the H$_2$ as ^{40}Ca$^+$ + H$_2 \rightarrow$ ^{40}CaH$^+$ + H. The occurrence of a reaction is determined when one of the ions goes dark and there is a drop in fluorescence counts. Once a reaction occurs, the leak valve is closed and the experiment is delayed until the base pressure is reached. After this pump down time, the internal degrees of freedom of the molecule are expected to be at room temperature due to weak coupling with the cold translational degrees of freedom. The identity of the molecule can be determined by resolved sideband spectroscopy [114] and under these experimental conditions we have only observed the formation of CaH$^+$.

To measure the vibrational overtones of ^{40}CaH$^+$, we use (1 + 1') REMPD. A broadband mode-locked Ti:Sapph (IR) laser excites a specific vibrational transition of ^{40}CaH$^+$, a second photon, a fixed ultraviolet (UV) cw laser (380nm) dissociates the ion from the upper vibrational state by coupling it to a repulsive electronic state (Fig. 2b). The IR laser power was 800 mW and the UV laser power was 200 μW. Upon dissociation, the

previously dark ^{40}CaH$^+$ ion, will be broken into Ca$^+$ + H, the Ca$^+$ will fluoresce again and there will be an increase in fluorescence counts as shown in Fig. 2. Other possible dissociation channels, including two UV photon absorption and UV induced electron bombardment, are measured to be low compared to the REMPD dissociation rates by performing control experiments with the IR blocked.

A pinhole before the PMT allows partial light collection from all three ions and reduces background due to scattered light. Misalignment from the crystal center results in three distinct collection efficiencies for each ion position. This allows us to detect the position of the dark ion from the fluorescence. The ion position shifts are due to collision with background gas. Three ions were used in the experiment because three ion chains with a dark ion resulted in faster recrystallization after a collision than two ion chains with a dark ion. Two ion chains required modulation of the laser for fast recrystallization after collisions.

The calculated values for CaH$^+$ properties are from Abe *et al.* [1] and based on the method NRel/cc-pCV5Z/CASPT2. The transition strength is proportional to the rate $r_d = 1/\langle \tau_d \rangle$.

5.1.2 Results
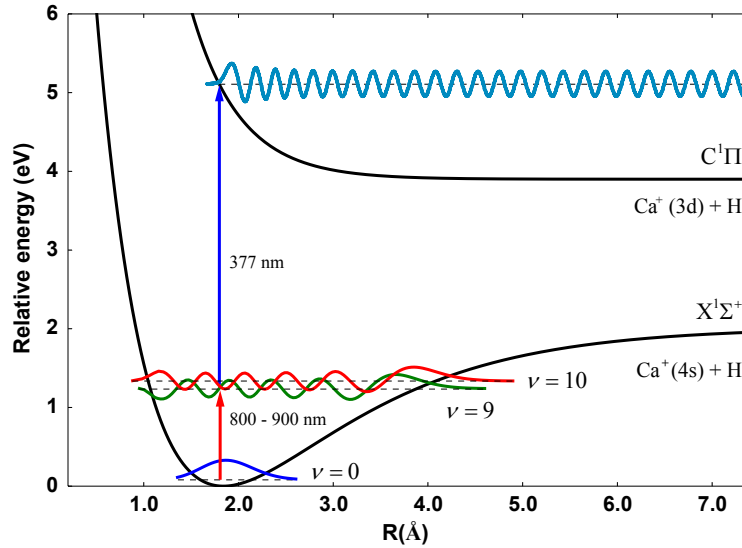
Figure 5.1: Simplified CaH$^+$ energy level diagram showing the overtones excited by a pulsed, tunable infrared laser (800-900 nm). A second ultraviolet laser (377 nm) excites the overtones to the unbound state to dissociate the molecule.
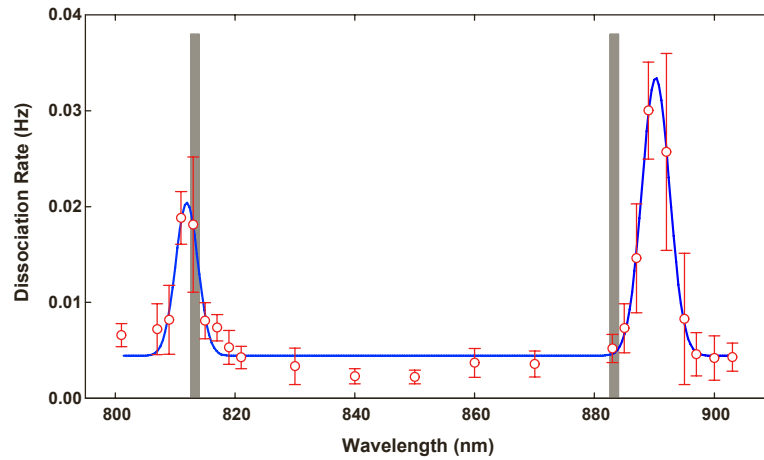
Figure 5.2: The measured τ_d are averaged over eight experiments and the inverse is plotted as a function of the IR wavelength. The data reveals two peaks which are fit assuming a Gaussian line shape. Gray bars are centered at the calculated theoretical values [1] for the $\nu' = 10 \leftarrow \nu = 0$ and $\nu' = 9 \leftarrow \nu = 0$ overtones. Error bars are the standard error of $r_d = 1/\langle \tau_d \rangle$, E_r, propagated from the standard deviation of $\langle \tau_d \rangle$, σ_τ: $E_r = \frac{r_d^2 \sigma_\tau}{\sqrt{8}}$.

Table 5.1: CaH$^+$ 9th and 10th Overtone Theoretical Overtone

v'	ν cm^{-1}	μ	B cm^{-1}	D cm^{-1}
9	12090	0.000092	3.652	0.00024777
10	13066	0.000055	3.483	0.00026575

We present the observation of two vibrational overtones of CaH$^+$ by two photon resonant photodissociation of single molecular ions (**Figure 5.1**). Although the molecular ion is at a translational temperature of a few millikelvin, the internal degrees of freedom are in equilibrium with the room temperature vacuum chamber via black body radiation. The calculated vibrational frequency of the molecule is 1478.4 cm^{-1} and we expect that the molecule will be in the ground vibrational state X$^1\Sigma^+$ greater than 99.9% of the time [1]. On the other hand, the calculated ground state rotational constant, 4.711 cm^{-1}, is small relative to room temperature. The rotational states will be populated with an expected value of $J = 5.36$ and the lowest ten J states are expected to have more than 94% of the population. Our experiment uses a single molecule at a time, but the blackbody radiation will randomize the J state on the order of minutes.

The spectrum clearly shows two peaks which we identify as the $\nu' = 10 \leftarrow \nu = 0$ and $\nu' = 9 \leftarrow \nu = 0$ overtones of CaH$^+$ based on theoretical calculations [1] (**Figure 5.2**).
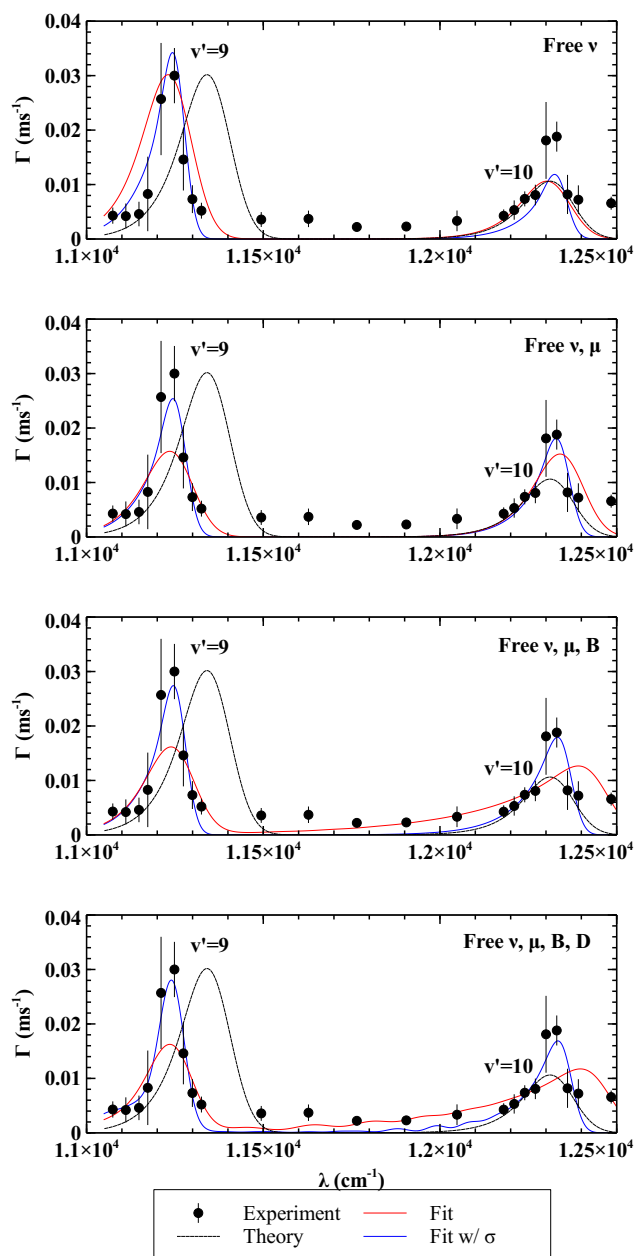
Figure 5.3: Optimized spectra from simple model. The various free parameters are the transition frequency, ν, the transition dipole moment, μ, the rotational constant, B, the first centrifugal constant, D, and the laser line width, ω. Data listed in **Table 5.2**,**Table 5.3**,**Table 5.4**, and **Table 5.5**.
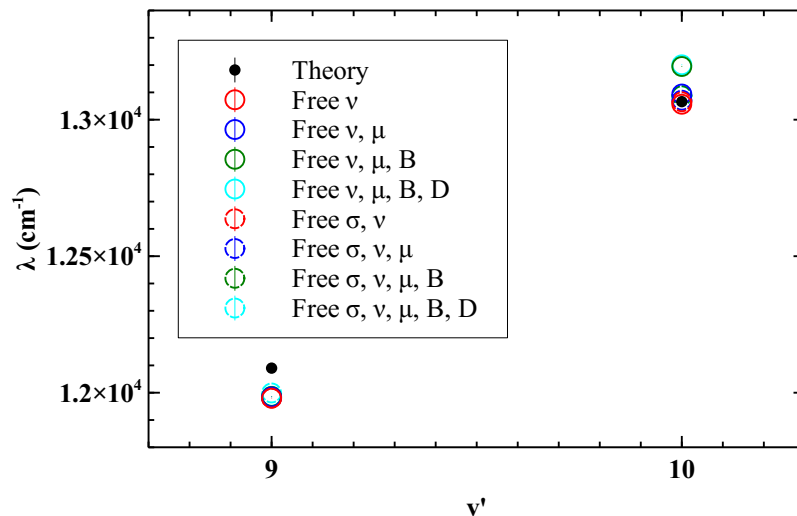
Figure 5.4: Optimized transition frequencies from **Figure 5.3** desplayed in Fortrat Diagram. Data listed in **Table 5.2**,**Table 5.3**,**Table 5.4**, and **Table 5.5**.

All theoretical analysis and optimizations used the simple model, **Equation 2.42**. The $\nu' = 10 \leftarrow \nu = 0$ transition centered around 812(3) nm, compared to the theoretical value of 813.3 nm, and the $\nu' = 9 \leftarrow \nu = 0$ transition centered around 890(3) nm, compared to the theoretical value of 883.3 nm, aline with observed differences between calculated and measured vibrational transition frequencies in other metal hydrides [1]. The eight optimizations differed by the free parameters: the transition frequency, ν, the transition dipole moment, μ, the rotational constant, B, the first centrifugal constant, D, and the laser line width, ω. When the laser width was constant, it was held at 80 cm^{-1}. Since the peak heights are relative, the dipole moments are recorded as relative to the $\nu' = 9 \leftarrow \nu = 0$ transition. Even with all the other parameters set as free, holding the line width constant could not account for the narrowness of the peaks, **Figure 5.3**. One of the main issues was optimizing the predicted baseline between the peaks, but even with the baseline removed, the optimizations did not match. The only other possible variable to affect the peak width is the laser line width, which produced better results, **Figure 5.3**. Based on optimizations, the laser line width is half of the original prediction. Of the optimizations, the free ν, μ, σ fit produces the best match while still having reasonable physical constants. None of the

80

predicted theoretical transition frequencies match theory perfectly, but all optimizations seem to match each other, **Figure 5.4**. Unfortunately, this data is insufficient to predict the v=0 energy state, with any degree of accuracy, as the high overtones need to many distortion constants to model their behavior.

Table 5.2: CaH$^+$ Optimized Overtone with Free ν, $\sigma = 40.54 \pm 0.06$ cm^{-1}

v'	ν cm^{-1}	ν w/ Free σ cm^{-1}
9	11980.2 ± 0.4	11979.8 ± 0.2
10	13056.5 ± 2.3	13065.7 ± 0.8

Table 5.3: CaH$^+$ Optimized Overtone with Free ν, μ, $\sigma = 43.55 \pm 0.04$ cm^{-1}

v'	ν cm^{-1}	ν w/ Free σ cm^{-1}	μ	μ w/ Free σ
9	11984.6 ± 0.5	11982.2 ± 0.2	μ_9	μ_9
10	13094.1 ± 1.1	13071.4 ± 0.3	$0.99 \pm 0.00 \, \mu_9$	$0.86 \pm 0.00 \, \mu_9$

Table 5.4: CaH$^+$ Optimized Overtone with Free ν, μ, B, $\sigma = 41.39 \pm 0.04$ cm^{-1}

v'	ν cm^{-1}	ν w/ Free σ cm^{-1}	μ	μ w/ Free σ	B cm^{-1}	B cm^{-1} w/ Free σ
9	11986.3 ± 0.9	11983.8 ± 0.2	μ_9	μ_9	3.71 ± 0.00	3.61 ± 0.00
10	13194.8 ± 1.2	13087.9 ± 0.3	$1.26 \pm 0.00 \, \mu_9$	$0.89 \pm 0.00 \, \mu_9$	-1.69 ± 0.00	2.76 ± 0.00

Table 5.5: CaH$^+$ Optimized Overtone with Free ν, μ, B, D, $\sigma = 40.60 \pm 0.03$ cm^{-1}

v'	ν cm^{-1}	ν w/ Free σ cm^{-1}	μ	μ w/ Free σ	B cm^{-1}	B cm^{-1} w/ Free σ	D cm^{-1}	D cm^{-1} w/ Free σ
9	11986.8 ± 0.9	11999.0 ± 0.2	μ_9	μ_9	3.73 ± 0.00	2.25 ± 0.00	0.0003 ± 0.0007	-0.0116 ± 0.0000
10	13201.0 ± 1.2	13087.6 ± 0.3	1.37 ± 0.00 μ_9	0.91 ± 0.00 μ_9	-3.74 ± 0.00	2.95 ± 0.00	0.0003 ± 0.0003	0.0132 ± 0.0000

5.1.3   Discussion

Our experimental setup was intended for high-precision quantum logic spectroscopy [63] experiments on molecular ions. We have shown that the same setup can be used for the preliminary large range spectroscopy necessary to observe even weak lines despite trapping only a few ions at a time. The next step for precision spectroscopy of CaH$^+$ is to reduce the rotational temperature by sympathetic cooling with neutral atoms and then rotationally resolve these transitions and the fundamental transition [62, 83].   Then quantum logic spectroscopy can be performed on ground state cooled Ca$^+$-CaH$^+$ crystals [76] in order to reach the precision necessary for observing relative changes in fundamental constants [64].

5.2   CaH$^+$ and CaD$^+$ Dissociation State Calculations

This next section focuses on determining the full dissociation pathway for CaH$^+$ and CaD$^+$ based on new theoretical studies combined with previous experimental evidence.

At this time, the work is inconclusive, as results are still inconclusive. Previous sections discussed possible [1 + 1'] resonance-enhanced multi-photon dissociation (REMPD) experiments without discussing the specific dissociation pathway. The pathway could inhibit or promote particular transitions which may affect the previously optimized transition strength, i.e. peak height. Accounting for these influences may explain many deviations, e.g. mismatched *ab initio* peak heights or inconsistent transition frequency adjustments, seen in previous sections. Based on the theoretical potential energy surfaces, both the $1^1\Sigma \rightarrow 2^1\Sigma$ electronic transitions and the $1^1\Sigma v = 0 \rightarrow 1^1\Sigma v' = x$ overtone transitions have a multitude of possible dissociation pathways, for CaH^+ and CaD^+. However, previous work discussed the experimental evidence contradicting the theoretical $2^1\Sigma$ PES curves, **Section 3**. As experiments are unable to verify the theoretical PES curves, this section focuses on entertaining the possibility of incorrect dissociation states. This study explores the possible affects this might have on experimental spectra from **Section 3** and **Section 4**.

5.2.1 Methods

The experimental set-up was discussed in detail in **Section 3** and **Section 4** [108, 158]. The laser frequency was tuned from 370 nm to 420 nm, and dissociation of CaH^+ and CaD^+ was collect at every 1 nm interval. Previous sections implement an analytical model where dissociation was assumed to abundantly faster than transitions and therefore irrelevant, **Equation 2.42**. The spectrum produced from this analytical model was optimized to fit the experimental peak maximum and peak height, which generated an experimental fit and experimental parameters. This work does not use the same model, as it cannot account for spectrum variation due to dissociation.

The theoretical methodology for this work uses a combination of the simple model, the full simulation model, and the stochastic model. The simple model, **Equation 2.41**, does not assume instantaneous dissociation, but instead uses a weighted sum of the

individual pathway dissociation rates. The weights come from the Boltzmann distribution of the ground state rotational population at 300K. By using this model, multiple competing pathways are quantitatively interlaced in the overall dissociation rate. However, the model assumes a two-photon dissociation, and therefore any three-photon dissociation pathways are excluded. The full simulation model, **Section 2.2**, accounts for all cross-talk from various stimulation sources. As before, the simulations assume an initial Boltzmann distribution of the ground vibronic state. Similar to the simple model, the full-simulation model cannot account for three-photon dissociation. Full-simulations require large computing resources and any three-photon pathways create too large problem sizes. The stochastic model, **Equation 2.27**, uses randomness to imitate the pathway of a molecule. Averaging over many possible pathways gives an estimation of the final rate. While this method cannot be put in an optimized, the method can demonstrate the affect if multi-photon pathways. The included electronic states where chosen to include all possible states that would be populated based on the theoretical PES curves and the expected laser frequency range. The included transition pathways are:

1. $1^1\Sigma, v = 0 - 7 \leftrightarrow 1^1\Sigma, v' = 0 - 7$

2. $1^1\Sigma, v = 0 - 7 \leftrightarrow 2^1\Sigma, v' = 0 - 7$

3. $2^1\Sigma, v = 0 - 7 \leftrightarrow 2^1\Sigma, v' = 0 - 7$

The included dissociation pathways are:

1. $1^1\Sigma, v = 0 - 7 \rightarrow 3^1\Sigma$

2. $1^1\Sigma, v = 0 - 7 \rightarrow 1^1\Pi$

3. $1^1\Sigma, v = 0 - 7 \rightarrow 2^1\Pi$

4. $2^1\Sigma, v = 0 - 7 \rightarrow 3^1\Sigma$

5. $2^1\Sigma, v = 0 - 7 \rightarrow 1^1\Pi$

6. $2^1\Sigma, v = 0 - 7 \rightarrow 2^1\Pi$

Based on previous results, the transitions for $1^1\Sigma \rightarrow 2^1\Sigma$ occur from v=0 to v'=0-4 for both CaH$^+$ and CaD$^+$. However, dissociation from the $1^1\Sigma$ state to the $1^1\Pi$ state occurs at v=5+, which means more the simulation model must include more than four vibrational states per each electronic state. As a compromise between computational resources and sufficient enough states, seven vibrational states was arbitrarily chosen. On the flip side, the simple/full models assume a two-photon dissociation, and therefore, cannot account for the $1^1\Sigma v = 0 \rightarrow 2^1\Sigma v = 0 - 4 \rightarrow 1^1\Sigma v = 5+ \rightarrow 1^1\Pi$ dissociation pathway.

Optimizations implemented both models to obtain frequency shifts for all three dissociation states. A shift in the total energy of the PES curve would modify the relative distance between the state and a transition state, which in turn, would change the relative dissociation strength. The shape of the dissociation state was assumed to remain constant, which an absolute shift parameter, in cm^{-1} was applied to the PES curve. All dissociation cross-sections are calculated through BCONT [116–118]. The previous physical constants, such as transition frequency and dipole moment, are excluded from these optimizations. Instead, the optimized constants from **Section 4** are assumed to be correct as they do not depend on the dissociation pathway. To ensure that the transition strength is the only factor affecting the optimizations, only the peak tops were included in the calculations. The optimizations minimize the χ^2 difference between the theoretical spectrum and the experimental spectrum. To speed-up all optimizations, the theoretical shifts were first optimized using **Equation 2.41** to produce initial guesses. Then, the full simulation model, **Section 2.2**, used the initial state to produce a full optimization. For a final confirmation, the optimized constants from CaH$^+$ were used to produce a CaD$^+$ spectrum which is compared to the results from **Section 3**.

5.2.2 Results and Discussion

Figure 5.5 top demonstrates a CaH^+ $1^1\Sigma \rightarrow 2^1\Sigma$ spectrum produced from using ab initio parameters with the simple model, the full simulation model and the stochastic model. All three models generates contrasting peak heights compared to the instantaneous dissociation analytical model [158]. In addition, the theoretical peak maximums are clearly left shifted from the experimental peak maximums, which is directly related to the dissociation cross section. This discrepancy directly originates from dissociation affect, which is seen in the difference between the two analytical models, **Figure 2.6**. The dissociation rate is not instantaneous compared to the transition rate, which modifies the peak maximum and the tail-end behavior.
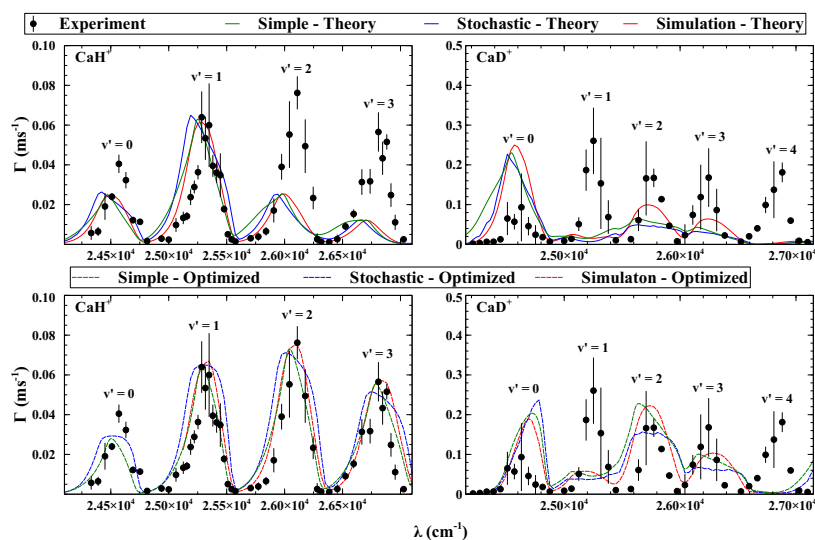
Figure 5.5: The full spectrum for CaH^+ from the full simulation model and simple model. The key lists the model and the source of the parameters. Optimization parameters are listed in **Table 5.6**.

All three models produce similar relative peak heights but different peak maximums from the same ab initio parameters, **Figure 5.5 top**. The inconsequential differences in relative peak height between the multi-photon spectrum (stochastic) and the two-photon spectrum (simulations) suggest that the three-photon pathway is irrelevant. Analyzing the rates, a molecule in the $2^1\Sigma$ state is more likely to dissociate or laser-stimulated emit to

$1^1\Sigma v = 0$, rather than spontaneously emit to $1^1\Sigma v = 5+$. This means the two-photon simulation model still produces accurate and efficient results. As expected, the shape of the simple model diverges from the expected shape of each peak from simulations. This difference demonstrates the limitations of the simple model, which can only estimate the relative peak height and not any rotational distribution. All three models produce slight variations in the frequency of each peak maximum. As the exact vibronic frequency was found in **Section 4**, this was considered an inconsequential inconsistency.

The simple model is the only process designed for optimizations. The full simulation is too computational resource heavy and the stochastic model does not produce consistent result. Therefore the optimizations were done with the simple model. The results of this quick optimizations are shown in **Table 5.6**. The shifts in this table are listed as $TheoryPES + Shift = OptimizedPES$. Since the simple model cannot account for the three-photon pathway, the optimizations cannot estimate any shift on the $1^1\Pi$ state. The $2^1\Pi$ state and $3^1\Sigma$ are still valid as its optimization parameter is within the 700 wavenumber shift from **Section 3**. Analyzing the dissociation cross-sections reveals that the 1000 cm^{-1} shift on the $3^1\Sigma$ state shifts the cross-section spectrum to an area of relatively large dissociation. This alters the dissociation spectrum to match the instantaneous dissociation model.

Table 5.6: The Optimized Shifts Applied to Theoretical Dissociation States in cm^{-1}

State	Shift
$1^1\Pi$	-
$2^1\Pi$	1059 ± 658
$3^1\Sigma$	248 ± 113

As a secondary verification, the optimized CaH$^+$ parameters used to produce a CaD$^+$ spectrum similar to **Section 3**. The initial theory produces infeasible results, and the

optimization does not brings out normal spectrum properties. In particular the $v' = 1$ and the $v' = 4$ transitions are missing from the spectra. The dissociation cross-sections are absolute zero for these particular vibronic transitions, which may speak towards the limitations of the BCONT program.

5.2.3   Conclusion

We have shown that an alternative theoretical model can discover a dissociation pathway when the Hamiltonian and experimental methods could not. We show that CaH^+ [1+1'] REMPD experiments dissociate through the $2^1\Pi$ and $3^1\Sigma$ states. The possible pathways for these states are $1^1\Sigma, v = 0 - 7 \rightarrow 2^1\Sigma, v' = 0 - 7 \rightarrow 2^1\Pi$ and $1^1\Sigma, v = 0 - 7 \rightarrow 2^1\Sigma, v' = 0 - 7 \rightarrow 3^1\Sigma$. Both pathways involves two-photon dissociation. These results have not actively disproved any previous peak assignments or transition frequency measurements, which indicates previous work is unaffected by the dissociation pathway.

While these results are incomplete and therefore inconclusive, the simple model makes good initial progress towards the final answer. The simple model can accurately predict relative peak heights for two-photon dissociation pathways. However, the model cannot account for the possibility of three-photon dissociation which seems prevalent in these results. In addition, the simple model does not accurately model key peak shape properties, owing to estimations made in the derivation of the model. These factors make the simple model unable for accurate results and only applicable to initial guesses.

To verify the results shown here, additional experimentation is needed. Quantum Logic Spectroscopy could eliminate the need for the dissociation pathway [35, 38, 63, 78, 79, 91, 104]. Chou et al. already used a logical Ca^+ to state-detect CaH^+ [35]. If this procedure could be modified to verify previously measured CaH^+ transition frequencies, then these dissociation results gain credibility. Rotational cooling before REMPD may also eliminate discrepancies, **Section 7.1.3**. The spectra presented here are plagued by wide peaks from rotational distributions. Eliminating these broad peaks would verify the exact transition

frequencies and authentic these results. Directly measuring the dissociation PES curves through experimentation would verify these results wholly.

CHAPTER 6

QUANTUM INFORMATION

6.1 Introduction

As quantum information processors become more complex a key challenge is the validation and verification of integrated systems. Individual gates can be well characterized by quantum process tomography (QTP) [164], randomized benchmarking (RB) [165–169], and related methods [170–175]. Although these techniques can be efficient under certain conditions [176–178], in general, QTP and RB become inefficient and impractically resource intensive, respectively, as the size of the circuit grows large. One method for testing larger devices is to compare the physical algorithmic output to the expected algorithmic output. For many algorithms, like the quantum linear system algorithm [179, 180], the ideal output may not be known and the effect of errors on the output cannot be calculated.

Fortunately there are classes of quantum circuits that can be efficiently computed, with the prime example being circuits composed of only Clifford gates, which can be simulated efficiently by the Gottesman-Knill theorem [181, 182]. The circuits can then be decorated with random Pauli errors and the output can be sampled using Monte-Carlo methods. This Monte-Carlo sampling can be extended to include Clifford errors [183] and Clifford gates conditional on measurements in a Pauli basis [184, 185]. Since the Clifford group transforms Pauli errors to Pauli errors, all of the errors can be pushed to the end of the circuit. This transformation is the basis of fault-path methods which identify the sets of errors that result in failure by following how Pauli operators propagate through the correction circuit [186]. For low-distance codes, these method are used to rigorously bound the fault-tolerant threshold of specific protocols. Exact calculations are not

practical due to the exponential possible combinations of errors and these methods rely on cutoffs that consider only a certain number of errors. This is well motivated by the reduced probability of having multiple errors and the limited distance of the codes.

Here we apply the fault-path method to algorithms made from Clifford circuits. While these algorithms provide at most only a polynomial advantage, they are ideal for testing the integration of many qubits into a quantum computer. Most quantum error correction codes expect that the errors are independent probabilistic Pauli operators. Implementing a non-fault tolerant circuit of Clifford gate and testing the output distribution relative to this model provides confidence in the accuracy of this error model for a given implementation.

In contrast to quantum error correction codes, we find that the fault-path method can efficiently calculate the exact success rate for certain tree-like quantum algorithms in polynomial time for Pauli error models. We show this can be determined from the graph structure of the circuit and discuss how the cost of exact simulation can be related to the weight of the nodes and the number of cycles in the graph. We then apply our tools to the Bernstein-Vazirani algorithm and exactly simulate the success rate for circuits containing up to 1350 qubits [187]. Finally, we apply error truncation to our method to estimate the threshold of the Steane [[7,1,3]] code with Shor ancilla [188, 189].

6.1.1 Background and Definitions: Pauli Errors and Clifford Circuits
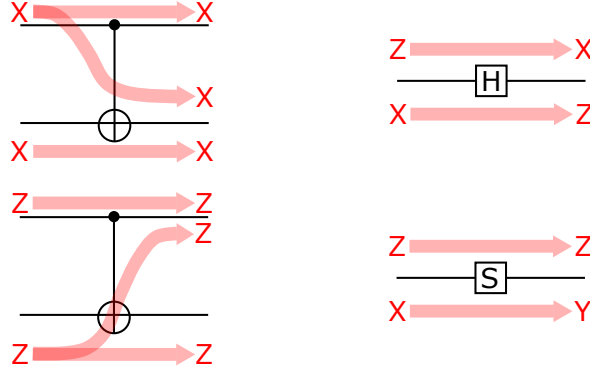
Figure 6.1: Two types of error (X and Z) propagating across a controlled-NOT, Hadamard, and Phase gates.

The Pauli operators on n qubits are composed from the tensor product of the single qubit Pauli operators X, Y, and Z, and the Identity, I. The weight of the Pauli operator is the number of non-identity elements in the tensor product. For n qubits there are 4^n Pauli operators. The Clifford group is defined as unitary operations that transform Pauli operators to Pauli operators. The Clifford group can be generated from one and two qubit operations: *CNOT*, H, and S. For additional information, we refer the readers to any quantum computation textbook [190].

A Pauli error channel, $\mathcal{E}$ is equivalent to a random application of a set of Pauli operators. The action of the channel is defined by Kraus operators $\mathcal{E}(\rho) = \sum_j \mathbf{A}_j \rho \mathbf{A}_j^\dagger$, where $\mathbf{A}_j = \sqrt{p_j}\mathbf{P}_j$, $\mathbf{P}_j$ is a Pauli operator, and p_j is the probability that the operator is applied. We define the number of non-zero p_j as the rank of the channel, r. Clifford operators map Pauli error channels to Pauli error channels and although the weight of the Pauli operators can be changed the rank of the channel is preserved. Pauli error channels compose with other Pauli error channels to create new Pauli error channels with a rank that is bound by the product of the ranks of the channel or the maximum rank allowed by the system.

A standard model for errors is that each gate g acting on k qubits has an associated Pauli error channel $\mathcal{E}_g$ composed of Pauli operators that also act on the same k qubits, limiting the rank to $r_g \leq 4^k$. Assuming a circuit constructed from one and two-qubit Clifford operators, the maximum rank for each error channel is 16. It is very convenient to push all of the error operators to the end of the circuit. The other Clifford operations transform the error channel to $\mathcal{E}'_g$ but preserve the rank. If there are G gates, the Pauli error channel of the entire circuit can be composed from G Pauli error channels of low rank. The cost of this composition determines whether we can efficiently determine the probability distribution of outcomes and the success rate.

It is convenient to introduce the notion of an error vector, $\boldsymbol{\Psi}$, which contains the 4^k probabilities for a state to a specific Pauli error. Each Clifford gate, g, first transforms $\boldsymbol{\Psi}$ by mapping one Pauli error to another Pauli error. This can be represented by a $4^k \times 4^k$ transformation matrix $\mathbf{T}_g$, with only 4^k non-zero entries of 1 and preserving the error-free entry of the error vector. Then, the associated error channel $\mathcal{E}_g$ is applied, which in this representation is a $4^k \times 4^k$ error matrix $\mathbf{E}_g$ which has r_g distinct coefficients and $4^k r_g$ non-zero entries. The transformation matrices for H, S, and *CNOT* are given graphically in **Figure 6.1**, alongside the full rank single qubit error matrix. To calculate the full error vector of k qubits with G gates, we can apply the formula:

$$\boldsymbol{\Psi}_{final} = (\prod_{i=1}^{G} \mathbf{E}_i \mathbf{T}_i) \boldsymbol{\Psi}_{initial}. \tag{6.1}$$

This calculation is impractical in general, but can be used for small problem sizes.

We often combine the error matrix and transformation matrix into a single bi-stochastic matrix: $\mathbf{M}_i = \mathbf{E}_i \mathbf{T}_i$. As per **Figure 6.1**, H changes X errors to Z errors, Pauli operations such as Z do not change Pauli errors. Assuming the same error matrices for the two gates, we present two example bi-stochastic matrices:

$$\mathbf{M}_Z = \begin{bmatrix} p_I & p_X & p_Y & p_Z \\ p_X & p_I & p_Z & p_Y \\ p_Y & p_Z & p_I & p_X \\ p_Z & p_Y & p_X & p_I \end{bmatrix} , \; \mathbf{M}_H = \begin{bmatrix} p_I & p_Z & p_Y & p_X \\ p_X & p_Y & p_Z & p_I \\ p_Y & p_X & p_I & p_Z \\ p_Z & p_I & p_X & p_Y \end{bmatrix}$$

Let us examine two simple scenarios. In the first example, there are G qubits each acted on by a single 1-qubit gate, and each gate has a distinct rank four error channel. In this case, every $\mathcal{E}_g$ is equivalent to $\mathcal{E}'_g$, since there are no sequential Clifford gates. Finding the complete Pauli error channel requires multiplying all combinations of error probabilities to yield 4^G coefficients, which is inefficient in the circuit size. If we define the success probability as the probability of no qubits having error, we only need to consider the I component of each error channel yielding a success rate, $P_{I,G} = \prod_g p_{I,g}$, which can be efficiently calculated with G multiplications.

In a second example, there is one qubit with G 1-qubit gates each with a distinct rank four error channel. Now the gates are in sequence and the channels are transformed by the gates to $\mathcal{E}'_g$. Unlike the previous example, the final rank of the error channel is bound to be 4. We can compose two error channels by multiplying the 4 coefficients of each channel to yield only 4 coefficients. As a result the complete error distribution can be found efficiently with only $16G$ multiplications of error probabilities after the error transformation. Generalizing to k qubits, we require $16^k G$ multiplications, which is efficient in G but inefficient in k. Formally, we calculate the bi-stochastic matrix for a sub circuit F.

$$\mathbf{M}_F = \prod_{g \in F} \mathbf{M}_g \tag{6.2}$$

The crux of our method for calculating success rates is to cut every circuit into these two examples by identifying circuit components whose failure rate can be calculated independently and by limiting the size of the dependent block to a small numbers of

94

qubits. If the circuit naturally has a small dependency, we can calculate the success rate exactly, otherwise we use approximations to truncate the dependency.

6.2 Fault-Path Tracer
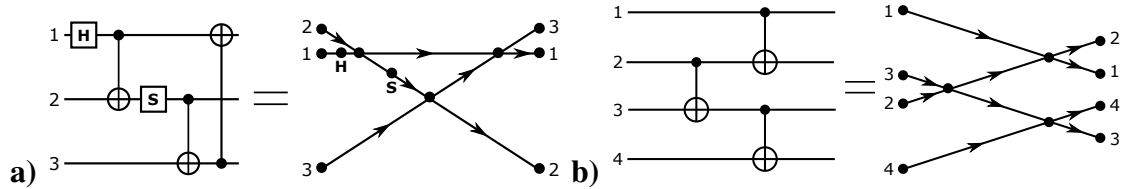
Figure 6.2: Demonstration of a standard circuit converted to a directed graph which contains: **a** a undirected cycle and **b** a tree-like pattern. Intersecting lines represent multi-qubit gates.

We start with a circuit of G one and two-qubit gates. We convert the circuit to a directed graph where each gate is a node with incoming edges and outgoing edges corresponding to the qubits acted on by the gate. A fault path is defined by starting at an output qubit of the circuit and then walking the graph backwards to the input qubits. The fault-path shows where errors can arise that may propagate to the final qubit output. We refer to our methods for using fault-paths to then calculate or estimate success rates as the Fault-Path Tracing (FPT) method.

Two circuits and their related graphs are shown in **Figure 6.2**. The fault-path, $fp(q)$, finds all gates where errors can be introduced to the final state of qubit q (**Algorithm 1**). To calculate the error on that qubit for circuits composed of one and two-qubit gates, we break the fault-path into sub-paths of single qubit gates connected by two-qubit gates. We can calculate the error matrix for the single-qubit gate paths efficiently as described earlier. Starting from the input nodes, we then combined these single qubit error matrices with the two-qubit error transformation matrix and gate error to generate a two-qubit error matrix on the outputs. We can then ask if the output qubit paths are in the fault path. If the answer is yes, we need to keep the two-qubit error matrix. If not, we can reduce the two-qubit error

matrix to a one-qubit error matrix by tracing over the error state of the output qubit that is off the path. Either way, we then continue along the graph towards the output qubit.

For tree-like graphs and a single fault path, we can always reduce to a single qubit error matrix after each gate. This simplification allows us to work with only single qubit error matrices except for at the two-qubit nodes where we need to calculate a two-qubit error matrix before reducing it. The result is an efficient method for calculating error states at single qubits without knowledge of the error states on other qubits (**Algorithm 2**). For undirected cycle on the underlying graph, the error matrices can continue to grow. In **Figure 6.2**a, we see that a two-qubit error matrix must be kept for a few nodes and that a three-qubit error matrix must be briefly constructed for the triangle-shaped loop. If we treat the undirected cycle as a single three-qubit Clifford gate, the graph becomes tree-like again but a three-qubit error matrix still must be generated. The number of qubits that input to the undirected cycle determines the size of error matrix that must be constructed.

For any algorithm, a lower-bound on the success probability can be determined by calculating the independent error probability of each output qubit having no error and then multiplying the probabilities. This will overestimate the error since output errors on qubits will be correlated. In order to calculate the correlations, we need to look at the overlap between fault-paths that affect our output of interest.

Our procedure for calculating error rates from overlapping fault paths is described in **Algorithm 3**. The four cases mentioned are: error on no branch, error on control branch, error on target branch, and error on both branches. We often assume that the output qubit is measured in a specific basis X or Z. As a result, the fault path is simplified and reduces the Pauli errors to simply an error (X or Y for Z measurements) or no error (I and Z for Z measurements). We refer to this fault-path as $fp(q; X)$. By breaking the overlapping fault-points into non-overlapping fault points, we can exactly calculate both the correlation and we can handle each subgraph exactly. However, in the case that there is a undirected cycle that has more than 2 qubit inputs or 2 qubit outputs, this method cannot no longer

exactly calculate the success rate. Instead, a lower bound is used to estimate the rate for each subgraph.

Algorithm 1 Finding Single Fault-Path

1: **function** FINDFP($\mathbb{C}, q, \mathbb{E}$)   ▷ The fault-path from qubit q with error e on circuit $\mathbb{C}$.
2:      $g \leftarrow \mathbb{C}[q][-1]$
3:      $fp(q; \mathbb{E}) \leftarrow (g, \mathbb{E})$ ▷ If no $\mathbb{E}$ specified, then two points (X and Z)
4:      $\mathbb{S} \leftarrow ErrorRules(g, \mathbb{E})$ ▷ Reverse error propagation rules to find previous error sources
5:      **for** $s \in \mathbb{S}$ **do**
6:          $g \leftarrow s[0]$
7:          $q \leftarrow s[1]$
8:          $\mathbb{E} \leftarrow s[2]$
9:          $fp(q; \mathbb{E}) + = FindFP(g, q, \mathbb{E})$
10:      **end for**
11:      **return** $fp(q; \mathbb{E})$ ▷ The fault-path containing a list of potential fault-points
12: **end function**

Algorithm 2 Probability of Success for Single Tree-Like Fault-Path

---

1: **function** SINGLESUCCESS($fp, \mathbb{M}$)   ▷ The error on path fp with error rates $\mathbb{M}$
Ensure: fp well-ordered   ▷ Based on order in $\mathbb{C}$, order fault-points
2:      $\Psi \leftarrow [1, 0, 0, 0]$
3:      **for** $g \in fp$ **do**
4:          $M \leftarrow \mathbb{M}[g]$
5:          **if** $g.size > 1$ **then**
6:              $M \leftarrow Condense(M)$ ▷ If the gate is a two-qubit gate, condense to a 4x4 matrix
7:          **end if**
8:          $\Psi \leftarrow M * \Psi$ ▷ Apply **Equation 6.2**
9:      **end for**
10:      $\bar{\varepsilon} \leftarrow \Psi[0]$.
11:      **return** $\bar{\varepsilon}$ ▷ Probability of the qubit yielding the correct output
12: **end function**

Algorithm 3 Approximate Probability of Success for Multiple Fault-Paths
---
1: **function** FINDRATE($\mathbb{F}$) ▷ Find probability of all fault-paths $\mathbb{F}$ having no error or error
2:      $\bar{\varepsilon} \leftarrow 1.0$
3:      $\varepsilon \leftarrow 1.0$
4:      $\mathbb{G} \leftarrow Split(\mathbb{F})$ ▷ Split paths into independent groups
5:      **for** $g \in \mathbb{G}$ **do**
6:          $Rates \leftarrow []$
7:          $\mathbb{O} \leftarrow g \cap g$ ▷ fault-points common to all fault-paths
8:          $\mathbb{B} \leftarrow FindBranches$ ▷ Find the n independent branches
9:          $\mathbf{\Psi} \leftarrow SingleSuccess(\mathbb{O})$ ▷ Find the rates of all 2^n possible cases
10:          **if** $Independent(\mathbb{B})$ **then**   ▷ Test independence in branches
11:              **for** $b \in \mathbb{B}$ **do**
12:                 $Rates \leftarrow FindRate(b)$
13:              **end for**[
14:          **else**   ▷ This is the case of a cycle
15:              $Rates \leftarrow \prod_i \epsilon_i$ ▷ Lower Bound Estimation]
16:          **end if**
17:          $M \leftarrow BuildMatrix(Rates)$
18:          $\mathbf{\Psi} \leftarrow M * \mathbf{\Psi}$ ▷ Apply **Equation 6.2**
19:          $\bar{\varepsilon} \leftarrow \bar{\varepsilon} * \mathbf{\Psi}[0]$
20:          $\varepsilon \leftarrow \varepsilon * \mathbf{\Psi}[0]$
21:      **end for**
22:      **return** $(\bar{\varepsilon}, \varepsilon)$ ▷ P(all have error), P(none have error)
23: **end function**

6.2.1 General Circuit

Fault-path:

M, X | H, X | $CNOT_C, Z$ | P_1, Z | Z, Z | P_2, Z
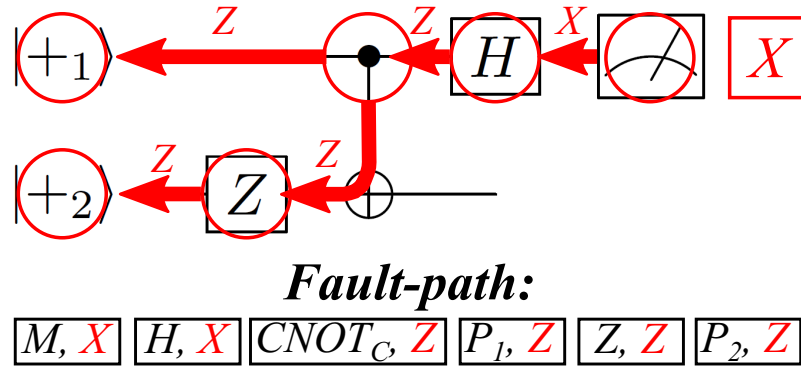
Figure 6.3: The Bernstein-Vazirani Algorithm for one bit, with a Hamming weight of one. A possible X error on the first qubit could have resulted from various previous gates, found through backwards error propagation rules. The controlled-X gate leads to a branch in the fault-path. Each possible error source is a fault-point and has an associated error type that affects the output.
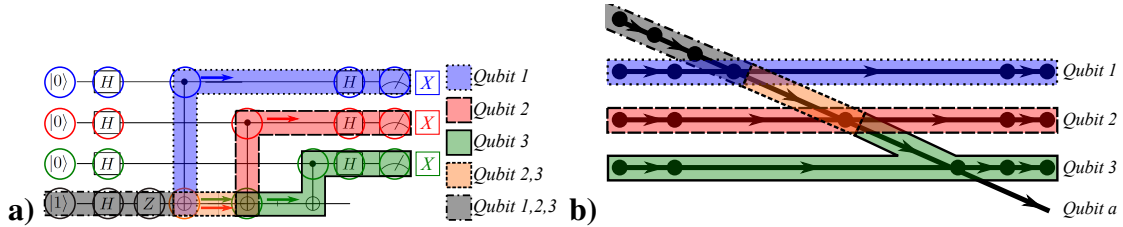
Figure 6.4: **a** The Bernstein-Vazirani Algorithm for three bits, with a Hamming weight of three, showing how errors spread in the circuit. Only part of the fault-paths are highlighted to emphasize the tree-pattern formed from fault-paths. **b** The same circuit represented as a directed-graph with the full fault-path labeled.

The Bernstein-Vazirani Algorithm finds the value of an unknown string, s, composed of m unknown bits [187]. It requires the oracle operation $U_{BV}(s)$ that changes the ouput qubit state y based on the data qubits x and the function $f_s(x)$:

$$f_s(x) = \vec{x} \cdot \vec{s} = (x_0 s_0 + x_1 s_1 + \cdots + x_{n-1} s_{n-1}) \mod 2$$

$$U_{BV}(s) |x\rangle |y\rangle = |x\rangle |y \oplus f_s(x)\rangle .$$

Like all oracle based algorithms, the construction of the oracle is not specified. We choose the simplest oracle that consists of CNOTs between data qubits where the value of s is 1 and the output qubit. The number of gates depends on the Hamming weight of s and, to determine worst case probabilities, we assume that s has maximum Hamming weight.

Classically, one sends in data strings with a single bit flipped and determines s in m steps. Quantum mechanically, by using Hadamard transformations and a Pauli Z, one can obtain s in a single oracle call. For this procedure, success is having no bit flips on the data qubits. The output qubit is free to have any error.

Each of the data qubits is measured in the Z basis, implying that only X/Y errors are malignant. $fp_Z(q)$ for each qubit is found using **Algorithm 1**. **Figure 6.3** shows the fault-path branching due to the multi-qubit gate. By mapping the overlap between all of the fault-paths, a tree-structure emerges. To emphasize the tree-structure in **Figure 6.4**a, some fault-points were deliberately left unhighlighted. This tree-structure meets the main assumption that none of the branches cross each other. To find the success rate for this 3-qubit circuit, each highlighted portion is analyzed separately. **Algorithm 2** gives the probability error state of the Q123 region, which represents the fault-points that affect all three data qubits. By tensoring this state with a unit vector, the first CNOT error matrix can be applied to this state to produce a 16-dimension vector. This larger vector can be divided into four distinct cases: no errors ($\bar{\epsilon}$), error occurring on control branch (ϵ_c), error occurring on target branch (ϵ_t), and error occurring on both branches (ϵ_{ct}):

$$\begin{bmatrix} \bar{\epsilon} \\ \epsilon_c \\ \epsilon_t \\ \epsilon_{ct} \end{bmatrix}_{Q123} \tag{6.3}$$

After the overlap, each branch is calculated recursively. Since the control branch only contains one fault-path, the probability of no error, $\bar{\epsilon}_{Q1}$, can be found using **Algorithm 1**.

100

The target branch contains two fault-paths which have a second overlap region and two additional branches. Similar to the Q123 region, a four-case vector can be found for the Q23 region:

$$
\begin{bmatrix} \bar{\epsilon} \\ \epsilon_c \\ \epsilon_t \\ \epsilon_{ct} \end{bmatrix}_{Q23}
\tag{6.4}
$$

Similar to before, after the Q23 overlap, the control and target branches have one fault-path each. The probability of no error, $\bar{\epsilon}_{Q2}$ and $\bar{\epsilon}_{Q3}$ respectively, is found using **Algorithm 1**. All of these error rates can be combined using **Equation 6.5** to find the success rate. By dividing the circuit into parts depending on the nodes, the matrices do not change size regardless of the number of qubits.

$$
\begin{bmatrix} \bar{\epsilon} & \epsilon_c & \epsilon_t & \epsilon_{ct} \\ \epsilon_c & \bar{\epsilon} & \epsilon_{ct} & \epsilon_t \\ \epsilon_t & \epsilon_{ct} & \bar{\epsilon} & \epsilon_c \\ \epsilon_{ct} & \epsilon_t & \epsilon_c & \bar{\epsilon} \end{bmatrix}_{Q2,Q3}
\begin{bmatrix} \bar{\epsilon} \\ \epsilon_c \\ \epsilon_t \\ \epsilon_{ct} \end{bmatrix}_{Q23}
=
\begin{bmatrix} \bar{\epsilon} \\ \\ \\ \epsilon \end{bmatrix}_{Q2,Q3,Q23}
$$

$$
\begin{bmatrix} \bar{\epsilon} & \epsilon_c & \epsilon_t & \epsilon_{ct} \\ \epsilon_c & \bar{\epsilon} & \epsilon_{ct} & \epsilon_t \\ \epsilon_t & \epsilon_{ct} & \bar{\epsilon} & \epsilon_c \\ \epsilon_{ct} & \epsilon_t & \epsilon_c & \bar{\epsilon} \end{bmatrix}_{(Q1),(Q2,Q3,Q23)}
\begin{bmatrix} \bar{\epsilon} \\ \epsilon_c \\ \epsilon_t \\ \epsilon_{ct} \end{bmatrix}_{Q123}
=
\begin{bmatrix} Success \\ \\ \\ Error \end{bmatrix}
\tag{6.5}
$$

As with the lowerbound method, various other sub-sets of the Pauli Channel can be found by exchanging ϵs and $\bar{\epsilon}$s. For example, consider the scenario that the first and third qubit have no error, but the second qubit does have error. To solve for this probability only a minor exchanging of the error rates for the second qubit, $\bar{\epsilon}_r$ and ϵ_r, are necessary:

$$
\begin{bmatrix}
\bar{\epsilon} & \epsilon_c & \epsilon_t & \epsilon_{ct} \\
\epsilon_c & \bar{\epsilon} & \epsilon_{ct} & \epsilon_t \\
\epsilon_t & \epsilon_{ct} & \bar{\epsilon} & \epsilon_c \\
\epsilon_{ct} & \epsilon_t & \epsilon_c & \bar{\epsilon}
\end{bmatrix}_{Q2,Q3}
\rightarrow
\begin{bmatrix}
\epsilon_c & \bar{\epsilon} & \epsilon_{ct} & \epsilon_t \\
\bar{\epsilon} & \epsilon_c & \epsilon_t & \epsilon_{ct} \\
\epsilon_{ct} & \epsilon_t & \epsilon_c & \bar{\epsilon} \\
\epsilon_t & \epsilon_{ct} & \bar{\epsilon} & \epsilon_c
\end{bmatrix}_{Q2,Q3}
$$

6.2.2 Limitations

As the FPT must make many assumptions to efficiently iterate through the circuit, there are many known limitations. Firstly for **Figure 6.5 a**, if A does not equal B, which is not a no-error state, then there is no simple equivalent of C. Solution: FPT always assumes ideal/perfect initial states. Secondly, in **Figure 6.5 a**, if E = Hadamard, then the FPT assumed equivalent is wrong since Hadamard gates are not commutative. Solution: FPT assumes there are no Hadamard gates in the circuit. Thirdly, for **Figure 6.5 b**, the controlled not gates must be converted to single qubit equivalents, of which there are none. Solution: FPT assumes no cycles present in graph. Fourthly, in **Figure 6.5 b**, if F = Hadamard, then the FPT assumed equivalent is wrong since Hadamard gates are not commutative. Solution: FPT assumes there are no Hadamard gates in the circuit. Lastly, for **Figure 6.5 b**, if F is not a Hadamard, then the FPT conversion is wrong since cycle present. Solution: FPT assumes no cycles present in graph.
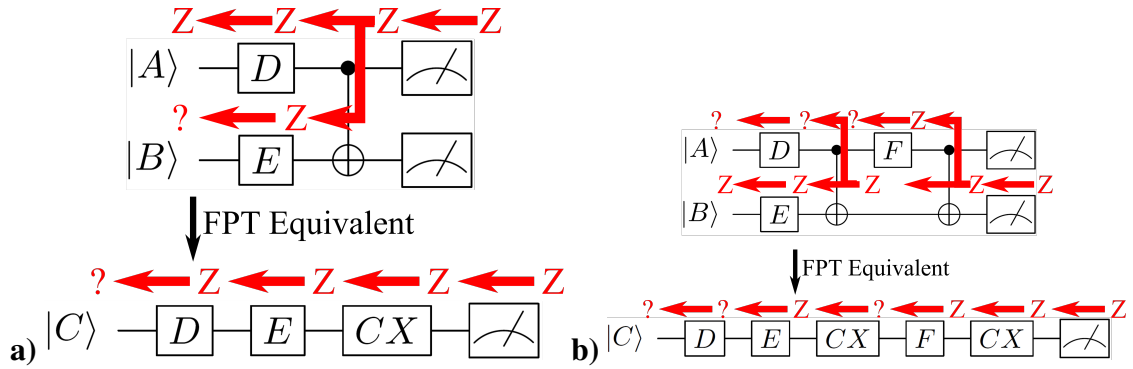
Figure 6.5: Examples circuit to explain where the basic FPT assumptions fail. The error path is shown in red for both circuits. The question marks represent error that changes depending on the previous gate (i.e. Hadamard gates).

6.3 Fault-Path Tracer for Quantum Error Correcting Codes

The FPT method was previously used to evaluate syndrome extraction methods for the Steane code on a model ion trap architecture [189]. Here we describe the details of the process for a specific syndrome extraction method assuming a quantum machine without geometry, i.e. two-qubit gates are possible between any qubits. The presented FPT method for quantum error correction is an extension and generalization of the previous method described in Ref. [191] and used in Ref. [189].

For distance-3 codes, all single qubits errors can be decoded. For the Steane Code, X and Z errors are decoded independently, allowing for some two-qubit errors to be fixed. This means the success rate is the probability of all data qubits having less than two errors of the same tpye on two different qubits after the correction is applied. Unlike before, this rate allows multiple correlated output errors, which renders the previous methods inefficient. To reduce the size of the circuit, every syndrome is assumed to be independent, which means they can be analyzed separately. The syndrome is divided into three sub-groups: detectable fault-paths, S_d, undetectable fault-paths, S_u, and ancilla fault-paths, S_a. Detectable fault-paths are sub-groups of data fault-paths where errors will affect the ancilla measurement. In contrast, undetectable fault-paths are those fault-points were the errors will not affect

the ancilla measurement. Finally, ancilla fault-paths are the complete fault-paths from ancilla qubits. For our FPT method, we assume these three categories share no fault-points in common. This implies that a single error in any of the three sub-groups will result in a single data-qubit error. Since each FPT calculation is dependent on the individual gate errors, the fault path only produces pseudothreshold curve, not a real threshold point. To find the real threshold, the circuit is encoded to a k-level and the error matrices are recursively modified to reflect the $k - 1$ error rate. The method is outlined in Construction **Algorithm 4**.

The exact procedure to find ε_d, ε_u, and ε_a varies with each QECC. Here we describe how it is applied to Steane QECC with Shor ancilla and the decoding scheme proposed by Divincenzo and Aliferis to account for the overlap between S_d and S_a in each syndrome [192]. An example sysdrome measurement circuit is shown in **Figure 6.6**. This QECC measures each syndrome (X and Z) three times, and employs a majority vote to ensure accurate corrections. Since each syndrome is independent, calculations can be reduced by assuming $\varepsilon_{d1} = \varepsilon_{d2} = \varepsilon_{d3}$. For each syndrome, the fault-paths for the DiVincenzo and Aliferis correction are found first. Based on the probability that an error will spread to both the ancilla measurements and the data measurements, additional gates are added to the data qubits to represent the probability of a correction occurring. For the case of the Steane-Shor QECC, the detectable and ancilla groups have a number of shared fault-points; therefore, the overlap between these groups is treated as a forth group, S_b. The data qubit fault-paths are divided among undetectable and detectable while the remaining ancilla fault-paths remain intact. Construction **Algorithm 3** is used to find ε_d, ε_u, ε_b, and ε_a. For this particular QECC, a single error in any of the four categories will render the entire syndrome faulty. Using the probability of a single X and Z syndrome measuring fault, the probability of the three syndromes giving the right correction is easy to calculate.

In general, this method is accurate when there is very little or no overlap between S_d and S_a. In addition, many QECCs require decoding schemes to reduce the number of relevant

---

Algorithm 4 Approximate probability of success for multiple fault-paths

---
1: **function** FINDRATEQECC($\mathbb{CC}, \mathbb{EC}, k$) $\triangleright$ Find rate from code style $\mathbb{CC}$, error correcting style $\mathbb{C}$, and current level k
2: $M \leftarrow FindRateQECC(\mathbb{CC}, \mathbb{EC}, k-1)$ $\triangleright$ Populate lower level matrix dictionary
3: $\mathbb{C} \leftarrow Circuit(\mathbb{CC}, \mathbb{EC})$
4: **for** $l \in [X, Z]$ **do**
5:   $D \leftarrow FindFP(\mathbb{C}, q, \mathbb{E}) \forall \mathbb{C}.dataQubits$
6:   **for** $path \in D$ **do**
7:    **for** $point \in path$ **do** $\triangleright$ Separate path into S_d and S_u
8:     **if** $point.data == True$ **then**
9:      $S_d += point$ [
10:     **else**
11:      $S_u += point$]
12:     **end if**
13:    **end for**
14:   **end for**
15:   $A \leftarrow FindFP(\mathbb{C}, q, \mathbb{E}) \forall \mathbb{C}.ancillaQubits$
16:   **for** $path \in A$ **do**
17:    **for** $point \in path$ **do** $\triangleright$ Separate path into S_a and benign fault-points
18:     **if** $point.benign == False$ **then**
19:      $S_a += point$
20:     **end if**
21:    **end for**
22:   **end for**
23:   $\varepsilon_d \leftarrow FindRate(S_d)$
24:   $\varepsilon_u \leftarrow FindRate(S_u)$
25:   $\varepsilon_a \leftarrow FindRate(S_a)$
26:   $\overline{\varepsilon_{error\_type}} \leftarrow \overline{\varepsilon_d \varepsilon_u \varepsilon_a} + \varepsilon_d \overline{\varepsilon_u \varepsilon_a} + \overline{\varepsilon_d} \varepsilon_u \overline{\varepsilon_a} + \overline{\varepsilon_d \varepsilon_u} \varepsilon_a$
27: **end for**
28: $(1 - \varepsilon) \leftarrow (1 - \varepsilon_X)(1 - \varepsilon_Z)$
29: **return** $(1 - \varepsilon)$ $\triangleright$ P(error correction success)
30: **end function**

---

qubits and account for any classical computations. Without these decoding schemes, the number of possible outcomes quickly renders the FPT method ill-suited. In general, the FPT method cannot simultaneously calculate multiple parts of the Pauli channel. To find the full Pauli channel exactly requires $G\ 4^m \times 4^m$ matrices where G is the number of gates and m is the number of data and ancilla qubits. These matrices would act on a size 4^m probability error state vector. Any correction steps would also need to be represented as $4^m \times 4^m$ matrices, as no classical corrections can be applied in this context.
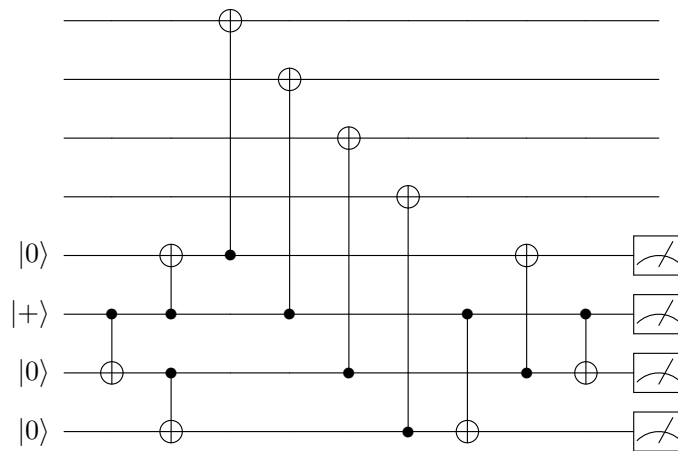
Figure 6.6: A single syndrome measurement for the Steane-Shor QEC with DiVincenzo decoding. The method generates a undirected cycle in the circuit diagram precluding the use of our methods for tree-like circuits.

6.4   Bernstein-Vazirani Algorithm

All matrix and vector math is done using the NumPy python package [193]. For testing purposes, we choose to model error as Markovian-depolarizing noise. Depolarizing noise represents the error rate of all gates as ϵ. Since single-qubit gates have three types of error (X, Y, and Z), each type of error has an equal chance of occurring ($\frac{\epsilon}{3}$). For two-qubit gates, this fraction changes to $\frac{\epsilon}{15}$ to represent the additional types of error (XX, YZ, etc.). When comparing the fault-path method to Monte Carlo simulations, there are two main

parameters: accuracy of the success rate and computation speed. We tested both of these parameters against two circuit variables: the gate error rate, ϵ, and the size of the unknown string, s. The Monte Carlo results consisted of many trials.

6.4.1 Accuracy
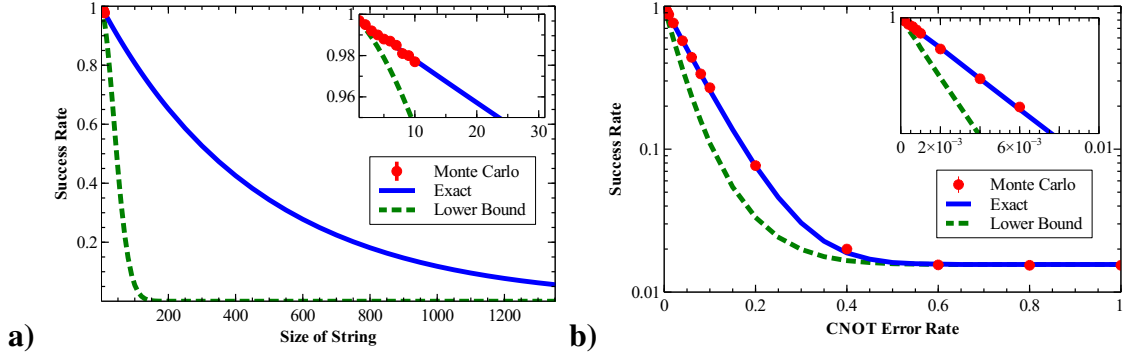
Figure 6.7: **a** Comparison of exact and approximate FPT methods to Monte Carlo for the Bernstein-Vazirani algorithm with CNOT error rate $= 1.0 \times 10^{-3}$ and Hamming weight equal to the string size. **b** Here we vary the error rate for a string size and Hamming weight equal to 6.

As seen in **Figure 6.7**, the success rate behavior is reasonable since it decreases for higher error rates and increases for smaller circuit sizes. Each (ϵ,s) combination was simulated $\frac{10 \cdot s}{\epsilon}$ times with a minimum of 100,000, and each combination is an average of least three trials. The exact FPT method accurately predicts all Monte Carlo results, both when the size of the string and the error rate are varied, **Figure 6.7**. In contrast, the lowerbound FPT method has regions of (ϵ,s) that appear more accurate. As the string size increases, the lowerbound method loses accuracy at an exponential rate. Comparatively, at error rates less than 0.002 and higher than 0.4, the percent error is less than 5%, while the region in between has percent error as high as 60%. In general, the lowerbound method reasonable predict the correct success rate with a percent error less than 5% at $s \cdot \epsilon < 0.01$.

6.4.2 Timings
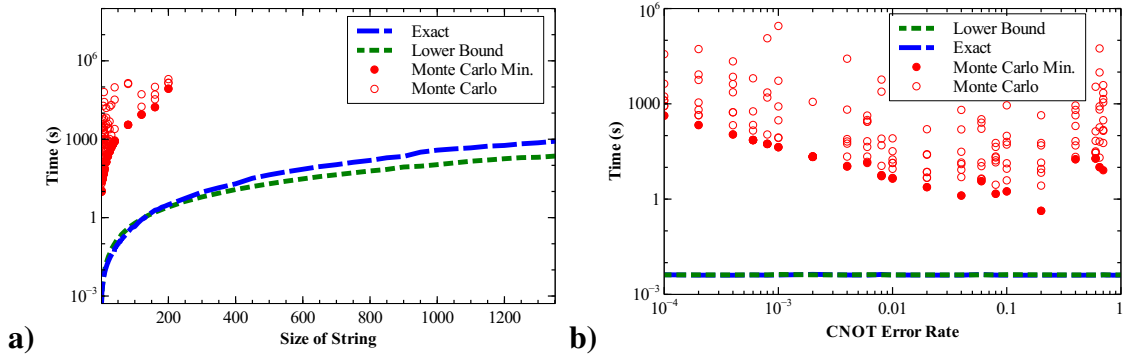
Figure 6.8: **a** CNOT error rate $= 1.0 \times 10^{-3}$, Hamming weight = size of string **b** String Size = 6, Hamming weight = 6

Both the exact FPT method and the lowerbound FPT method consistently take less time as expected from an analytical method, **Figure 6.8**. To measure the Monte Carlo minimum wall time necessary for each combination, each (ϵ, s) combination was simulated until the success rate converged to the answer provided by the exact FPT. The convergence criteria was set to a percent error of less than 1%. Each (ϵ, s) combination was tested with at least five trials for precision. As the fault-path method for tree-circuits is fully independent of error rate, the timing does not change based on error rate, unlike Monte Carlo methods. The minimum trial time for each point reveals a polynomial clear behavior, **Figure 6.8**.As the string size increases, the Monte Carlo minimum time behavior increases as a third degree polynomial, which reflects the linear increase in the number of simulations and the quadratic increase in time per simulation. As the error rate moves away from 0.5% the minimum time increases, reflective of the larger phase space. As the string size increases, the exact method scales as a fifth degree polynomial while the lowerbound method scales forth degree polynomial. The exact scaling of each FPT method is dependent on the number of fault-points and the size of the overlap and therefore changes depending on the circuit. As the Monte Carlo method cannot analysis error rates in the $10^{-6} - 10^{-4}$ range, the FPT is exceedingly useful for these cases.

6.4.3   Resource Usage
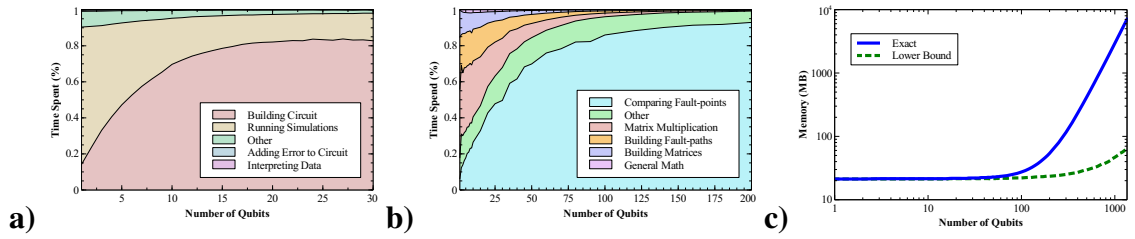
Figure 6.9: The distribution of computation time for **a** Monte Carlo simulations **b** versus Fault-Path Tracer where CNOT error rate $= 1.0 \times 10^{-3}$, Hamming weight = number of qubits. **c** The amount of memory used based on number of qubits for both methods.

The Monte Carlo method applies time to building circuit copies for each iteration, **Figure 6.9 a**. The entire Monte Carlo procedure can be divide into five main steps: circuit creation, adding error, simulation, output interpretation, and misc. Circuit creation constructs a single instance of the procedure; the circuit gains erroneous gates added through a random number generator; simulations provide the outcome of the iteration; the results are compiled separately. Overall, for larger circuit sizes, building each simulation takes to most amount of time. The time taken to add error to each circuit, interpret the output, and other tasks scales linearly but is insignificant comparatively. An advantage of the Monte Carlo calculations is the lack of information that must be stored from simulation to simulation, **Figure 6.9 c**.

The exact FPT method dedicates the most time to comparing fault-points to each other, , **Figure 6.9 b**. The various FPT functions consist of six types: finding fault-paths, comparing fault-paths, building matrices, matrix math, algebraic math, and misc. Multiple steps require building and compiling fault-paths; the error rate dictionary may gain new entires for scalable matrices; these matrices undergo various math functions; due to the analytical nature the FPT method depends heavily on algebraic math. The comparing fault-path portion starts to dominate the calculations at larger circuits, due to the increased number of fault-paths and the polynomially increased number of fault-points. In

comparison, the last four functions start to become insignificant at larger sizes. The FPT methods require large amounts of resources with large circuits, **Figure 6.9 c**.

6.5 Steane-Shor Quantum Error Correction Code
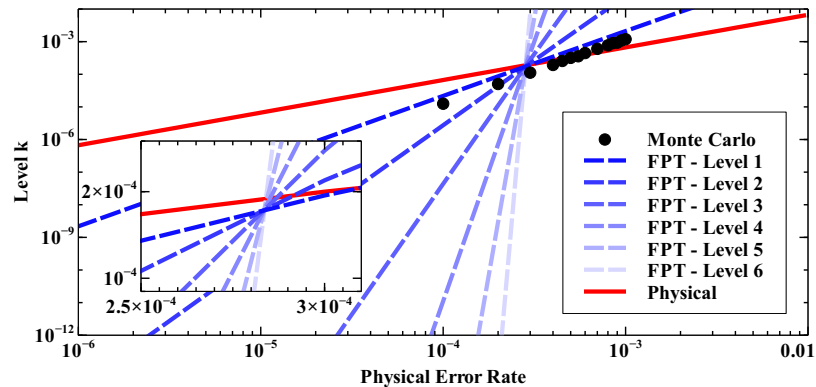
Figure 6.10: The threshold curves based on two methods: the FPT and Monte Carlo simulations for a EC circuit. The FPT shows the threshold curve for different levels of encoding to find the threshold. MC results were found at level one. The AGP result represents the predicted threshold at an infinite level.

A key figure for any error-correcting code is where the logical error rate is less than the physical error rate. This first error threshold is called the pseudothreshold. The threshold is defined for a code family and is the error which below one can achieve arbitrary low failure probability by increasing the code distance. **Figure 6.10** compares the FPT method to Monte-Carlo. We expect Monte-Carlo to give exact results but also it requires more statistics as error rates are reduced [194]. Here we use it to benchmark the pseudothreshold for an isolated error correction implementation. We see that the FPT method yields similar results.

Using the fault-path tracer method, the threshold curve was found for the first five levels of encoding, **Figure 6.10**. The Steane-Shor circuit does not follow the binary-tree pattern; therefore, the FPT method only produces a lower bound on the threshold. It estimates the pseudothreshold at 3.25×10^{-4} which is lower than the Monte Carlo simulations. Since

the difference between these two curves is a second degree polynomial, this emphasizes how the tracing method misses some errors that cancel. Under the assumptions that logical measurement and preparation operations have failure rates as if they were transversal, a level k circuit can be analyzed in terms of $k-1$-level error rates. Our method estimates the real threshold at 1.91×10^{-4}. Here we examine a circuit of I followed by error correction.

The method of Aliferis, Gottesman, and Preskill (AGP) based on fault-paths and malignant pair counting produces a conservative estimate of the threshold. We implemented the AGP method using code from Andrew Cross [195]. We were able to predict a memory threshold assuming error correction, an identity gate, and then error correction. We found a threshold of 5.91×10^{-5}. We expect that the real Pauli error threshold lies above our estimate and this estimate.

6.6 Conclusion

The analytic methods based on fault paths can be used to accurately assess the integrated performance of quantum devices. We have shown the utility of fault paths for understanding the failure of simple algorithms and error correcting codes. Although the method is limited to circuits which are not universal with relatively simple structures, the method is scalable to many qubits. We expect that testing the performance of faulty quantum computers on easy problems will be an important method for showing that errors between gates are sufficiently independent for error correction to work.

The work also suggests that a tensor network approach could be applied to calculate the error of the circuits [196]. Tensor networks are typically used to describe quantum states and to calculate their properties. In this case the tensor network describes the error states and sampling different error output configurations would correspond to changing output error vectors. We expect similarities with the graphical methods for stabilizer circuits [182]. Tensor network contraction also naturally allows for partial parallelization of algorithms and this may lead to faster algorithms for more accurate estimation of error correcting

circuit thresholds.

CHAPTER 7

CONCLUSION

This work reported the initial efforts towards using CaH^+ in future astrochemistry and fundamental physics experiments. We described a multitude of relevant transitions occurring at the vibrational, vibronic, and rovibronic levels, which are applicable to future high-precision molecular spectroscopy, quantum logic spectroscopy (QLS) experiments, and rotational state preparation of CaH^+. The vibronic $1^1\Sigma$ $v_0 \longrightarrow 2^1\Sigma$ $v'_{0,1,2,3,4}$ transitions of CaH^+ and CaD^+; rovibronic $1^1\Sigma$ $v_0,J \longrightarrow 2^1\Sigma$ $v'_{0,1,2,3},J'$ transitions of CaH^+; vibrational $1^1\Sigma$ $v_0 \longrightarrow 1^1\Sigma$ $v'_{9,10}$ transitions of CaH^+ all contribute to future applications.

This work introduced an alternative method to the traditional Hamiltonian method for theoretical calculations. The approach imitated the rate changes occurring during experimentation. By convoluting a broad laser with an underlying transition spectrum, the program accounted for simultaneous Doppler cooling, excitation transitions, and dissociations occurring in resonance enhanced multiphoton photodissociation spectroscopy. The simple model directly estimated the overall dissociation rate analytically, while the simulation model re-created the fluorescence curve seen in experiments from a matrix ODE. Tuning the laser properties produced different transition spectra without modifying the base program.

The models allowed each peak to be assigned to a specific transitions based on previous theoretical predictions. When the theoretical spectrum was optimized to match the experimental spectrum, the models corrected the theoretical predictions. The chosen optimized parameters (transition frequency, transition dipole moments, rotational constants, and dissociation pathway) exposed many discrepancies between predictions and experiments. The vibrational overtones had slight shifts, less than a nanometer, from

theory, and a thinner laser linewidth. Accounting for the Born-Oppenheimer approximation, the vibronic optimizations revealed a 700 cm^{-1} shift in the $2^1\Sigma$ state that was previously unrecorded. The rovibronic optimizations uncovered differences in the rotational constants. The full-simulation model explained dissociation occurs through the $3^1\Sigma$, $1^1\Pi$, and $2^1\Pi$ states.

7.1 Future Work

Long term future projects include QLS, astrochemistry, and fundamental physics. However, the models described in this work have immediate applications based off the results presented here. The isotope shift between CaH$^+$ and CaD$^+$, an experimentally determined potential energy surface, and a rotational cooling scheme are all immediately achievable.

7.1.1 CaH$^+$ and CaD$^+$ Isotope Shift

Previous spectroscopy results potentially reveal the exact isotope shift between CaH$^+$ and CaD$^+$. The potential energy surfaces for both of these diatomics might have minute differences due to the change in mass and/or volume. The vibronic comparison from **Section 3** assumes the Born-Oppenheimer approximation, which eliminates any distinctions between the two PES curves. However, the same results could reveal a small isotopic shift in the $1^1\Sigma \rightarrow 2^1\Sigma$ transition, representing a break down of the Born-Oppenheimer approximation. This shift has been studied in small molecules for years [139, 141, 197–202]. Experiments mostly use NMR spectroscopy [139, 141, 199, 200], but many theoretical studies exist as well [197, 198, 200–202]. Typically lighter molecules have larger shifts, but that assumptions is not always true. H_2O was found to have isotope shift of 0.2 cm^{-1} [198], which as later revised to 23 cm^{-1} [201]. The heavy lead atom has an shift of 0.2 cm^{-1} [197], and Yb$^+$ has found to be 1 Hz [202], while the lighter KH molecule is 10 cm^{-1} [139, 141]. CaH has similar properties to MgH, which is

estimated to have a isotope shift of 0.8 cm^{-1} [199, 200].

The exact isotope shift, Δ, depends on four main parameters:

$$\Delta = (T_{CaH^+}(1) - T_{CaH^+}(0)) - (T_{CaD^+}(1) - T_{CaD^+}(0)), \tag{7.1}$$

where $T_{CaH^+}(1)$ is the zero-point energy of the CaH$^+$ $2^1\Sigma$ state, $T_{CaH^+}(0)$ is the zero-point energy of the CaH$^+$ $1^1\Sigma$ state, $T_{CaD^+}(1)$ is the zero-point energy of the CaD$^+$ $2^1\Sigma$ state, and $T_{CaD^+}(0)$ is the zero-point energy of the CaD$^+$ $1^1\Sigma$ state. Results from **Section 3** give the $T_{CaH^+}(1)$ and $T_{CaD^+}(1)$ terms. The main missing terms are $T_{CaH^+}(0)$ and $T_{CaD^+}(0)$, both of which require additional experimentation. While results similar to **Section 5.1** could give the $T_{CaH^+}(0)$ term, calculations require additional overtones closer to v=0 to accurately account for the vibrational distortion. Similarly, the $T_{CaD^+}(0)$ term requires all data, since no measurements of the ground state exist.

7.1.2 CaH$^+$ and CaD$^+$ Potential Energy Surface Calculations

The Rydberg–Klein–Rees method derives a potential energy surface from a rotational-vibrational spectra of diatomic molecules [203–208]. As previous results proved theoretical PES curves incorrect, experimental PES curves are particularly relevant. Luckily no additional experimentation is needed to obtain the CaH$^+$ $2^1\Sigma$ PES curve. The RKR1-16 program developed by Le Roy et al. uses the results from **Section 4** to calculate Dunham coefficients and a potential [209]. However, the current rovibronic constants do not seem reasonable, and need to be future analyzed before any calculations are finalized.
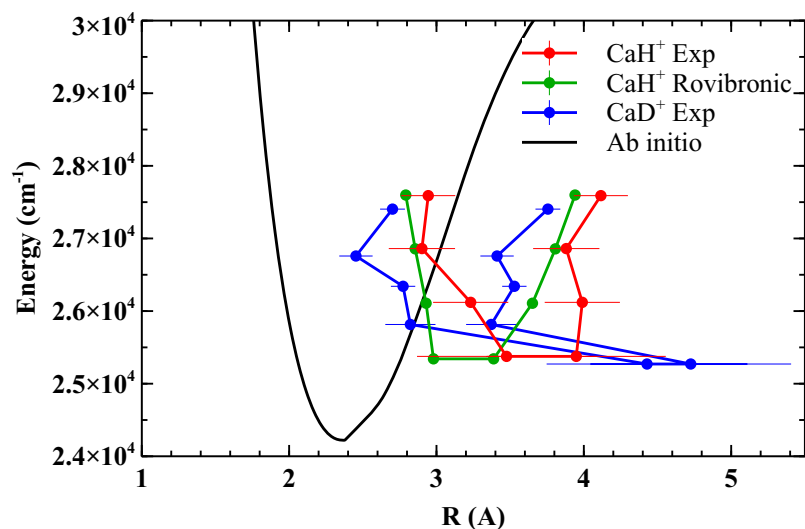
Figure 7.1: An experimental potential energy surface of the CaH$^+$ $2^1\Sigma$ state. The ab initio results originate from Ref. [2]. The experimental results are calculated from manually implementing the Rydberg–Klein–Rees method using data from previous chapters, **Section 3** and **Section 4**. The shift of the potential well is clearly visible.

7.1.3   CaH$^+$ Rotational Cooling

As stated previously, the results from **Section 4** are vital to rotationally cooling CaH$^+$, which in turn is vital to future QLS experiments. The theoretical model does not need any major modification for cooling. The steady state changes from a dissociative state to a ground rovibronic state. Dissociation rates can be removed from calculations as they are not relevant to the problem, but they do not need to be removed as dissociation could occur simultaneous as cooling. Rotational cooling using optical techniques requires precise experimental conditions and prior knowledge of the rotational distribution, [59–61, 109]. Due to the rotational selection rules, the strongest transitions that needs to be excited is the J=1/2 state, but consequently, the J=0 state cannot be excited at all. This emphasis the need for precise laser control. Rotational cooling utilizing optical lasers comes in two flavors: laser pulse shaping and narrow linewidth lasers. Both methods require exciting only one rotational branch, either P or R, with the laser, and relaxing to the J=0 state.

The pulse shaping requires half-Gaussian shaped laser to excite an entire branch, i.e. P

or R branch, of the rotational distribution without accidentally exciting the other branch. To ensure that the J=0 state is not excited, the pulse shape must drop off suddenly on one side, and to excite the entire P branch, the pulse shape must gradually decrease intensity on the other side, [61]. As a consequence, the diatomic molecule must separate P and R branches, which CaH^+ does not. However, BH^+ does have these separate branches, and the cooling over time is shown below, **Figure 7.2**. The theoretical model cannot currently implement a non-Gaussian pulse shape, but this is easily remedied.

$$n_0, v_0, j_{2/3/etc.} \xrightarrow{Pbranch,laser} n_1, v_0, j_{1/2/etc.} \xrightarrow{P/Rbranch,relaxation} n_0, v_0, j_{0/1/etc.} \quad (7.2)$$

$$n_0, v_0, j_{2/3/etc.} \xrightarrow{Pbranch,laser} n_0, v_1, j_{1/2/etc.} \xrightarrow{P/Rbranch,relaxation} n_0, v_0, j_{0/1/etc.} \quad (7.3)$$

$$n_0, v_0, j_{1/2/etc.} \xrightarrow{Pbranch,laser} n_0, v_1, j_{0/1/etc.} \xrightarrow{Rbranch,laser} n_1, v_0, j_{1/2/etc.} \quad (7.4)$$

$$\xrightarrow{P/Rbranch,relaxation} n_0, v_0, j_{0/1/etc.} \quad (7.5)$$
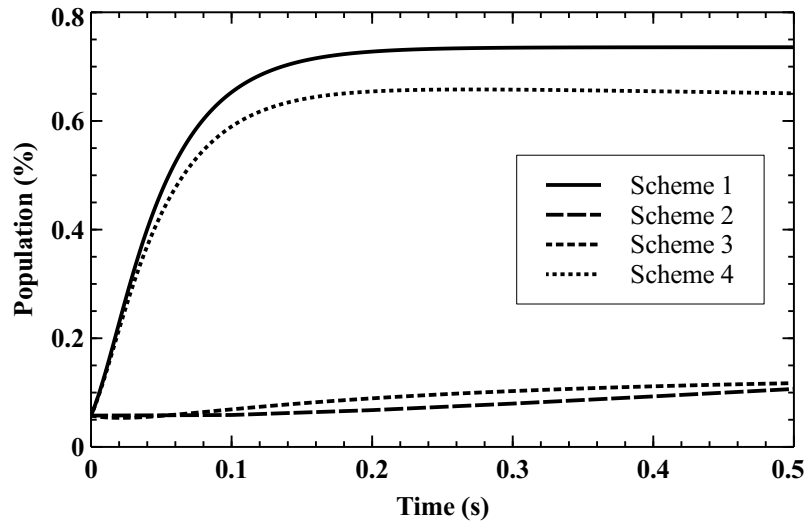
Figure 7.2: BH^+ rotational cooling where the population of the n_1, v_0, k_0 changes over time depending on the three methods listed above.

The narrow linewidth method concentrates on one isolate transitions and lets Le

Chatelier's principle combined with black body radiation drive the transition. Since a single transitions must be excited, the linewidth of the laser must be narrow enough to eliminate any side reactions. This requires separated/isolated rotational transitions, but CaH^+ does not have easily isolated rovibronic transitions. The theoretical model can estimate the cooling rates, but no estimates have been done as of yet.

$$n_0, v_0, \dot{j}_2 \xrightarrow{Pbranch,laser} n_1, v_0, \dot{j}_1 \xrightarrow{P/Rbranch,relaxation} n_0, v_0, \dot{j}_{0/2} \qquad (7.6)$$

$$n_0, v_0, \dot{j}_2 \xrightarrow{Pbranch,laser} n_0, v_1, \dot{j}_1 \xrightarrow{P/Rbranch,relaxation} n_0, v_0, \dot{j}_{0/2} \qquad (7.7)$$

$$n_0, v_0, \dot{j}_1 \xrightarrow{Pbranch,laser} n_0, v_1, \dot{j}_0 \xrightarrow{Rbranch,laser} n_1, v_0, \dot{j}_1 \qquad (7.8)$$

$$\xrightarrow{P/Rbranch,relaxation} n_0, v_0, \dot{j}_{0/2} \qquad (7.9)$$
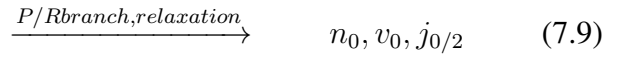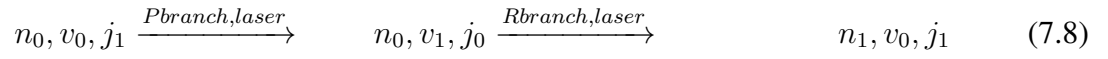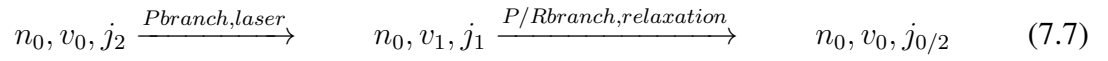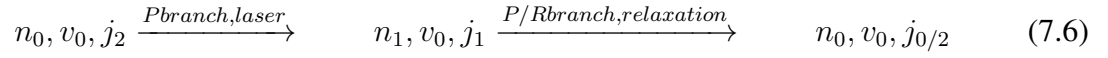
Appendices

A.1 Extension of the Simple Model

The simple model is derived from a simple three state problem where the states are the ground state (N_0), an intermediate transition state (N_1), and the dissociative state (N_2). This is the assumptions that prevents intra-electronic transitions.

$$\frac{dN_0}{dt} = -\Gamma_{01}N_0 - \Gamma_{02}N_0 + \Gamma_{10}N_1 \tag{A.1}$$

$$\frac{dN_1}{dt} = \Gamma_{01}N_0 - \Gamma_{10}N_1 - \Gamma_{12}N_1 \tag{A.2}$$

$$\frac{dN_2}{dt} = \Gamma_{02}N_0 + \Gamma_{12}N_1 \tag{A.3}$$

These rates are converted to a transition matrix form as before. Solving the matrix ODE requires the eigenvalues (λ_0, λ_1, λ_2) and eigenvectors (v_0, v_1, v_2).

$$
\begin{aligned}
\lambda_0 &= 0 \\
\lambda_1 &= 1/2 \left(-\sqrt{(\Gamma_{01} + \Gamma_{10} + \Gamma_{02} + \Gamma_{12})^2 - 4(\Gamma_{01}\Gamma_{12} + \Gamma_{10}\Gamma_{02} + \Gamma_{02}\Gamma_{12})} \right. \\
&\quad \left. -\Gamma_{01} - \Gamma_{10} - \Gamma_{02} - \Gamma_{12} \right) \\
\lambda_2 &= 1/2 \left(\sqrt{(\Gamma_{01} + \Gamma_{10} + \Gamma_{02} + \Gamma_{12})^2 - 4(\Gamma_{01}\Gamma_{12} + \Gamma_{10}\Gamma_{02} + \Gamma_{02}\Gamma_{12})} \right. \\
&\quad \left. -\Gamma_{01} - \Gamma_{10} - \Gamma_{02} - \Gamma_{12} \right)
\end{aligned}
$$

$$E = (\Gamma_{01} - \Gamma_{10} + \Gamma_{02} - \Gamma_{12} + \sqrt{(\Gamma_{01} + \Gamma_{10} + \Gamma_{02} + \Gamma_{12})^2 - 4(\Gamma_{10}\Gamma_{02} + \Gamma_{01}\Gamma_{12} + \Gamma_{02}\Gamma_{12})})$$

$$(\Gamma_{01} + \Gamma_{10} + \Gamma_{02} + \Gamma_{12} + \sqrt{(\Gamma_{01} + \Gamma_{10} + \Gamma_{02} + \Gamma_{12})^2 - 4(\Gamma_{10}\Gamma_{02} + \Gamma_{01}\Gamma_{12} + \Gamma_{02}\Gamma_{12})})$$

$$\frac{1}{2\left(\Gamma_{01}\Gamma_{02} - \Gamma_{10}\Gamma_{02} + \Gamma_{02}^2 - 2\Gamma_{01}\Gamma_{12} - \Gamma_{02}\Gamma_{12} + \dfrac{1}{\Gamma_{02}\sqrt{(\Gamma_{01} + \Gamma_{10} + \Gamma_{02} + \Gamma_{12})^2 - 4(\Gamma_{10}\Gamma_{02} + \Gamma_{01}\Gamma_{12} + \Gamma_{02}\Gamma_{12})}}\right)}$$

$$F = (\Gamma_{01} - \Gamma_{10} + \Gamma_{02} - \Gamma_{12} - \sqrt{(\Gamma_{01} + \Gamma_{10} + \Gamma_{02} + \Gamma_{12})^2 - 4(\Gamma_{10}\Gamma_{02} + \Gamma_{01}\Gamma_{12} + \Gamma_{02}\Gamma_{12})})$$

$$(\Gamma_{01} + \Gamma_{10} + \Gamma_{02} + \Gamma_{12} - \sqrt{(\Gamma_{01} + \Gamma_{10} + \Gamma_{02} + \Gamma_{12})^2 - 4(\Gamma_{10}\Gamma_{02} + \Gamma_{01}\Gamma_{12} + \Gamma_{02}\Gamma_{12})})$$

$$\frac{1}{2\left(-\Gamma_{01}\Gamma_{02} + \Gamma_{10}\Gamma_{02} - \Gamma_{02}^2 + 2\Gamma_{01}\Gamma_{12} + \Gamma_{02}\Gamma_{12} + \dfrac{1}{\Gamma_{02}\sqrt{(\Gamma_{01} + \Gamma_{10} + \Gamma_{02} + \Gamma_{12})^2 - 4(\Gamma_{10}\Gamma_{02} + \Gamma_{01}\Gamma_{12} + \Gamma_{02}\Gamma_{12})}}\right)}$$

$$G = \Gamma_{01}(\Gamma_{01} + \Gamma_{10} + \Gamma_{02} + \Gamma_{12} + \sqrt{(\Gamma_{01} + \Gamma_{10} + \Gamma_{02} + \Gamma_{12})^2 - 4(\Gamma_{10}\Gamma_{02} + \Gamma_{01}\Gamma_{12} + \Gamma_{02}\Gamma_{12})})$$

$$\frac{1}{2\left(-\Gamma_{01}\Gamma_{12} + \Gamma_{02}\left(-\Gamma_{10} - \Gamma_{12} + 1/2\left(\Gamma_{01} + \Gamma_{10} + \Gamma_{02} + \Gamma_{12} + \dfrac{1}{\sqrt{(\Gamma_{01} + \Gamma_{10} + \Gamma_{02} + \Gamma_{12})^2 - 4(\Gamma_{10}\Gamma_{02} + \Gamma_{01}\Gamma_{12} + \Gamma_{02}\Gamma_{12})}}\right)\right)\right)}$$

$$H = \Gamma_{01}(\Gamma_{01} + \Gamma_{10} + \Gamma_{02} + \Gamma_{12} - \sqrt{(\Gamma_{01} + \Gamma_{10} + \Gamma_{02} + \Gamma_{12})^2 - 4(\Gamma_{10}\Gamma_{02} + \Gamma_{01}\Gamma_{12} + \Gamma_{02}\Gamma_{12})})$$

$$\frac{1}{2\left(-\Gamma_{01}\Gamma_{12} + \Gamma_{02}\left(-\Gamma_{10} - \Gamma_{12} + 1/2\left(\Gamma_{01} + \Gamma_{10} + \Gamma_{02} + \Gamma_{12} - \dfrac{1}{\sqrt{(\Gamma_{01} + \Gamma_{10} + \Gamma_{02} + \Gamma_{12})^2 - 4(\Gamma_{10}\Gamma_{02} + \Gamma_{01}\Gamma_{12} + \Gamma_{02}\Gamma_{12})}}\right)\right)\right)}$$

$$M = \begin{bmatrix} 0 & -E & F \\ 0 & G & H \\ 1 & 1 & 1 \end{bmatrix}$$

The SVU decomposition directly solves the matrix ODE problem:

$$M \begin{bmatrix} z_0 \\ z_1 \exp(\lambda_1 t) \\ z_2 \exp(\lambda_2 t) \end{bmatrix} = \begin{bmatrix} N_0(t) \\ N_1(t) \\ N_2(t) \end{bmatrix} \tag{A.4}$$

Since the molecule population is assumed to start in the ground state at time zero and end up in the dissociative state at time infinity, boundary conditions determine the initial constants, (z_0, z_1, z_2).

$$M \begin{bmatrix} z_0 \\ z_1 \\ z_2 \end{bmatrix} = \begin{bmatrix} 1 \\ 0 \\ 0 \end{bmatrix} \tag{A.5}$$

$$M \begin{bmatrix} z_0 \\ 0 \\ 0 \end{bmatrix} = \begin{bmatrix} 0 \\ 0 \\ 1 \end{bmatrix} \tag{A.6}$$

Solving the boundary conditions gives:

$$\begin{bmatrix} z_0 \\ z_1 \\ z_2 \end{bmatrix} = \begin{bmatrix} 1 \\ \frac{H}{G-H} = -\left(1.0 + \frac{E}{F-E}\right) \\ \frac{E}{F-E} = -\left(1.0 + \frac{H}{G-E}\right) \end{bmatrix} \tag{A.7}$$

The dissociation population over time appears immediately.

$$N_2(t) = 1 + \frac{H}{G-H} \exp(\lambda_1 t) + -\left(1.0 + \frac{H}{G-E}\right) \exp(\lambda_2 t) \tag{A.8}$$

In this scenario, there is no immediate connection to the single experiential form:

$$N_2(t) = 1 - \exp(-\Gamma t).$$

A.2   Supporting Information for Revised Theoretical Predictions
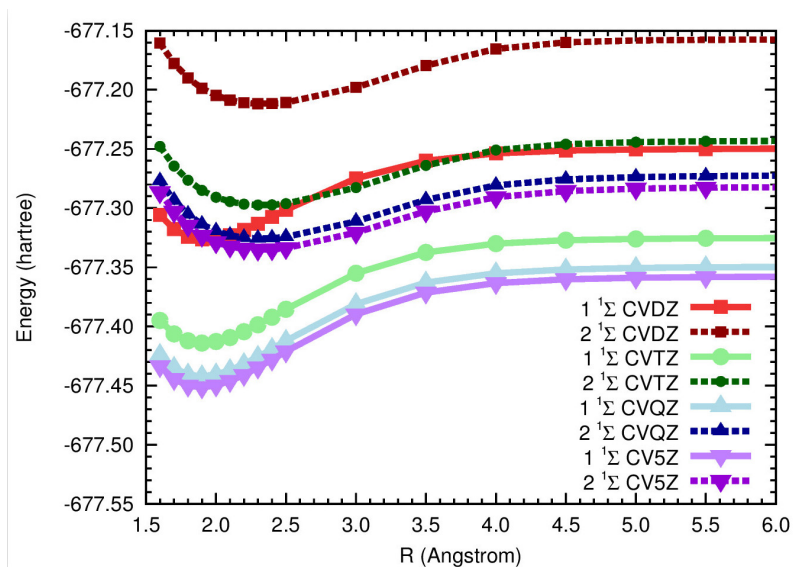
Figure A.1: Convergence of (EOM)-CCSD potential energy curves for CaH$^+$ with respect to basis set.
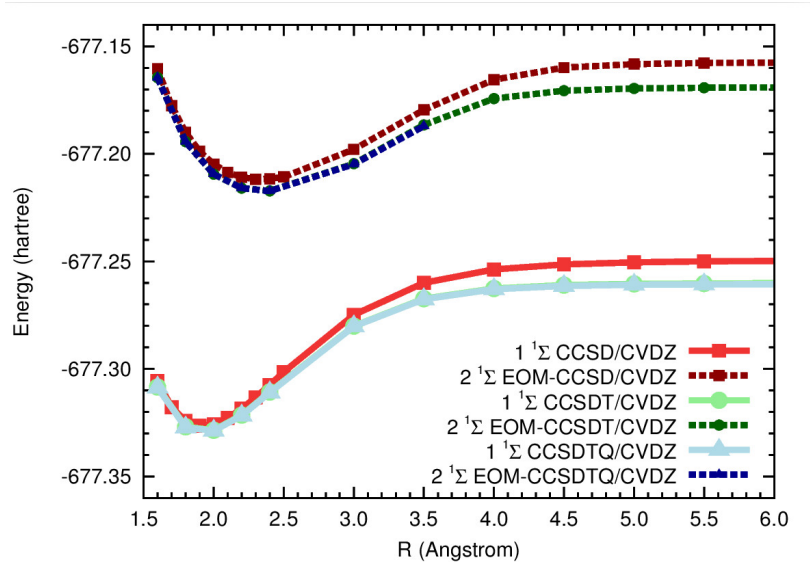
Figure A.2: Convergence of potential energy curves for CaH^+ with respect to electron correlation treatment, using the cc-pCVDZ basis set.

Table A.1: Best estimates of spectroscopic constants (bond lengths in Å, other quantities in cm^{-1}) and total energies (hartrees) at interpolated equilibrium geometries for the $1\,^1\Sigma$ and $2\,^1\Sigma$ states of CaH^+ and CaD^+ at the (EOM)-CCSDT/cc-pCV5Z level of theory, under the Born-Oppenheimer approximation

State	r_e	ω_e	B_e	$\tilde{D}_e$	α_e	$\omega_e x_e$	E_e
$1\,^1\Sigma$ CaH^+	1.89089	1507.1	4.796	1.94E-4	0.10	20.1	-677.462002410
$1\,^1\Sigma$ CaD^+	1.89089	1079.1	2.459	5.11E-5	0.04	10.3	-677.462002410
$2\,^1\Sigma$ CaH^+	2.37234	772.0	3.047	1.90E-4	0.06	3.8	-677.349617993
$2\,^1\Sigma$ CaD^+	2.37234	552.7	1.562	4.99E-5	0.02	1.9	-677.349617993

Table A.2: Spectroscopic constants (bond lengths in Å, other quantities in cm^{-1}) and total energies (hartrees) at interpolated equilibrium geometries for the $1^1\Sigma$ state of CaH$^+$ with various levels of theory

Method	r_e	ω_e	B_e	$\tilde{D}_e$	α_e	$\omega_e x_e$	E_e
CCSDT/cc-pVDZ	1.91034	1439.4	4.699	2.00E-4	0.12	22.0	-677.220894672
CCSD/cc-pVTZ	1.91512	1467.5	4.676	1.90E-4	0.09	18.0	-677.317233199
CCSD(T)/cc-pVTZ	1.91533	1459.3	4.675	1.92E-4	0.09	18.4	-677.319803391
CCSD/cc-pVQZ	1.89837	1514.6	4.758	1.88E-4	0.10	21.2	-677.366168443
CCSD/cc-pCVDZ	1.91999	1449.2	4.652	1.92E-4	0.11	21.5	-677.326512265
CCSD/cc-pCVTZ	1.90378	1491.1	4.731	1.91E-4	0.09	19.8	-677.413936982
CCSD/cc-pCVQZ	1.89407	1508.6	4.780	1.92E-4	0.09	18.8	-677.442064155
CCSD/cc-pCV5Z	1.89190	1513.7	4.791	1.92E-4	0.09	19.2	-677.451397791
CCSD(T)/cc-pCVDZ	1.92087	1440.9	4.648	1.93E-4	0.11	22.4	-677.329064799
CCSD(T)/cc-pCVTZ	1.90345	1483.7	4.733	1.93E-4	0.10	20.3	-677.421677760
CCSD(T)/cc-pCVQZ	1.89288	1502.5	4.786	1.94E-4	0.10	19.6	-677.451588801
CCSDT/cc-pCVDZ	1.92114	1439.9	4.646	1.94E-4	0.11	22.3	-677.329292288
CCSDT/cc-pCVTZ	1.90381	1482.5	4.731	1.93E-4	0.10	20.6	-677.422117460
CCSDT/cc-pCVQZ	1.89318	1501.0	4.785	1.95E-4	0.10	19.7	-677.452488658
CCSDT/cc-pCV5Z	1.89089	1507.1	4.796	1.94E-4	0.10	20.1	-677.462002410
CCSDTQ/cc-pCVDZ	1.92097	1440.3	4.647	1.94E-4	0.11	22.3	-677.329548511

Table A.3: Spectroscopic constants (bond lengths in Å, other quantities in cm^{-1}) and total energies (hartrees) at interpolated equilibrium geometries for the $2^1\Sigma$ state of CaH$^+$ with various levels of theory

Method	r_e	ω_e	B_e	$\tilde{D}_e$	α_e	$\omega_e x_e$	E_e
EOM-CCSD/cc-pVDZ	2.33817	802.9	3.137	1.91E-4	0.05	1.5	-677.104454269
EOM-CCSD/cc-pVTZ	2.33957	853.7	3.133	1.69E-4	0.04	3.0	-677.199792155
EOM-CCSD/cc-pVQZ	2.32222	833.6	3.180	1.85E-4	0.05	1.6	-677.248390508
EOM-CCSDT/cc-pVDZ	2.35708	794.3	3.086	1.86E-4	0.04	-0.4	-677.108074752
EOM-CCSD/cc-pCVDZ	2.33683	839.1	3.140	1.76E-4	0.05	3.4	-677.211792315
EOM-CCSD/cc-pCVTZ	2.32758	849.4	3.165	1.76E-4	0.04	3.0	-677.297436065
EOM-CCSD/cc-pCVQZ	2.31831	845.2	3.191	1.82E-4	0.06	4.3	-677.325657641
EOM-CCSD/cc-pCV5Z	2.31716	843.8	3.194	1.83E-4	0.06	4.0	-677.335117059
EOM-CCSDT/cc-pCVDZ	2.36514	814.6	3.066	1.74E-4	0.04	0.1	-677.217284959
EOM-CCSDT/cc-pCVTZ	2.37073	801.8	3.051	1.77E-4	0.04	0.4	-677.308991179
EOM-CCSDT/cc-pCVQZ	2.36987	779.2	3.053	1.88E-4	0.06	3.0	-677.339816718
EOM-CCSDT/cc-pCV5Z	2.37234	772.0	3.047	1.90E-4	0.06	3.8	-677.349617993
EOM-CCSDTQ/cc-pCVDZ	2.36596	811.1	3.064	1.75E-4	0.04	0.4	-677.217302187

REFERENCES

[1] Minori Abe et al. "Ab initio study on vibrational dipole moments of XH^+ molecular ions: X = ^{24}Mg, ^{40}Ca, ^{64}Zn, ^{88}Sr, ^{114}Cd, ^{138}Ba, ^{174}Yb and ^{202}Hg". In: *J. Phys. B* 43.24 (2010), p. 245102.

[2] Minori Abe et al. "Ab initio study on potential energy curves of electronic ground and excited states of ^{40}CaH$^+$ molecule". In: *Chem. Phys. Lett.* 521 (2012), pp. 31–35.

[3] R. V. Krems. "Cold controlled chemistry". In: *Phys. Chem. Chem. Phys.* 10 (28 2008), pp. 4079–4092.

[4] Xin Tong, Dieter Wild, and Stefan Willitsch. "Collisional and radiative effects in the state-selective preparation of translationally cold molecular ions in ion traps". In: *Phys. Rev. A* 83 (2 Feb. 2011), p. 023415.

[5] H. R. Sadeghpour et al. "Collisions near threshold in atomic and molecular physics". In: *J. Phys. B* 33.5 (2000), R93.

[6] Roman V. Krems. "Recent Research Developments in Chemical Physics". In: ed. by S.G. Pandalai. Recent Research Developments in Chemical Physics v. 3, pt. 2. Transworld Research Network, 2002. Chap. Chemical reactions and inelastic collisions of atoms and molecules at cold and ultracold temperatures, pp. 485–500.

[7] Roman V. Krems. "Molecules near absolute zero and external field control of atomic and molecular dynamics". In: *Int. Rev. Phys. Chem.* 24.1 (2005), pp. 99–118.

[8] Martin T. Bell et al. "Ion-molecule chemistry at very low temperatures: cold chemical reactions between Coulomb-crystallized ions and velocity-selected neutral molecules". In: *Faraday Discuss.* 142 (0 2009), pp. 73–91.

[9] Brianna R. Heazlewood and Timothy P. Softley. "Low-Temperature Kinetics and Dynamics with Coulomb Crystals". In: *Annu. Rev. Phys. Chem.* 66.1 (2015). PMID: 25594853, pp. 475–495.

[10] Alexander D. Gingell et al. "Cold chemistry with electronically excited Ca$^+$ Coulomb crystals". In: *J. Chem. Phys.* 133.19 (2010), p. 194302.

[11] Stefan Willitsch et al. "Chemical applications of laser- and sympathetically-cooled ions in ion traps". In: *Phys. Chem. Chem. Phys.* 10 (48 2008), pp. 7200–7210.

[12] Eric R. Hudson. "Method for producing ultracold molecular ions". In: *Phys. Rev. A* 79 (3 Mar. 2009), p. 032716.

[13] Lincoln D Carr et al. "Cold and ultracold molecules: science, technology and applications". In: *New J. Phys.* 11.5 (2009), p. 055049.

[14] Thomas R. Rizzo, Jaime A. Stearns, and Oleg V. Boyarkin. "Spectroscopic studies of cold, gas-phase biomolecular ions". In: *Int. Rev. Phys. Chem.* 28.3 (2009), pp. 481–515.

[15] Olivier Dulieu et al. "Physics and Chemistry of Cold Molecules". In: *Phys. Chem. Chem. Phys.* 13 (42 2011), pp. 18703–18704.

[16] G. Poulsen, Y. Miroshnychenko, and M. Drewsen. "Efficient ground-state cooling of an ion in a large room-temperature linear Paul trap with a sub-Hertz heating rate". In: *Phys. Rev. A* 86 (5 Nov. 2012), p. 051402.

[17] Stefan Willitsch. "Coulomb-crystallised molecular ions in traps: methods, applications, prospects". In: *Int. Rev. Phys. Chem.* 31.2 (2012), pp. 175–199.

[18] Mikhail Lemeshko et al. "Manipulation of molecules with electromagnetic fields". In: *Mol. Phys.* 111.12-13 (2013), pp. 1648–1682.

[19] Michael Drewsen. "Ion Coulomb crystals". In: *Phys. B* 460 (2015). Special Issue on Electronic Crystals (ECRYS-2014), pp. 105–113.

[20] K. Mølhave and M. Drewsen. "Formation of translationally cold MgH^+ and MgD^+ molecules in an ion trap". In: *Phys. Rev. A* 62 (1 June 2000), p. 011401.

[21] Peter F. Staanum et al. "Probing Isotope Effects in Chemical Reactions Using Single Ions". In: *Phys. Rev. Lett.* 100 (24 June 2008), p. 243003.

[22] J. Doyle et al. "Editorial: Quo vadis, cold molecules?" In: *Eur. Phys. J. D* 31.2 (Nov. 2004), pp. 149–164.

[23] Kenneth R. Brown, Jungsang Kim, and Christopher Monroe. "Co-designing a scalable quantum computer with trapped atomic ions". In: *npj Quantum Inf.* 2 (Nov. 2016). Review Article, p. 16034.

[24] Jee Woo Park et al. "Second-scale nuclear spin coherence time of ultracold 23Na40K molecules". In: *Science* 357.6349 (2017), pp. 372–375.

[25] B. Roth et al. "Ion-neutral chemical reactions between ultracold localized ions and neutral molecules with single-particle resolution". In: *Phys. Rev. A* 73 (4 Apr. 2006), p. 042712.

[26] Stefan Willitsch et al. "Cold Reactive Collisions between Laser-Cooled Ions and Velocity-Selected Neutral Molecules". In: *Phys. Rev. Lett.* 100 (4 Jan. 2008), p. 043203.

[27] Mireille Aymar and Olivier Dulieu. "The electronic structure of the alkaline-earth-atom (Ca, Sr, Ba) hydride molecular ions". In: *J. Phys. B* 45.21 (2012), p. 215103.

[28] Yuan-Pin Chang et al. "Specific Chemical Reactivities of Spatially Separated 3-Aminophenol Conformers with Cold Ca$^+$ Ions". In: *Science* 342.6154 (2013), pp. 98–101.

[29] Masatoshi Kajita and Yoshiki Moriwaki. "Proposed detection of variation in m_p/m_e using a vibrational transition frequency of a CaH$^+$ ion". In: *J. Phys. B* 42.15 (2009), p. 154022.

[30] Masatoshi Kajita et al. "Estimated accuracies of pure XH$^+$ (X: even isotopes of group II atoms) vibrational transition frequencies: towards the test of the variance in m_p/m_e". In: *J. Phys. B* 44.2 (2011), p. 025402.

[31] Masatoshi Kajita et al. "Proposed detection of variation in m_p/m_e using a vibrational transition frequency of a CaH$^+$ ion, Estimated accuracies of pure XH$^+$ (X: even isotopes of group II atoms) vibrational transition frequencies: towards the test of the variance in m_p/m_e". In: *J. Phys. B* 44.20 (2011), p. 209802.

[32] Naoki Kimura et al. "Sympathetic crystallization of CaH$^+$ produced by a laser-induced reaction". In: *Phys. Rev. A* 83 (3 Mar. 2011), p. 033422.

[33] U. Bressel et al. "Manipulation of Individual Hyperfine States in Cold Trapped Molecular Ions and Application to HD^+ Frequency Metrology". In: *Phys. Rev. Lett.* 108 (18 May 2012), p. 183003.

[34] Masatoshi Kajita et al. "Test of m_p/m_e changes using vibrational transitions in N$_2^+$". In: *Phys. Rev. A* 89 (3 Mar. 2014), p. 032509.

[35] Chin-wen Chou et al. "Preparation and coherent manipulation of pure quantum states of a single molecular ion". In: *Nature* 545.7653 (May 2017). Letter, pp. 203–207.

[36] A. Boutalib, J. P. Daudey, and M. El Mouhtadi. "Theoretical study of the lowest electronic states of CaH and CaH$^+$ molecules". In: *Chem. Phys.* 167.1 (1992), pp. 111–120.

[37] Sylvio Canuto, Marcos A. Castro, and K. Sinha. "Theoretical determination of the spectroscopic constants of CaH^+". In: *Phys. Rev. A* 48 (3 Sept. 1993), pp. 2461–2463.

[38] J. C. J. Koelemeij, B. Roth, and S. Schiller. "Blackbody thermometry with cold molecular ions and application to ion-based frequency standards". In: *Phys. Rev. A* 76 (2 Aug. 2007), p. 023413.

[39] J. C. J. Koelemeij et al. "Vibrational Spectroscopy of HD$^+$ with 2-ppb Accuracy". In: *Phys. Rev. Lett.* 98 (17 Apr. 2007), p. 173002.

[40] J. Bruce. Schilling, William A. Goddard, and J. L. Beauchamp. "Theoretical studies of transition-metal hydrides. 1. Bond energies for MH$^+$ with M = Ca, Sc, Ti, V, Cr, Mn, Fe, Co, Ni, Cu, and Zn". In: *J. Am. Chem. Soc.* 108.4 (1986), pp. 582–584.

[41] J. Bruce. Schilling, William A. Goddard, and J. L. Beauchamp. "Theoretical studies of transition-metal hydrides. 2. Calcium monohydride(1+) through zinc monohydride(1+)". In: *J. Chem. Phys.* 91.22 (1987), pp. 5616–5623.

[42] T S Monteiro et al. "Broadening of the Ca$^+$ and Mg$^+$ resonance lines by collision with atomic hydrogen". In: *J. Phys. B* 21.24 (1988), p. 4165.

[43] Héla Habli et al. "Ab Initio Adiabatic and Diabatic Energies and Dipole Moments of the CaH^+ Molecular Ion". In: *J. Phys. Chem. A* 115.48 (2011). PMID: 22013968, pp. 14045–14053.

[44] Hél Habli et al. "Ab initio study of spectroscopic properties of the calcium hydride molecular ion". In: *Eur. Phys. J. D* 64.1 (July 2011), p. 5.

[45] Masatoshi Kajita and Minori Abe. "Frequency uncertainty estimation for the ^{40}CaH$^+$ vibrational transition frequencies observed by Raman excitation". In: *J. Phys. B* 45.18 (2012), p. 185401.

[46] Anders K. Hansen et al. "Single-Ion Recycling Reactions". In: *Angew. Chem. Int. Ed.* 51.32 (2012), pp. 7960–7962.

[47] A. Mokhberi and S. Willitsch. "Sympathetic cooling of molecular ions in a surface-electrode ion trap". In: *Phys. Rev. A* 90 (2 Aug. 2014), p. 023402.

[48] Kunihiro Okada and Masatoshi Kajita. "Toward laser spectroscopy of rotationally cooled CaH$^+$ ions trapped in a cryogenic linear Paul trap". In: *J. Phys. Conf. Ser.* 635.3 (2015), p. 032060.

[49] Naoki Kimura, Masatoshi Kajita, and Kunihiro Okada. "Photodissociation of sympathetically crystallized CaH +". In: *J. Phys. Conf. Ser.* 875.3 (2017), p. 022042.

[50] U. Fröhlich et al. "Ultracold Trapped Molecules: Novel Systemsfor Tests of the Time-Independenceof the Electron-to-Proton Mass Ratio". In: *Astrophysics, Clocks*

and Fundamental Constants. Ed. by Savely G. Karshenboim and Ekkehard Peik. Berlin, Heidelberg: Springer Berlin Heidelberg, 2004, pp. 297–307.

[51]   S. Schiller and V. Korobov. "Tests of time independence of the electron and nuclear masses with ultracold molecules". In: *Phys. Rev. A* 71 (3 Mar. 2005), p. 032505.

[52]   Michael T. Murphy et al. "Strong Limit on a Variable Proton-to-Electron Mass Ratio from Molecules in the Distant Universe". In: *Science* 320.5883 (2008), pp. 1611–1613.

[53]   H. Loh et al. "Precision Spectroscopy of Polarized Molecules in an Ion Trap". In: *Science* 342.6163 (2013), pp. 1220–1222.

[54]   The ACME Collaboration et al. "Order of Magnitude Smaller Limit on the Electric Dipole Moment of the Electron". In: *Science* 343.6168 (2014), pp. 269–272.

[55]   D. DeMille et al. "Enhanced Sensitivity to Variation of m_e/m_p in Molecular Spectra". In: *Phys. Rev. Lett.* 100 (4 Jan. 2008), p. 043202.

[56]   J.-Ph. Karr et al. "Hydrogen molecular ions for improved determination of fundamental constants". In: *Phys. Rev. A* 94 (5 Nov. 2016), p. 050501.

[57]   B. Roth et al. "Precision Spectroscopy of Molecular Hydrogen Ions: Towards Frequency Metrology of Particle Masses". In: *Precision Physics of Simple Atoms and Molecules*. Ed. by Savely G. Karshenboim. Berlin, Heidelberg: Springer Berlin Heidelberg, 2008, pp. 205–232.

[58]   Roman Krems, Bretislav Friedrich, and William C Stwalley, eds. *Cold Molecules: Theory, Experiment, Applications*. CRC Press, 2009.

[59]   Peter F. Staanum et al. "Rotational laser cooling of vibrationally and translationally cold molecular ions". In: *Nat. Phys.* 6.4 (Apr. 2010), pp. 271–274.

[60]   T. Schneider et al. "All-optical preparation of molecular ions in the rovibrational ground state". In: *Nat. Phys.* 6.4 (Apr. 2010), pp. 275–278.

[61]   Chien-Yu Lien et al. "Broadband optical cooling of molecular rotors from room temperature to the ground state". In: *Nat. Commun.* 5.4783 (Sept. 2014).

[62]   A. K. Hansen et al. "Efficient rotational cooling of Coulomb-crystallized molecular ions by a helium buffer gas". In: *Nature* 508.7494 (Apr. 2014). Letter, pp. 76–79.

[63]   P. O. Schmidt et al. "Spectroscopy Using Quantum Logic". In: *Science* 309.5735 (2005), pp. 749–752.

[64]   T. Rosenband et al. "Frequency Ratio of Al^+ and Hg^+ Single-Ion Optical Clocks; Metrology at the 17th Decimal Place". In: *Science* 319.5871 (2008), pp. 1808–1812.

[65]   Sandra Brünken et al. "H_2D^+ observations give an age of at least one million years for a cloud core forming Sun-like stars". In: *Nature* 516.7530 (Dec. 2014). Letter, pp. 219–221.

[66]   E. K. Campbell et al. "Laboratory confirmation of C_{60}^+ as the carrier of two diffuse interstellar bands". In: *Nature* 523.7560 (July 2015). Letter, pp. 322–323.

[67]   Charles M. Olmstedt. "Sunspot Bands Which Appear in the Spectrum of a Calcium Arc Burning in the Presence of Hydrogen". In: *Astrophys. J.* 21 (1908), pp. 66–69.

[68]   A. Eagle. "On the Spectra of Some of the Compounds of the Alkaline Earths". In: *Astrophys. J.* 30 (1909), p. 231.

[69]   Yngve Öhman. "Spectrographic Studies in the Red". In: *Astrophys. J.* 80.9 (1934), p. 171.

[70]   B. Barbuy et al. "Intensity of CaH Lines in Cool Dwarfs". In: *Astron. Astrophys. Suppl. Ser.* 101.2 (1993), pp. 409–413.

[71]   Andrew A. Mills et al. "Ultra-sensitive high-precision spectroscopy of a fast molecular ion beam". In: *J. Chem. Phys.* 135.22 (2011), p. 224201.

[72]   Christian Schneider et al. "Laser-Cooling-Assisted Mass Spectrometry". In: *Phys. Rev. Applied* 2 (3 Sept. 2014), p. 034013.

[73]   Fred J. Grieman, Bruce H. Mahan, and Anthony O'Keefe. "The laser induced fluorescence spectrum of trapped CD^+". In: *J. Chem. Phys.* 72.7 (1980), pp. 4246–4247.

[74]   Fred J. Grieman et al. "Laser-induced fluorescence of trapped molecular ions: the CH^+ $A^1\Pi \leftarrow X^1\Sigma^+$ system". In: *Faraday Discuss.* 71 (0 1981), pp. 191–203.

[75]   D Offenberg et al. "Measurement of small photodestruction rates of cold, charged biomolecules in an ion trap". In: *J. Phys. B* 42.3 (2009), p. 035101.

[76]   R. Rugango et al. "Sympathetic cooling of molecular ion motion to the ground state". In: *New J. Phys.* 17.3 (2015), p. 035009.

[77]   Yong Wan et al. "Efficient sympathetic motional-ground-state cooling of a molecular ion". In: *Phys. Rev. A* 91 (4 Apr. 2015), p. 043425.

[78] Fabian Wolf et al. "Non-destructive state detection for quantum logic spectroscopy of molecular ions". In: *Nature* 530.7591 (Feb. 2016). Letter, pp. 457–460.

[79] Yong Wan et al. "Precision spectroscopy by photon-recoil signal amplification". In: *Nat. Commun.* 5 (Jan. 2014). Article, p. 3096.

[80] D. J. Larson et al. "Sympathetic cooling of trapped ions: A laser-cooled two-species nonneutral ion plasma". In: *Phys. Rev. Lett.* 57 (1 July 1986), pp. 70–73.

[81] Scott T. Sullivan et al. "Trapping molecular ions formed via photo-associative ionization of ultracold atoms". In: *Phys. Chem. Chem. Phys.* 13 (42 2011), pp. 18859–18863.

[82] Matthew T. Hummon et al. "2D Magneto-Optical Trapping of Diatomic Molecules". In: *Phys. Rev. Lett.* 110 (14 Apr. 2013), p. 143001.

[83] Wade G. Rellergert et al. "Evidence for sympathetic vibrational cooling of translationally cold molecules". In: *Nature* 495.7442 (Mar. 2013), pp. 490–494.

[84] Felix H.J. Hall et al. "Ion-neutral chemistry at ultralow energies: dynamics of reactive collisions between laser-cooled Ca+ ions and Rb atoms in an ion-atom hybrid trap". In: *Mol. Phys.* 111.14-15 (2013), pp. 2020–2032.

[85] F. Robicheaux. "Low-energy scattering of molecules and ions in a magnetic field". In: *Phys. Rev. A* 89 (6 June 2014), p. 062701.

[86] Eric R. Hudson. "Sympathetic cooling of molecular ions with ultracold atoms". In: *EPJ Techniques and Instrumentation* 3.1 (Dec. 2016), p. 8.

[87] D. A. Tabor et al. "Suitability of linear quadrupole ion traps for large Coulomb crystals". In: *Appl. Phys. B* 107.4 (June 2012), pp. 1097–1104.

[88] Christian Felix Roos. "Controlling the quantum state of trapped ions". PhD thesis. University of Innsbruck, Feb. 2000.

[89] K Højbjerre et al. "Rotational state resolved photodissociation spectroscopy of translationally and vibrationally cold MgH$^+$ ions: toward rotational cooling of molecular ions". In: *New J. Phys.* 11.5 (2009), p. 055026.

[90] Xin Tong, Alexander H. Winney, and Stefan Willitsch. "Sympathetic Cooling of Molecular Ions in Selected Rotational and Vibrational States Produced by Threshold Photoionization". In: *Phys. Rev. Lett.* 105 (14 Sept. 2010), p. 143001.

[91] C. W. Chou et al. "Frequency Comparison of Two High-Accuracy Al$^+$ Optical Clocks". In: *Phys. Rev. Lett.* 104 (7 Feb. 2010), p. 070802.

[92] B. Roth et al. "Rovibrational spectroscopy of trapped molecular hydrogen ions at millikelvin temperatures". In: *Phys. Rev. A* 74 (4 Oct. 2006), p. 040501.

[93] Jean-Philippe Karr et al. "Vibrational spectroscopy of H_2^+: Hyperfine structure of two-photon transitions". In: *Phys. Rev. A* 77 (6 June 2008), p. 063410.

[94] Kuang Chen et al. "Molecular-ion trap-depletion spectroscopy of $BaCl^+$". In: *Phys. Rev. A* 83 (3 Mar. 2011), p. 030501.

[95] J.-P. Karr, A. Douillet, and L. Hilico. "Photodissociation of trapped H_2^+ ions for REMPD spectroscopy". In: *Appl. Phys. B* 107.4 (June 2012), pp. 1043–1052.

[96] Satrajit Chakrabarty et al. "A Novel Method to Measure Electronic Spectra of Cold Molecular Ions". In: *J. Phys. Chem. Lett.* 4.23 (2013), pp. 4051–4054.

[97] Oskar Asvany et al. "Experimental ground-state combination differences of CH5+". In: *Science* 347.6228 (2015), pp. 1346–1349.

[98] E.S. Endres et al. "Incomplete rotational cooling in a 22-pole ion trap". In: *J. Mol. Spectrosc.* 332 (2017). Molecular Spectroscopy in Traps, pp. 134–138.

[99] Takashi Baba and Izumi Waki. "Cooling and Mass-Analysis of Molecules Using Laser-Cooled Atoms". In: *Jpn. J. Appl. Phys.* 35.9A (1996), p. L1134.

[100] Takashi Baba and Izumi Waki. "Spectral shape of in situ mass spectra of sympathetically cooled molecular ions". In: *J. Appl. Phys.* 92.7 (2002), pp. 4109–4116.

[101] Takashi Baba and Izumi Waki. "Chemical reaction of sympathetically laser-cooled molecular ions". In: *J. Chem. Phys.* 116.5 (2002), pp. 1858–1861.

[102] Craig R. Clark et al. "Detection of single-ion spectra by Coulomb-crystal heating". In: *Phys. Rev. A* 81 (4 Apr. 2010), p. 043428.

[103] Anders Bertelsen, Solvejg Jørgensen, and Michael Drewsen. "The rotational temperature of polar molecular ions in Coulomb crystals". In: *J. Phys. B* 39.5 (2006), p. L83.

[104] D. B. Hume et al. "Trapped-Ion State Detection through Coherent Motion". In: *Phys. Rev. Lett.* 107 (24 Dec. 2011), p. 243902.

[105] Y.-W. Lin, S. Williams, and B. C. Odom. "Resonant few-photon excitation of a single-ion oscillator". In: *Phys. Rev. A* 87 (1 Jan. 2013), p. 011402.

[106] Matthias Germann, Xin Tong, and Stefan Willitsch. "Observation of electric-dipole-forbidden infrared transitions in cold molecular ions". In: *Nat. Phys.* 10.11 (Nov. 2014). Letter, pp. 820–824.

[107] Wayne M Itano et al. "Cooling methods in ion traps". In: *Phys. Scripta* 1995.T59 (1995), p. 106.

[108] Renè Rugango et al. "Vibronic Spectroscopy of Sympathetically Cooled CaH$^+$". In: *ChemPhysChem* 17.22 (2016), pp. 3764–3768.

[109] E. S. Shuman, J. F. Barry, and D. DeMille. "Laser cooling of a diatomic molecule". In: *Nature* 467.7317 (Oct. 2010), pp. 820–823.

[110] Jason H V Nguyen et al. "Challenges of laser-cooling molecular ions". In: *New J. Phys.* 13.6 (2011), p. 063023.

[111] J. H. V. Nguyen and B. Odom. "Prospects for Doppler cooling of three-electronic-level molecules". In: *Phys. Rev. A* 83 (5 May 2011), p. 053404.

[112] I. Manai et al. "Rovibrational Cooling of Molecules by Optical Pumping". In: *Phys. Rev. Lett.* 109 (18 Oct. 2012), p. 183001.

[113] Mehdi Hamamda et al. "Ro-vibrational cooling of molecules and prospects". In: *J. Phys. B* 48.18 (2015), p. 182001.

[114] James E. Goeders et al. "Identifying Single Molecular Ions by Resolved Sideband Measurements". In: *J. Phys. Chem. A* 117.39 (2013). PMID: 23560481, pp. 9725–9731.

[115] Robert J. Le Roy. "LEVEL: A computer program for solving the radial Schrödinger equation for bound and quasibound levels". In: *J. Quant. Spectrosc. Radiat. Trans.* 186 (2017). Satellite Remote Sensing and Spectroscopy: Joint ACE-Odin Meeting, October 2015, pp. 167–178.

[116] Robert J. Le Roy, Geoffrey T. Kraemer, and Sergei Manzhos. "1 potential, 2 potentials, 3 potentials-4: Untangling the UV photodissociation spectra of HI and DI". In: *J. Chem. Phys.* 117.20 (2002), pp. 9353–9369.

[117] John H D Eland et al. "Photo double ionization spectra of CO: comparison of theory with experiment". In: *J. Phys. B* 37.15 (2004), p. 3197.

[118] Jon P. Camden et al. "Probing Excited Electronic States Using Vibrationally Mediated Photolysis Application to Hydrogen Iodide". In: *J. Phys. Chem. A* 108.39 (2004), pp. 7806–7813.

[119]   Robert C. Hilborn. "Einstein coefficients, cross sections, f values, dipole moments, and all that". In: *Am. J. Phys* 50.11 (1982), pp. 982–986.

[120]   Robert C. Hilborn. "Erratum "Einstein coefficients, cross sections, f values, dipole moments, and all that" [Am. J. Phys. 50, 982 (1982)]". In: *Am. J. Phys* 51.5 (1983), pp. 471–471.

[121]   Robert C. Hilborn. "Einstein coefficients, cross sections, f values, dipole moments, and all that". arXiv. Sept. 2002.

[122]   Jeanne L. McHale. *Molecular Spectroscopy*. 1st ed. Prentice Hall, May 1998.

[123]   Alan Corney. *Atomic and Laser Spectroscopy*. Oxford University Press, Oct. 11, 2006. 763 pp.

[124]   K. Thyagarajan and Ajoy Ghatak. *Einstein Coefficients and Light Amplification*. Boston, MA: Springer US, Sept. 27, 2010.

[125]   Anne Meyers Kelley. *Condensed-Phase Molecular Spectroscopy and Photophysics*. John Wiley and Sons Ltd, Dec. 26, 2012. 344 pp.

[126]   Annie Hansson. "Stark Spectroscopy, Lifetimes and Coherence Effects In Diatomic Molecular Systems". PhD thesis. Stockholm University, 2005.

[127]   Annie Hansson and James K.G. Watson. "A comment on Hönl-London factors". In: *J. Mol. Spectrosc.* 233.2 (2005), pp. 169–173.

[128]   A. E. Siegman. "Additional formulas for stimulated atomic transitions". In: *Am. J. Phys* 51.12 (1983), pp. 1110–1113.

[129]   Wolfgang Ketterle. *Covered Topics and Course Notes*. Eprint. 2006.

[130]   Ihar Shchatsinin. "Free Clusters and Free Molecules in Strong, Shaped Laser Fields". PhD thesis. Freien Universitat Berlin, 2009.

[131]   Shih-l Chu, Cecil Laughlin, and Krishna K. Datta. "Two-photon dissociation of vibrationally excited H_2^+. Complex quasi-vibrational energy and inhomogeneous differential equation approaches". In: *Chem. Phys. Lett.* 98.5 (1983), pp. 476–481.

[132]   Cecil Laughlin, Krishna K. Datta, and Shih-I Chu. "Two-photon dissociation of vibrationally excited HD^+ The inhomogeneous differential equation approach". In: *J. Chem. Phys.* 85.3 (1986), pp. 1403–1411.

[133]   Karsten Ahnert and Mario Mulansky. *ODEINT*. 2009.

[134]   Anthony E. Siegman. *Lasers*. University Science Books, May 11, 1986. 1285 pp.

[135]   R. O'Neill. "Algorithm AS47: Function Minimization Using a Simplex Procedure". In: *J. Royal Stat. Soc. C* 20.3 (1971), pp. 338–345.

[136]   P. Blythe et al. "Production of Ultracold Trapped Molecular Hydrogen Ions". In: *Phys. Rev. Lett.* 95 (18 Oct. 2005), p. 183002.

[137]   Ncamiso B. Khanyile, Gang Shu, and Kenneth R. Brown. "Observation of vibrational overtones by single-molecule resonant photodissociation". In: *Nat. Commun.* 6 (July 2015). Article, p. 7825.

[138]   A. Pardo et al. "Laser-induced fluorescence and inelastic collisions of KH molecule". In: *J. Mol. Spectrosc.* 97.2 (1983), pp. 248–252.

[139]   A. Pardo et al. "The $A^1\Sigma$ - $X^1\Sigma$ band system KH and KD molecules". In: *J. Chem. Phys.* 117.1 (1987), pp. 149–162.

[140]   William C. Stwalley, Warren T. Zemke, and Sze Cheng Yang. "Spectroscopy and Structure of the Alkali Hydride Diatomic Molecules and their Ions". In: *J. Phys. Chem. Ref. Data* 20.1 (1991), pp. 153–187.

[141]   Ian R. Bartky. "The $A^1\Sigma$ - $X^1\Sigma$ transition of ^{39}KH and ^{39}KD. Vibrational numbering and molecular constants". In: *J. Mol. Spectrosc.* 20.4 (1966), pp. 299–311.

[142]   W. Zrafi et al. "Evaluation of the adiabatic correction for LiH, RbH and CsH molecules". In: *J. Mol. Struct.* 777.1 (2006). Numerical Simulations in chemistry, after a symposium held in Algeria, pp. 87–97.

[143]   Wei-Cheng Tung, Michele Pavanello, and Ludwik Adamowicz. "Very accurate potential energy curve of the LiH molecule". In: *J. Chem. Phys.* 134.6 (2011), p. 064117.

[144]   G. D. Purvis and R. J. Bartlett. "A Full Coupled-cluster Singles and Doubles Model: The Inclusion of Disconnected Triples". In: *J. Chem. Phys.* 76 (1982), pp. 1910–1918.

[145]   J. Noga and R. J. Bartlett. "The Full CCSDT Model for Molecular Electronic Structure". In: *J. Chem. Phys.* 86 (1987), pp. 7041–7050.

[146]   J. Noga and R. J. Bartlett. "Erratum: The Full CCSDT Model for Molecular Electronic Structure". In: *J. Chem. Phys.* 89 (1988), p. 3401.

[147]   G. E. Scuseria and H. F. Schaefer. "A New Implementation of the Full CCSDT Model for Molecular Electronic Structure". In: *Chem. Phys. Lett.* 152 (1988), pp. 382–386.

[148]   S. A. Kucharski and R. J. Bartlett. "Recursive Intermediate Factorization and Comlete Computational Linearization of the Coupled- Cluster Single, Double, Triple, and Quadruple Excitation Equations". In: *Theor. Chim. Acta* 80 (1991), pp. 387–405.

[149]   S. A. Kucharski and R. J. Bartlett. "The Coupled-Cluster Single, Double, Triple, and Quadruple Excitation Method". In: *J. Chem. Phys.* 97 (1992), pp. 4282–4288.

[150]   T. H. Dunning. "Gaussian Basis Sets for Use in Correlated Molecular Calculations. I. The Atoms Boron Through Neon and Hydrogen". In: *J. Chem. Phys.* 90 (1989), pp. 1007–1023.

[151]   J. Koput and K. A. Peterson. "Ab Initio Potential Energy Surface and Vibrational-Rotational Energy Levels of $X^2\Sigma^+$ CaOH". In: *J. Phys. Chem. A* 106 (2002), pp. 9595–9599.

[152]   J. F. Stanton and R. J. Bartlett. "The Equation of Motion Coupled-cluster Method. A Systematic Biorthogonal Approach to Molecular Excitation Energies, Transition Probabilities, and Excited State Properties". In: *J. Chem. Phys.* 98 (1993), pp. 7029–7039.

[153]   J. D. Watts and R. J. Bartlett. "The Inclusion of Connected Triple Excitations in the Equation-of-Motion Coupled-Cluster Method". In: *J. Chem. Phys.* 101 (1994), pp. 3073–3078.

[154]   S. Hirata. "Higher-Order Equation-of-Motion Coupled-Cluster Methods". In: *J. Chem. Phys.* 121 (2004), pp. 51–59.

[155]   Robert M. Parrish et al. "Psi4 1.1: An Open-Source Electronic Structure Program Emphasizing Automation, Advanced Libraries, and Interoperability". In: *Journal of Chemical Theory and Computation* 13.7 (2017). PMID: 28489372, pp. 3185–3197.

[156]   Zoltán Rolik et al. "An efficient linear-scaling CCSD(T) method based on local natural orbitals". In: *The Journal of Chemical Physics* 139.9 (2013), p. 094105.

[157]   J.F. Stanton et al. *CFOUR, Coupled-Cluster techniques for Computational Chemistry, a quantum-chemical program package.* contributions from A.A. Auer, R.J. Bartlett, U. Benedikt, C. Berger, D.E. Bernholdt, Y.J. Bomble, O. Christiansen, F. Engel, R. Faber, M. Heckert, O. Heun, C. Huber, T.-C. Jagau, D. Jonsson, J. Jusélius, K. Klein, W.J. Lauderdale, F. Lipparini, T. Metzroth, L.A.

Mück, D.P. O'Neill, D.R. Price, E. Prochnow, C. Puzzarini, K. Ruud, F. Schiffmann, W. Schwalbach, C. Simmons, S. Stopkowicz, A. Tajti, J. Vázquez, F. Wang, J.D. Watts and the integral packages MOLECULE (J. Almlöf and P.R. Taylor), PROPS (P.R. Taylor), ABACUS (T. Helgaker, H.J. Aa. Jensen, P. Jørgensen, and J. Olsen), and ECP routines by A. V. Mitin and C. van Wüllen.

[158]   J. Condoluci et al. "Reassigning the CaH$^+$ $1^1\Sigma \to 2^1\Sigma$ vibronic transition with CaD$^+$". In: *arXiv:1705.01326 [physics.atom-ph]* (2017).

[159]   Andrew M. Weiner. "Ultrafast optical pulse shaping: A tutorial review". In: *Opt. Commun.* 284.15 (2011). Special Issue on Optical Pulse Shaping, Arbitrary Waveform Generation, and Pulse Characterization, pp. 3669–3692.

[160]   Dieter Gerlich. "Ion-neutral collisions in a 22-pole trap at very low energies". In: *Phys. Scripta* 1995.T59 (1995), p. 256.

[161]   Jonathan D. Weinstein et al. "Magnetic trapping of calcium monohydride molecules at millikelvin temperatures". In: *Nature* 395.6698 (Sept. 1998), pp. 148–150.

[162]   S R Jefferts et al. "Accuracy evaluation of NIST-F1". In: *Metrologia* 39.4 (2002), p. 321.

[163]   Thomas P Heavner et al. "First accuracy evaluation of NIST-F2". In: *Metrologia* 51.3 (2014), p. 174.

[164]   Isaac L. Chuang and M. A. Nielsen. "Prescription for experimental determination of the dynamics of a quantum black box". In: *J. Mod. Opt.* 44 (1997), pp. 2455–2467.

[165]   Joseph Emerson et al. "Symmetrized characterization of noisy quantum processes". In: *Science* 317 (2007), pp. 1893–1896.

[166]   Joseph Emerson, Robert Alicki, and Karol Życzkowski. "Scalable noise estimation with random unitary operators". In: *J. Opt. B* 7 (2005), S347–S352.

[167]   Benjamin Lévi et al. "Efficient error characterization in quantum information processing". In: *Phys. Rev. A* 75 (2007), p. 022314.

[168]   Christoph Dankert et al. "Exact and approximate unitary 2-designs: constructions and applications". In: *Phys. Rev. A* 80 (2009), p. 012304.

[169]   E. Knill et al. "Randomized benchmarking of quantum gates". In: *Phys. Rev. A* 77 (1 2008), p. 012307.

[170] Steven T. Flammia and Yi-Kai Liu. "Direct fidelity estimation from few pauli measurements". In: *Phys. Rev. Lett.* 106 (23 2011), p. 230501.

[171] Steven T. Flammia et al. "Quantum tomography via compressed sensing: error bounds, sample complexity and efficient estimators". In: *New J. Phys.* 14 (2012), p. 095022.

[172] Marcus P. da Silva, Olivier Landon-Cardinal, and David Poulin. "Practical characterization of quantum devices without tomography". In: *Phys. Rev. Lett.* 107 (21 2011), p. 210404.

[173] Robin Blume-Kohout et al. "Robust, self-consistent, closed-form tomography of quantum logic gates on a trapped ion qubit". In: *arXiv:1310.4492* (2013).

[174] Seth T. Merkel et al. "Self-consistent quantum process tomography". In: *Phys. Rev. A* 87 (6 2013), p. 062119.

[175] Joel Wallman et al. "Estimating the coherence of noise". In: *New J. Phys.* 17.11 (2015), p. 113020.

[176] A. Shabani et al. "Efficient measurement of quantum dynamics via compressive sensing". In: *Phys. Rev. Lett.* 106 (10 2011), p. 100401.

[177] Easwar Magesan, Jay M. Gambetta, and Joseph Emerson. "Robust randomized benchmarking of quantum processes". In: *Phys. Rev. Lett.* 106 (2011), p. 180504.

[178] Easwar Magesan, Jay M. Gambetta, and Joseph Emerson. "Characterizing quantum gates via randomized benchmarking". In: *Phys. Rev. A* 85 (2012), p. 042311.

[179] Aram W. Harrow, Avinatan Hassidim, and Seth Lloyd. "Quantum algorithm for linear systems of equations". In: *Phys. Rev. Lett.* 103 (15 2009), p. 150502.

[180] B. D. Clader, B. C. Jacobs, and C. R. Sprouse. "Preconditioned quantum linear system algorithm". In: *Phys. Rev. Lett.* 110 (25 2013), p. 250504.

[181] Scott Aaronson and Daniel Gottesman. "Improved simulation of stabilizer circuits". In: *Phys. Rev. A* 70 (5 2004), p. 052328.

[182] Simon Anders and Hans J. Briegel. "Fast simulation of stabilizer circuits using a graph-state representation". In: *Phys. Rev. A* 73 (2 2006), p. 022334.

[183] Easwar Magesan et al. "Modeling quantum noise for efficient testing of fault-tolerant circuits". In: *Phys. Rev. A* 87 (1 2013), p. 012324.

[184] Mauricio Gutiérrez et al. "Approximation of realistic errors by Clifford channels and Pauli measurements". In: *Phys. Rev. A* 87 (3 2013), p. 030302.

[185] Mauricio Gutiérrez and Kenneth R. Brown. "Comparison of a quantum error-correction threshold for exact and approximate errors". In: *Phys. Rev. A* 91 (2 2015), p. 022335.

[186] Panos Aliferis, Daniel Gottesman, and John Preskill. "Quantum accuracy threshold for concatenated distance-3 codes". In: *Quant. Inf. Comput.* 6 (2006), pp. 97–165.

[187] Ethan Bernstein and Umesh Vazirani. "Quantum complexity theory". In: *Proceedings of the Twenty-fifth Annual ACM Symposium on Theory of Computing*. STOC '93. New York, NY, USA: ACM, 1993, pp. 11–20.

[188] Andrew Martin Steane. "Error correcting codes in quantum theory". In: *Phys. Rev. Lett.* 77 (5 1996), pp. 793–797.

[189] Yu Tomita et al. "Comparison of ancilla preparation and measurement procedures for the Steane [[7,1,3]] code on a model ion-trap quantum computer". In: *Phys. Rev. A* 88 (4 2013), p. 042336.

[190] Michael A. Nielsen and Isaac L. Chuang. *Quantum computation and quantum information*. 10th Anniversary. Cambridge University Press, 2010.

[191] Yu Tomita. "Numerical and analytical studies of quantum error correction". PhD thesis. Georgia Institute of Technology, 2014.

[192] David P. DiVincenzo and Panos Aliferis. "Effective fault-tolerant quantum computation with slow measurements". In: *Phys. Rev. Lett.* 98 (2007), p. 220501.

[193] Gael Varoquaux Stefan van der Walt S. Chris Colbert. "The NumPy array: a structure for efficient numerical computation". In: *CiSE* 13 (2011), pp. 22–30.

[194] Sergey Bravyi and Alexander Vargo. "Simulation of rare events in quantum error correction". In: *Phys. Rev. A.* 88 (2013), p. 062308.

[195] Panos Aliferis and Andrew W. Cross. "Subsystem fault tolerance with the Bacon-Shor code". In: *Phys. Rev. Lett.* 98 (2007), p. 220502.

[196] Román Orús. "A practical introduction to tensor networks: Matrix product states and projected entangled pair states". In: *Annals of Physics* 349.Supplement C (2014), pp. 117–158.

[197] Jenny E. Rosenthal and G. Breit. "The Isotope Shift in Hyperfine Structure". In: *Phys. Rev.* 41 (4 Aug. 1932), pp. 459–470.

[198]   David W. Schwenke and Dochan Kwak. *First Principle Predictions of Isotopic Shifts in H₂O*. Tech. rep. 20030018927. NASA Ames Research Center, Dec. 2002.

[199]   A. Shayesteh et al. "Fourier transform infrared emission spectra of MgH and MgD". In: *J. Chem. Phys.* 120.21 (2004), pp. 10002–10008.

[200]   Robert D. E. Henderson et al. "Accurate Analytic Potential and Born–Oppenheimer Breakdown Functions for MgH and MgD from a Direct-Potential-Fit Data Analysis". In: *J. Phys. Chem. A* 117.50 (2013). PMID: 24093511, pp. 13373–13387.

[201]   Patrick Meier et al. "Transformation of potential energy surfaces for estimating isotopic shifts in anharmonic vibrational frequency calculations". In: *J. Chem. Phys.* 140.18 (2014), p. 184111.

[202]   Cédric Delaunay and Yotam Soreq. "Probing New Physics with Isotope Shift Spectroscopy". In: *arXiv* (2016).

[203]   N L Singh and D C Jain. "The Rydberg-Klein-Rees Method of Constructing the True Potential Energy Curves of Diatomic Molecules". In: *Proc. Phys. Soc.* 79.2 (1962), p. 274.

[204]   Joseph T. Vanderslice. "Modification of the Rydberg—Klein—Rees Method for Obtaining Potential Curves for Doublet States Intermediate Between Hund's Cases (a) and (b)". In: *J. Chem. Phys.* 37.2 (1962), pp. 384–388.

[205]   Frank J. Zeleznik. "Numerical Calculation of Potential-Energy Curves by the Rydberg-Klein-Rees Method". In: *J. Chem. Phys.* 42.8 (1965), pp. 2836–2838.

[206]   R. H. Davies and Joseph T. Vanderslice. "Second-Order WKB Corrections to Rydberg-Klein-Rees Potential Curves". In: *J. Chem. Phys.* 45.1 (1966), pp. 95–99.

[207]   J. L. C. Villaveces et al. "Approximate polynomial expressions for Rydberg-Klein-Rees curves of diatomic covalent molecules". In: *J. Math. Chem.* 2.3 (July 1988), pp. 217–226.

[208]   Alfredo Aguado, Joaquín Juan Camacho, and Miguel Paniagua. "A numerical procedure to obtain accurate potential energy curves for diatomic molecules". In: *J. Mol. Struct.* 254.Supplement C (1992), pp. 135–144.

[209]   Robert J. Le Roy. "RKR1: A computer program implementing the first-order RKR method for determining diatomic molecule potential energy functions". In: *J. Quant. Spectrosc. Radiat. Trans.* 186 (2017). Satellite Remote Sensing and Spectroscopy: Joint ACE-Odin Meeting, October 2015, pp. 158–166.

EDUCATION

Georgia Institute of Technology   June 2013 - October 2017
Ph.D. in Theoretical/Computational Chemistry   Atlanta, GA

· Cumulative GPA: 3.71

The University of Texas   August 2010 - December 2012
B.S. in Chemistry: Computation, B.S. in Mathematics: Scientific Computing   Austin, TX

· Cumulative GPA: 3.51, Chemistry GPA: 3.54, Math GPA: 3.49
· Elements of Computing Certificate

Colin College   May 2011 - August 2011
Transient Student   Plano, TX

· Cumulative GPA: 4.0

The University of North Texas   August 2008 - December 2010
High School Diploma   Denton, TX

· Texas Academy of Mathematics and Science (TAMS)
· Cumulative GPA: 3.916
· Dean's List in Spring 2009, President's List in Fall 2008

WORK EXPERIENCE

Graduate Research Assistant   January 2014 - October 2017
Mentor: Kenneth R. Brown   *Georgia Institute of Technology*

· Project 1: Wrote python program to model discrete stochastic events, using a tensor network framework, to analytically calculate quantum error probabilities (Paper 3)
· Project 2: Wrote C++/MPI program to model deterministic time-dependent changes, using matrix differential equations and non-linear regression, to implicitly solve for constants and rates (Papers 1,4,5)
· Project 3: Using C++/MPI to model dynamic changes to implicitly search for optimal conditions for newer experimental methods
· Managed/created group events, web resources, and communication

· Mentored graduate, undergraduate, and high school students:
John Condoluci Current Georgia Tech Ph.D. Student
Aaron Calvin Current Georgia Tech Ph.D. Student
Silas Fradley Current Georgia Tech B.S. Student
Conor Smith Current Lewis & Clark B.S. Student
Lucy Grant Current High School Student
Ryan Sheehan Former High School Student, Current Georgia Tech B.S. Student
Alonzo Hernandez Former High School Student, Current Georgia Tech B.S. Student

Graduate Teaching Assistant   August 2016
Office of Institute Diversity (OMED) Challenge Program   *Atlanta, GA*

· 20 hours per week for one month
· Taught general chemistry for in-coming minority students
· Graded weekly lab assignments

Graduate Student   Spring 2014
Computational Genomics Class   *Georgia Institute of Technology*

· Used pre-made software, ABySS, for genome assembly of *Meningococcal meningitis*
· Front-end GUI/design of http://gbrowse2014.biology.gatech.edu/ using HTML, CSS, and javascript

Graduate Teaching Assistant   August 2013 - May 2014
Freshman Chemistry Program   *Georgia Institute of Technology*

· 20 hours per week
· Taught weekly general chemistry lab for engineers, recitations, and tutoring hours
· Graded weekly lab reports and quizzes
· Taught three sections of 24 undergrads each

Graduate Researcher (Special Project)   August 2013 - December 2013
Mentor: Dr. C. David Sherrill   *Georgia Institute of Technology*

· Studied conformers of six molecules with methane-pi interaction to determine the effect on the energy change between folded and unfolded configurations

Graduate Researcher (Special Project)   June 2013 - August 2013
Mentor: Dr. Jean-Luc Bredas   *Georgia Institute of Technology*

· Studied Gallium-doped Zinc oxide surfaces with self-assembled monolayers to determine the effect of an increased gallium ratio on the work function

Tutor   January 2013 - June 2013
Wyzant   *Plano, TX*

· 9 hours per week
· Tutored general chemistry for college students
· Tutored various middle/elementary subjects

Researcher (Undergraduate Special Project)   January 2011 - December 2011
Mentor: Dr. Graeme Henkelman   *The University of Texas*

· Started python program to efficiently predict the optimized configuration of a metal
nanoparticles with two different atoms based on patterns

Researcher (High School)   January 2009 - May 2010
Mentor: Dr. Thomas Cundari   *University of North Texas*

· Studied ground state, stretching frequency and bond length of Nickel aluminum
· Entered research into competitions

Tutor   August 2009 - December 2009
University of North Texas   *Denton, TX*

· 6 hours per month
· Tutored general chemistry and calculus to high schoolers

General Employee   May 2007 - December 2007
Firehouse Subs   *Plano, TX*

· Preparing food (cooking food, arranging food, presenting food)
· Clean-up (cleaning dining area, cleaning dishes, cleaning bathrooms)
· Closing (locking doors, stocking, preparations for next day)

PEER-REVIEWED PUBLICATIONS

1. Rugango, R.; Calvin, A. T.; Janardan, S.; Shu, G., Brown, K. R. Vibronic
   spectroscopy of sympathetically cooled CaH^+ *ChemPhysChem* 17, 3764 **2016**.

2. Gutiérrez, M.; Smith, C.; Lulushi, L.; Janardan, S.; Brown, K. R. Errors and
   pseudothresholds for incoherent and coherent noise. *Phys. Rev. A* 94, 042338 **2016**.

3. Janardan, S.; Tomita, Y.; Gutiérrez, M.; Brown, K. R. Analytical error analysis of
   Clifford gates by the fault-path tracer method. *Quantum Inf Process* 15, 3065 **2016**.

4. Cundari, T. R.; Janardan, S.; Olatunji-Ojo, O.; Wilson, B. R. A first-principles study
   of diatomic NiAl: ground state, structure, and spectroscopic constants. *Int. J.
   Quantum Chem.* **2010**.

5. Condoluci, J. J.; Janardan, S.; Calvin, A. T.; Shu, G., Brown, K. R. Isotopic effect on analysis for spectroscopy of sympathetically cooled $^{40}CaH^+$. *in preparation*

6. Calvin, A. T.; Janardan, S.; Condoluci, J. J.; Rugango, R.; Pretzsch, E.; Shu, G., Brown, K. R. Rovibronic spectroscopy of sympathetically cooled $^{40}CaH^+$ using Fourier transform femtosecond pulse shaping. *in preparation*

CONFERENCES

Career, Research, and Innovation Development Conference (CRIDC)   February 2017
Poster: Papers (1)(5)(6)   *Atlanta, GA*

Cold Molecule Multidisciplinary University Research Initiative (MURI)   October 2016
Poster: Papers (1)(5)(6)   *Atlanta, GA*

Southwest Quantum Information and Technology Conference (SQuInT) February 2015
Poster: Papers (3)   *Berkeley, CA*

Georgia Tech Chemistry and Biochemistry Fall Retreat   November 2014
Poster: Papers (3)   *Helen, GA*

Texas Academy of Mathematics and Science Summer Research Presentation August 2009
Poster: Papers (4)   *Denton, TX*

UNT University Scholars Day   April 2010
Talk: Papers (4)   Denton, TX

· 2nd Place in Chemistry Division

AWARDS

Fellowship Recipient   Fall 2013 - Summer 2015
Graduate Assistance in Areas of National Need (GAANN)   *Georgia Institute of Technology*

Semi-Finalists   Spring 2010
Intel Science Talent Search   *Nation-Wide*

146

Semi-Finalists Spring 2010
Siemens Competition in Math, Science & Technology *Nation-Wide*

Scholarship Recipient Summer 2009
TAMS Summer Research Scholarship *University of North Texas*

OUTREACH/VOLUNTEER EXPERIENCE

Volunteer Traffic Marshall April 2017
March For Science Atlanta Atlanta, GA

· Directed marchers from subway station to march location

Volunteer Science Fair Judge March 2017
Georgia Science and Engineering Fair Athens, GA

· Senior Division, Tier I Judge, Junior Division Category Leader
· Scored senior division projects in physics and astronomy
· Picked junior division category winner for physics and astronomy

Volunteer Lesson Planner February 2017
SciRen Lesson Planning Atlanta, GA

· Transformed Ph.D. research into lessons plans for K-12 curriculum of local Georgia schools

General Volunteer January 2017
CEISMC Kids Club Atlanta, GA

· Ran chemistry demos with 2nd-3rd graders to encourage interest in science

Volunteer Food Packer December 2016
Feed My Starving Children-Hope Filled Holiday Meal Packing Event Atlanta, GA

· Packed food to help feed 282 under-fed children for one year

Volunteer Teacher/Registration Team Co-Lead January 2015-May 2016
Chinmaya Mission Niketan (Temple) Norcross, GA

· Taught 3rd, 7th, and 8th grade students (various years)
· Maintained front-end of registration website and wrote registration how-to manuals
· Helped customers with registration process and with book sales

General Volunteer   August 2016, August 2015
Chemistry Lab Coat Sales   Atlanta, GA

· Sold lab coats, lab books, and googles to general chemistry students

General Volunteer   January 2003 - May 2010
Chinmaya Mission Saaket (Temple)   Dallas, TX

· Bookstore management (yearly inventory, knowledge of bookstore procedures, organizing books, selling of products, managing cash register)
· Babysiting (watch over young kids, break up fights/solve conflicts, help find parents)
· Noise Control (keeping track of location of various classes, making sure no one is disturbing others)
· Training new members (teaching new proceedings, keeping trainees focused)

PROFESSIONAL SOCIETIES

1. APS

CLUBS

Writer   August 2010 - December 2012
Nazar (South Asian Magazine)   University of Texas

· Online magazine dedicated to perspective of South Asians
· Contributed articles for the magazine on current events and personal perspective

General Member   August 2010 - December 2012
Indian Student Association   University of Texas

· 1hr/week, 9weeks/yr

General Member   August 2010 - December 2012
Indian Culture Association   University of Texas

· 1hr/week, 9weeks/yr